

Summer 8-31-2011

Energy propagation in jammed granular matter

Xiaoni Fang
New Jersey Institute of Technology

Follow this and additional works at: <https://digitalcommons.njit.edu/dissertations>



Part of the [Mathematics Commons](#)

Recommended Citation

Fang, Xiaoni, "Energy propagation in jammed granular matter" (2011). *Dissertations*. 285.
<https://digitalcommons.njit.edu/dissertations/285>

This Dissertation is brought to you for free and open access by the Electronic Theses and Dissertations at Digital Commons @ NJIT. It has been accepted for inclusion in Dissertations by an authorized administrator of Digital Commons @ NJIT. For more information, please contact digitalcommons@njit.edu.

Copyright Warning & Restrictions

The copyright law of the United States (Title 17, United States Code) governs the making of photocopies or other reproductions of copyrighted material.

Under certain conditions specified in the law, libraries and archives are authorized to furnish a photocopy or other reproduction. One of these specified conditions is that the photocopy or reproduction is not to be “used for any purpose other than private study, scholarship, or research.” If a user makes a request for, or later uses, a photocopy or reproduction for purposes in excess of “fair use” that user may be liable for copyright infringement,

This institution reserves the right to refuse to accept a copying order if, in its judgment, fulfillment of the order would involve violation of copyright law.

Please Note: The author retains the copyright while the New Jersey Institute of Technology reserves the right to distribute this thesis or dissertation

Printing note: If you do not wish to print this page, then select “Pages from: first page # to: last page #” on the print dialog screen

The Van Houten library has removed some of the personal information and all signatures from the approval page and biographical sketches of theses and dissertations in order to protect the identity of NJIT graduates and faculty.

ABSTRACT

ENERGY PROPAGATION IN JAMMED GRANULAR MATTER

by
Xiaoni Fang

The systems built from dense granular materials are very important due to their relevance to a number of technological and other fields. However, they are difficult to study in particular due to a lack of accurate continuum description. In this work, studies on these systems are presented using discrete element simulations that model the granular particles as soft, elastic, and frictional disks which interact when in contact. These simulations are used for the purpose of analyzing a few granular systems with the main emphasis on understanding phenomena of energy and force propagation.

Analysis of energy propagation in a two-dimensional disordered system is carried out by considering the propagation of information away from an oscillating boundary which is characterized by both temporal and spatial structure. This spatial structure, in particular, is important since it makes comparison to any continuum model more challenging and insightful. The results are compared to a simple linear wave equation with damping, and a very good agreement is found. This result suggests, that at least for the dense, compressed, jammed systems considered here, mathematical description of energy propagation based on a simple continuum model is possible.

The simulation is then extended to consider the process of impact of a large-scale intruder on a granular system. In this problem, a detailed investigation is considered on the manner in which energies and forces propagate, and in particular a concentration on the influence of material parameters, such as inter-particle friction, is studied. This analysis has led to better understanding of the scaling relations connecting the intruder's speed and its depth of penetration.

Finally, the dynamics of dense granular flow in a hopper geometry is modeled and studied, where the flow is sensitive to jamming. Extensive analysis of this problem have been carried out, including large scale statistical analysis of data in order to understand the influence of statistical fluctuations on the results.

ENERGY PROPAGATION IN JAMMED GRANULAR MATTER

by
Xiaoni Fang

A Dissertation
Submitted to the Faculty of
New Jersey Institute of Technology and
Rutgers, The State University of New Jersey – Newark
in Partial Fulfillment of the Requirements for the Degree of
Doctor of Philosophy in Mathematical Sciences

Department of Mathematical Sciences, NJIT
Department of Mathematics and Computer Science, Rutgers-Newark

August 2011

Copyright © 2011 by Xiaoni Fang

ALL RIGHTS RESERVED

APPROVAL PAGE

ENERGY PROPAGATION IN JAMMED GRANULAR MATTER

Xiaoni Fang

Dr. Lou Kondic, Dissertation Advisor Date
Professor, Department of Mathematical Sciences, NJIT

Dr. Denis Blackmore, Committee Member Date
Professor, Department of Mathematical Sciences, NJIT

Dr. Robert Miura, Committee Member Date
Distinguished Professor, Department of Mathematical Sciences, NJIT

Dr. Richard Moore, Committee Member Date
Associate Professor, Department of Mathematical Sciences, NJIT

Dr. Pushpendra Singh, Committee Member Date
Professor, Department of Mechanical and Industrial Engineering, NJIT

BIOGRAPHICAL SKETCH

Author: Xiaoni Fang
Degree: Doctor of Philosophy
Date: August 2011

Undergraduate and Graduate Education:

- Doctor of Philosophy in Mathematical Sciences,
New Jersey Institute of Technology, Newark, NJ, 2011
- Master of Science in Mathematics,
Oklahoma State University, Stillwater, OK, 2006
- Bachelor of Science in Information and Computational Science,
Beijing Jiaotong University, Beijing, China, 2003

Major: Mathematical Sciences

Presentations and Publications:

- X. Fang, “Modeling Hopper Flow,” poster presentation, *International Fine Particles Research Institute Annual Meeting*, Chapel Hill, NC, June 2011
- X. Fang, “On influence of microstructure on granular impact”, poster presentation, *Dana Knox Research Showcase*, New Jersey Institute of Technology, Newark, NJ, April 2011.
- X. Fang, “On influence of microstructure on granular impact”, poster presentation, *63rd Annual Meeting of American Physical Society*, Long Beach, CA, November 2010.
- X. Fang, “Jamming and energy propagation through dense granular materials”, poster presentation, *62nd Annual Meeting of American Physical Society*, Minneapolis, MN, November 2009.
- X. Fang, “Signal propagation through dense granular systems”, poster presentation, *Frontiers in Applied and Computational Mathematics*, New Jersey Institute of Technology, Newark, NJ, July 2009.

- X. Fang, “Signal propagation through dense granular systems”, poster presentation, *Gordon Research Conferences on Nonlinear Science*, South Hadley, MA, June 2009.
- X. Fang, “Signal propagation through dense granular systems”, poster presentation, *7th Granular Material Workshop*, New Haven, CO, May 2009.
- X. Fang, “Signal propagation through dense granular systems”, poster presentation, *Dana Knox Research Showcase*, New Jersey Institute of Technology, Newark, NJ, April 2009.
- L. Kondic, X. Fang, O.M. Dybenko, and R. P. Behringer “Energy transport through dense granular matter”, *Powders and Grains 2009*, eds. M. Nakagawa and S. Luding, *AIP Conference Proceedings* 1145, 293-296 (2009).

To my advisor, Dr. Lou Kondic.

ACKNOWLEDGMENT

I give my great gratitude to my advisor Dr. Lou Kondic for his untiring guidance on my dissertation through the years, and valuable and inspiring advice on many aspects of my life.

I truly sincerely thank Dr. Denis Blackmore, Dr. Robert Miura, Dr. Richard Moore, and Dr. Pushpendra Singh for agreeing to be on my committee and any help you offered. I would like to thank Drs. Mark Shattuck from the City College of CUNY and Robert P. Behringer from Duke University for helping me learn more about granular matter.

I would also like to thank the Department of Mathematical Sciences at NJIT for their financial support and everybody in the department. It has been a pleasant five years overall.

Finally, I take this opportunity to express my thanks to The Big Bang Theory, the TV show, not the real theory. Thanks for the great show and you have accompanied me through many long nights.

TABLE OF CONTENTS

Chapter	Page
1 INTRODUCTION	1
1.1 Granular Materials	1
1.2 Dense Jammed Granular Systems	1
1.3 Literature	3
1.4 Overview	4
2 1-D GRANULAR SYSTEMS	6
2.1 One-Dimensional Hertzian Chains	6
2.1.1 Strongly Compressed Chains $ u_{i-1} - u_i \ll \delta_0$	7
2.1.2 Weakly Compressed Chains $ u_{i-1} - u_i \gg \delta_0$	10
2.2 Other Nonlinear Lattices	13
2.2.1 The Fermi-Pasta-Ulam Lattice	13
2.2.2 The Toda Lattice	14
3 2-D GRANULAR SYSTEMS WITH BOUNDARY EXCITATIONS	16
3.1 Introduction	16
3.2 Methods	18
3.3 Results	21
3.3.1 Infinite Wavelength Perturbation	21
3.3.2 Finite Wavelength Perturbation	28
3.3.3 Parametric Dependence I: System Parameters	30
3.3.4 Parametric Dependence II: Perturbation Properties	38
3.3.5 Constant Pressure (CP) System	41
3.4 Discussion	43
3.4.1 Continuum Model	44
3.4.2 Particle Scale Response	45
3.5 Conclusions	51

TABLE OF CONTENTS
(Continued)

Chapter	Page
4 IMPACT ON 2-D GRANULAR SYSTEMS	55
4.1 Overview	55
4.2 Introduction	55
4.3 System Setup	57
4.4 Results for the Penetration Depth	60
4.4.1 Intruder Properties	61
4.4.2 System Properties	63
4.5 Microstructure Evolution, Force Networks, and Granular Dynamics during Impact	74
4.5.1 Properties of the Force Field	75
4.5.2 Properties of the Displacement Field	85
4.6 Comparison to Effective Models and Experimental Results	87
4.7 Conclusion	94
5 HOPPER FLOW	97
5.1 Introduction	97
5.2 System Setup and Material Parameters	97
5.3 Simulation Protocol	98
5.4 Calibration of the Model	100
5.5 The Mass Flow Rate	102
5.6 Results	105
5.6.1 Survival Times	105
5.6.2 Time to Empty the Hopper and the Mass Flux	110
5.6.3 Results for Velocities and Pressures	112
5.7 Summary	114
6 CONCLUSIONS	119
APPENDIX A MODELING PARTICLE INTERACTIONS	121

TABLE OF CONTENTS
(Continued)

Chapter	Page
A.1 Force Model	121
A.2 Key Parameters	126
APPENDIX B DISCRETE ELEMENT TECHNIQUES	131
APPENDIX C CONTINUUM MODEL FOR ENERGY PROPAGATION . .	136
C.1 Eigenfunction Approach	136
APPENDIX D AFFINE AND NON-AFFINE DEFORMATIONS	143
APPENDIX E SIMULATING IMPACTS OF A LARGE INTRUDER	147
REFERENCES	151

LIST OF TABLES

Table	Page
3.1 Parameters of the Model	20
5.1 Mean Survival Time for Varied System Parameters of Outlet Size $D = 2.7$ cm and Angle $\theta = 45^\circ$ (Single Realization Results)	101
5.2 Empty Time for Varied System Parameters of Outlet Size $D = 4.5$ cm and Angle $\theta = 60^\circ$ (Single Realization Results)	102
5.3 Mean Survival Time Data (Algebraic Means) over 40 Realization Runs .	105
5.4 Mean Survival Times and Standard Deviations from Exponential Fitting over 40 Realization Runs	108
5.5 Mean Empty Time Data (Averages over 40 Realizations are Used for $D \leq 3.5$ cm, and Single Realizations are Reported for Larger D 's Since If There is No Jamming, the Fluctuations between Realizations are Negligible.)	112

LIST OF FIGURES

Figure	Page
1.1 Experiment result of 3-D force chains from [3]. The bright color shows the force chains.	2
2.1 1-D granular chain of identical grains under a uniform precompression. The initial disturbance is given to the first particle on the left to the right as the arrow indicates.	6
3.1 Total force on granular particles at four different phases during one period of the boundary oscillation; The upper wall is static, and the lower one performs standing type of motion. In this and the following figures, we use $r = 0.1$, $f = 30$ Hz, amplitude $A = 0.6 d$, and 40,000 particles except if specified differently.	22
3.2 Elastic energy at four times during one period of the boundary oscillation; The upper wall is static, and the lower one moves in and out.	24
3.3 Elastic and kinetic energy of the granular particles as the frequency of the perturbation on the lower boundary is modified.	25
3.4 Fourier spectrum (FZ-AXAT) of the elastic energy for four representative frequencies of boundary excitations.	26
3.5 Total force on the particles close to the boundaries.	27
3.6 Elastic energy at four times during one period of the boundary oscillation; The upper wall is static, and the lower one performs standing type of motion. In this and following figures, we use $r = 0.1$, $f = 30$ Hz, $\lambda = 250 d$, $A = 0.6 d$, and 40,000 particles except if specified differently.	29
3.7 Two-dimensional Fourier transform of the elastic energy for the ‘basic’ case ($\lambda = 250 d$, $f = 30$ Hz, $A = 0.6 d$). The system is divided into 64×64 cells and the central row/column corresponds to the 0 mode in the x/z directions, respectively.	29
3.8 Fourier spectrum (FXAT) of the elastic energy as a function of z , the distance from the shearing wall.	30
3.9 Fourier spectrum (FXAT) of three independently prepared systems.	31
3.10 Fourier spectrum (FXAT) in two systems where the domain size in the x direction is varied. $Lx = 250 d$ (solid line) and $Lx = 125 d$ (dashed line) are shown. Here $\lambda = 125 d$	32

LIST OF FIGURES
(Continued)

Figure	Page
3.11 Fourier spectrum (FXAT) in two systems where the domain size in the z direction is varied. The simulations with 40,000 particles (solid line) and 50,000 particles (dashed line) are shown.	33
3.12 Fourier spectrum (FXAT) of the elastic energy for different elastic particle properties.	33
3.13 Fourier spectrum (FXAT) of the elastic energy for different elastic and frictional particle properties. Influence of dynamic and static friction : $\mu = 0$ (solid line, model I), $\mu = 0.5$ (dotted line, model I) and $\mu = 0.5$, $k_t = 0.8k_n$ (dashed line, model II) are shown.	34
3.14 Fourier spectrum (FXAT) in the systems where the stiffness of the particles as well as the frequency of driving were modified, but their ratio was kept constant.	35
3.15 Fourier spectrum (FXAT) of three systems whose only difference is the volume fraction: $\rho = 0.90$ (solid line) $\rho = 0.85$ (dashed line) and $\rho = 0.80$ (dotted line).	36
3.16 Numbers of contacts for $\rho = 0.90$ (solid line), $\rho = 0.85$ (dashed line) and $\rho = 0.80$ (dotted line).	36
3.17 FXAT and elastic energies as polydispersity is changed from $r = 0.1$ (basic case, solid line) $r = 0.2$ (dashed line) $r = 0.4$ (dotted line), and for two monodisperse systems: $\rho = 0.90$ (thick solid line) and $\rho = 0.917$ (thick dashed line).	37
3.18 For $\rho = 0.917$, the average elastic energy of the monodisperse particles is similar to the average elastic energy of the polydisperse case $r = 0.1$. . .	37
3.19 FXAT as the amplitude, A , of imposed perturbation is modified.	38
3.20 FXAT as the wavelength of imposed perturbation is decreased.	39
3.21 FXAT as the frequency, f , of imposed perturbation is modified. Spectral power is shown in part a) since dominant mode could not be clearly identified.	40
3.22 Fourier spectrum (FZ-AXAT) of the elastic energy for four representative frequencies of boundary excitations with $\lambda = 250 d$	41
3.23 Dominant Fourier mode (FXAT) as applied pressure is varied.	42
3.24 Dominant Fourier mode (FXAT) as the wavelength, λ , and frequency, f , of imposed perturbation are varied.	42

LIST OF FIGURES
(Continued)

Figure	Page
3.25 Dominant Fourier mode (FXAT) of systems with different pressures and different polydispersities, r	43
3.26 Affine component of particle dynamics for the ‘basic’ system ($f = 30$ Hz, $\lambda = 250 d$) at $t = 240$	46
3.27 Affine component of particle dynamics at $t = 240$ for specified systems.	46
3.28 Fourier transform (FXAT) of the affine component of particle dynamics. Note different scales in a) - b) versus c) - d).	47
3.29 Monodisperse system ($f = 30$ Hz, $\lambda = 250 d$). The results are shown at $t = 240$	48
3.30 Monodisperse system ($r = 0.0$). The results are shown at $t = 240$	49
3.31 Pair-pair correlation function for the systems characterized by different polydispersities and volume fractions.	50
3.32 The probability that number of contacts of a given particle remains through time in one of the considered groups: $Z \leq 3$ shown by the red (solid) curves, and $Z \geq 4$ shown by the green (dashed) curves. The period of oscillations corresponds to the motion of the boundary.	51
3.33 High frequency driving $f = 100$ Hz ($\lambda = 250 d$, $r = 0.1$). The results are shown at $t = 240$	52
3.34 Short wavelength perturbation: $\lambda = 250 d/4$ ($f = 30$ Hz, $r = 0.1$). The results are shown at $t = 240$	53
3.35 Non-affine component as a function of the distance from the oscillating boundary for few frequencies and wavelengths of the perturbations. Here $r = 0.1$	54
3.36 The probability that number of contacts of a given particle remains through time in one of the considered groups: $Z \leq 3$ shown by the red (solid) curves, and $Z \geq 4$ shown by the green (dashed) curves. The period of oscillations corresponds to the motion of the boundary.	54
4.1 System setup. For illustration we show implementations of both circular and elliptic intruders. In the simulations, one of these shapes is incident on the middle of the upper surface of the granular system.	58
4.2 Penetration depth of $D_i = 10$ intruder impacting with different speed. Here we use $r = 0.2$, $k_n = 4 \cdot 10^3$, $k_t = 0.0$, $e_n = 0.5$, $\mu = 0.5$. Material properties of the intruder are the same as of the granular particles. The arrow shows the direction of increasing impact speed.	61

LIST OF FIGURES
(Continued)

Figure	Page
4.3 Penetration depths of intruders of different sizes. The other parameters and line patterns are the same as in Figure 4.2.	62
4.4 Penetration depth for intruders characterized by different elliptical ogives; we show the results for (i) $a = 5$ and $v = 0.1$ (red squares), $v = 0.4$ (green triangles), $v = 0.7$ (blue diamonds), and for (ii) $a = 10$, $v = 0.7$ (red circles). The domain size was increased in (ii) to $H = 100$, $W = 100$. The other parameters are as in Figure 4.2.	63
4.5 Penetration depth of an intruder in systems with varying stiffness: $k_n = 4 \times 10^3$ (black solid); $k_n = 4 \times 10^4$ (red dashed); $k_n = 4 \times 10^5$ (blue dash-dot). In the part a), the impact speed is $v = 0.7$; in part b), the impact speed in physical units (m/s, for example) is kept fixed at the value $v_p = 0.7d/t_{col}$ ($k_n = 4.0 \cdot 10^3$). The other parameters are as in Figure 4.2.	64
4.6 Penetration depth of an intruder in systems with varying coefficient of restitution, $e_n = 0.9, 0.5, 0.1$ shown by red (solid), dashed (green) and blue (dash-dot) lines, respectively. Here, $v = 0.7$, the system size is $W = 200$, $H = 200$; the other parameters are as in Figure 4.2.	65
4.7 Penetration depth for different friction models and Coulomb thresholds; here we show the results as follows (top to bottom): $\mu = 0$ (red dashed); $\mu = 0.1$, $k_t = 0.0$ (green dotted); $\mu = 0.1$, $k_t = 0.8k_n$ (pink dash-dot-dot), $\mu = 0.5$, $k_t = 0.0$ (black solid); $\mu = 0.5$, $k_t = 0.8k_n$ (blue dash-dot). Here $v = 0.7$, the other parameters are as in Figure 4.2.	66
4.8 Penetration depth for an impact on a hexagonal lattice; here $r = 0.0$ and the other parameters and line patterns are as in Figure 4.2. Note the different range on the vertical axis compared to the one typically used.	68
4.9 Final (long time) penetration depth for the systems characterized by different polydispersities, r ; the other parameters are as in Figure 4.2.	69
4.10 Influence of gravitational acceleration on impact; here, $v = 1.0$ and the other parameters are as in Figure 4.2. We chose g 's (given in cm/s^2), appropriate to various objects in the Solar system: Pluto, Moon, Mars, Earth, Jupiter.	70
4.11 Snapshots of a granular system after impact under the four larger gravities considered here ($g = 160, 369, 980$, and 2479 cm/s^2) from Figure 4.10 at $t \approx 300$. Gravity is monotonously increasing from a) to d).	71

LIST OF FIGURES
(Continued)

Figure	Page
4.12 Influence of the system width, W , and height, H , on the penetration depth as a function of time. The solid/dashed lines show three realizations of impacts with the speed $v = 1.0/0.1$, respectively. The other parameters are as in Figure 4.2.	72
4.13 Penetration depth for a system characterized by $W = 100$ and $H = 200$; the impact speed is $v = 0.7$; the other parameters are as in Figure 4.2. .	74
4.14 Normal force experienced by the granular particles at four different times. Here, $v = 0.7$, and the other parameters are as in Figure 4.2 (kinetic friction).	76
4.15 Tangential force experienced by the granular particles at four different times for the same parameters as in Figure 4.14 (kinetic friction). . . .	76
4.16 Normal force experienced by the granular particles at four different times for $k_t = 0.8k_n$; the other parameters are as in Figure 4.14 (static friction).	77
4.17 Tangential force experienced by the granular particles at four different times for the same parameters as in Figure 4.16 (static friction).	78
4.18 Normal force experienced by the granular particles at fixed distances below the surface due to an impact on a hexagonal lattice at time $t = 24$; $\mu = 0$ (red up-triangles); $\mu = 0.1$, $k_t = 0.0$ (green down-triangles); $\mu = 0.1$, $k_t = 0.8k_n$ (pink squares), $\mu = 0.5$, $k_t = 0.0$ (black diamonds); $\mu = 0.5$, $k_t = 0.8k_n$ (blue circles). Here $v = 0.7$, the other parameters are as in Figure 4.2.	79
4.19 Normal force experienced by the granular particles at four different times during impact on a hexagonally ordered system. Here, $r = 0.0$, and the other parameters are as in Figure 4.14 (kinetic friction).	79
4.20 Tangential force experienced by the granular particles at four different times for the same system as in Figure 4.19 (kinetic friction).	80
4.21 Normal force experienced by the granular particles at four different times for $k_t = 0.8k_n$; the other parameters are as in Figure 4.19 (static friction).	80
4.22 Tangential force experienced by the granular particles at four different times for the same system as in Figure 4.21 (static friction).	81

LIST OF FIGURES
(Continued)

Figure	Page
4.23 The total force on the intruder as a function of time for the following systems (depth versus time for the systems in part (a) is available in Figure 4.7): $\mu = 0$ (red dashed); $\mu = 0.1$, $k_t = 0.0$ (green dotted); $\mu = 0.1$, $k_t = 0.8k_n$ (pink dash-dot-dot), $\mu = 0.5$, $k_t = 0.0$ (solid black); $\mu = 0.5$, $k_t = 0.8k_n$ (blue dash-dot). Here $v = 0.7$; the other parameters are as in Figure 4.2.	81
4.24 Zeroth Betti number, B_0 , for the normal force during impacts on polydisperse, $r = 0.2$, systems with $v = 0.7$ and (a) kinetic friction; (b) static friction; the other parameters are as in Figure 4.2. In this and the following figures, B_0 's are normalized by the number of particles, and the forces by the average (normal) force on all particles. Note that the peaks in the B_0 's for $F / \langle F \rangle \approx 2$ are due to the elastic waves propagating through the system.	83
4.25 Zeroth Betti number, B_0 , for the tangential force during impacts on the systems as in Figure 4.24.	83
4.26 Affine deformation at $t = 24$ for impact on polydisperse systems modeled by different friction models; \mathbf{i} and \mathbf{j} are the unit vectors in the x and y directions; here $v = 0.7$, the other parameters are as in Figure 4.2. . . .	86
4.27 \mathcal{D}_{min}^2 distribution at $t = 24$ for impact on polydisperse systems modeled by different friction models; the parameters are as in Figure 4.26.	87
4.28 Affine deformation at $t = 24$ for impact on monodisperse hexagonal systems modeled by different friction models; here $v = 0.7$, the other parameters are as in Figure 4.2.	88
4.29 \mathcal{D}_{min}^2 distribution at $t = 24$ for impact on polydisperse systems modeled by different friction models; the parameters are as in Figure 4.28.	89
4.30 Intruder's acceleration versus its time-dependent depth, $y(t)$, and time-dependent velocity, $u(t)$. The impact velocities are $v = 0.05$, $v = 0.1$, $v = 0.2$, $v = 0.3$, $v = 0.4$, $v = 0.7$, and $v = 1.0$. The parameters that are not varied are as in Figure 4.2.	91
4.31 Intruder's total penetration depth, D , versus $H = y+$, where h is the falling distance. Here, we show $\mu = 0.0$ (red circles), $\mu = 0.5$, $k_t = 0.0$ (black squares), and $\mu = 0.5$, $k_t = 0.8k_n$ (blue diamonds). The parameters that are not varied are as in Figure 4.2.	93

LIST OF FIGURES
(Continued)

Figure	Page
4.32 Combined energy of the intruder and granular particles during impact for three systems characterized by different frictional properties; penetration depth versus time is shown in Figure 4.7. Here we show the results for: $\mu = 0$ (red dashed); $\mu = 0.5, k_t = 0.0$ (black solid), and $\mu = 0.5, k_t = 0.8k_n$ (blue dash-dot). The parameters are as in Figure 4.7.	96
5.1 Hopper Setup. Particles in the hopper are colored according to the normal force experienced. Gravitational compaction leads to larger forces in the lower parts of the hopper.	98
5.2 Survival time diagram.	100
5.3 Diagram of a hopper.	103
5.4 Distribution of survival times for $D = 2.7$ cm and $\theta = 45^\circ$. The data are obtained from 40 realizations.	107
5.5 Dependence of survival times on the outlet size.	108
5.6 Distribution of survival times as function of elapsed time from the beginning of simulations. Here, $\theta = 45^\circ$. The data are obtained from 40 realizations.	109
5.7 Mass flux for $\theta = 45^\circ$	111
5.8 Dependence of the constant k from Eq. (5.4) on the outlet angle, θ	111
5.9 Number of particles in the hopper as a function of time for different hopper angles ($D = 4.5$ cm).	113
5.10 Velocity vectors at three consecutive output times (averaged over 1/100 second). Here $D = 4.1$ cm, $\theta = 60^\circ$	113
5.11 Averaged velocity fields for outlet size of $D = 4.5$ cm and two outlet angles. Absolute values of velocity components are shown. Slight waviness next to the hopper walls is due to cell-averaging procedure.	115
5.12 Fluctuation of velocity components ($D = 4.5$ cm, $\theta = 60^\circ$).	116
5.13 Averaged pressure fields for outlet size of $D = 4.5$ cm and two outlet angles.	117
5.14 Fluctuations of pressure fields for outlet size of $D = 4.5$ cm and two outlet angles.	117
A.1 Diagram of two particles interaction.	123
A.2 Direction of ξ	124

LIST OF FIGURES
(Continued)

Figure	Page
B.1 Illustration of cells in make_list.f.	133
C.1 Continuum model results as the frequency of perturbation is modified. .	140
C.2 Continuum model results as the wavelength of perturbation is modified.	141
C.3 Continuum model results as the frequency of perturbation is modified for spatially independent perturbation.	142

CHAPTER 1

INTRODUCTION

1.1 Granular Materials

Granular materials are large conglomerations of discrete macroscopic particles [38], such as sand in an hourglass or beans in a container. Two important aspects of granular materials are that temperature plays no major role, and the interactions between grains are dissipative. Granular materials are ‘non-thermal’, i.e., thermal energy (kT) has no significant effect compared to the gravitational energy experienced by the grains. To see why this is the case, we do a rough estimate. For a typical velocity of the order of 1 cm/s and a typical mass of order 10^{-8} kg, we find that the kinetic energy $E_k = \frac{1}{2}mv^2 \approx 10^{-12}$ Joule. If this kinetic energy were caused by thermal agitation, it would correspond to a temperature of 10^{11} K. The loss of potential energy experienced by such a particle as it drops by a height of its own diameter d , is given by $\Delta E_p = mgd$, which is roughly equal to E_k , i.e., $E_k = \Delta E_p$ [21]. Thus, kT is insignificant and thermodynamics does not apply to macroscopic granular materials. The interactions between grains are basically through collisions, which are typically inelastic. Thus there is always energy loss due to inelastic collisions and friction.

1.2 Dense Jammed Granular Systems

Granular materials are different from solids, liquids, and gases. Imagine a handful of sand being poured on the floor, it flows like a liquid; while the pile on which it is poured behaves solid-like. If wind blows through the sand, it can become suspended in the air like a gas. Depending on the situation, granular materials can behave like one of those states. Thus a granular material is often referred to as ‘the 5th state

of matter' (the 4th state is plasma). If particles are densely packed, they are able to resist external applied stress like a solid. If they are loosely assembled, they may not sustain the stress and will flow instead. This transition between the solid-like phase and fluid-like phase makes granular materials unique. We usually call granular materials in the solid-like regime 'jammed granular materials'. Particles in a jammed granular material are typically in contact with a number of their immediate neighbors. The forces between the particles in jammed granular materials do not propagate isotropically, but instead are more likely to be distributed in certain directions than others [3, 13]. These preferred directions are referred to as 'force chains' - chains of contacts along which the forces are stronger than the mean inter-particle force. Many beautiful pictures, Figure 1.1 is one example, have been taken showing the existence of these force chains, whose length is much larger than a typical particle size. Due to this heterogeneity in stress distribution, describing force or energy propagation through jammed granular materials is a difficult task. In particular, it is unclear whether and how continuum models can be used for this purpose.

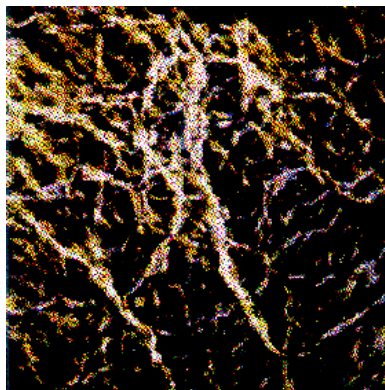


Figure 1.1 Experiment result of 3-D force chains from [3]. The bright color shows the force chains.

1.3 Literature

Sound waves have been used to study the properties of granular materials for a long time, since sound is transmitted in a media by actual contacts. In a dry granular material, sound propagates from one grain to its neighbors only through their mutual contacts and the contact law has a strong influence on sound propagation. As indicated by Hertz's law [20], which is suitable for the calculation of perfectly spherical particle collisions, the sound velocity c should vary as $p^{1/6}$, where p is the isotropic pressure applied to the granular material. Experimental results show that at low pressures, c follows a $p^{1/4}$ non-Hertzian power law [26, 27, 34]. The effect of the nonlinear contact law was also studied by Nesterenko and collaborators [57, 58, 60] from a different point of view. They considered a one-dimensional monodisperse granular chain, where all grains are in contact initially, and have shown analytically that the propagation of a weakly compressed pulse initiated in the chain can be described by the Korteweg-de Vries (KdV) equation giving solutions of a solitary wave type. When a strong pulse is applied, one also finds solitary wave solutions, but of a different kind. The solitary waves observed in this case have a finite width that is independent of the solitary wave amplitude. The existence of these solitary waves was later confirmed experimentally in [14, 45]. Since then, a number of studies has focused on the nonlinear dynamics in granular systems [14, 16, 33, 77]. Moreover, there have been recent studies on the propagation of solitary waves in the applications of detecting impurities and of energy trapping and absorption [17, 19, 32, 74].

When extending to two-dimensional or three-dimensional granular systems, the disorder in the packing of the granular materials becomes very important. Since the force chains in a disordered system through which the sound travels can be very sensitive to the local structure, even a very small change in the grain placement can cause a completely different force network. Small amplitude waves have been used to examine the structure and the nonlinear properties of this force network [40]. It is

found that at low frequencies, such that the wavelengths are very long compared to the mean length of the force chains, the materials can be regarded as a homogeneous medium. When the wavelength is comparable to the particle size, scattering effects dominate, the homogeneous description is not adequate, and the waves are determined by the exact structure of the force chains.

There has also been extensive discussion in the literature regarding continuum descriptions of stress propagation through dense jammed granular materials [25, 28, 29, 49, 53, 54, 63, 76, 81]. Some works claim that the propagation is wave-like and it should be described by a hyperbolic equation [25, 53, 54, 76, 81]. In other works, evidence of an elliptic description of stress structure is reported [28]. It has been recently revealed that these approaches may both be valid, but on different length scales [29, 49, 63]. For small systems, it is found that a hyperbolic description is valid, while for larger systems, elastic description is more appropriate.

1.4 Overview

In this work, a few different granular systems are considered and the issues of granular flow and associated energy propagation are discussed. The considered systems are all characterized by large volume fraction - they are jammed, or close to jamming. We start by considering one-dimensional model-systems in Chapter 2, which already in this simple one-dimensional geometry shows a variety of interesting features, as discussed briefly above. Two-dimensional systems are then investigated in Chapter 3 using discrete element method (DEM) simulations and the results are compared to a relatively simple continuum model.

In Chapter 4, we study on force and energy propagation in a system exposed to impact of a large scale intruder. This problem is of interest in a number of different settings, starting from astrophysical applications to various types of impact processes relevant in technological applications. Again using DEM simulations, the response

of a granular system to impact and the processes which govern this response are discussed.

The final part of this work discusses a slightly different problem of a hopper flow in Chapter 5. Hopper geometries are heavily used in a variety of technological applications, and it is of interest to understand the mechanisms determining the main aspects of the flow.

CHAPTER 2

1-D GRANULAR SYSTEMS

2.1 One-Dimensional Hertzian Chains

A significant amount of work on energy propagation mechanisms in one-dimensional particle chains was done by Nesterenko and collaborators [57, 58, 60]. In this section, we briefly summarize the analysis presented in these works.

For a one-dimensional granular chain under the Hertzian law, the force between two adjoining particles is determined by

$$F = \frac{2E}{3(1 - \sigma^2)} \left(\frac{R_1 R_2}{R_1 + R_2} \right)^{1/2} [(R_1 + R_2) - (x_2 - x_1)]^{3/2} \quad (2.1)$$

where R_1 and R_2 are the granules' radii, E is Young's modulus, σ is the Poisson coefficient, and x_1 and x_2 are the coordinates of the spherical particles' centers ($x_2 > x_1$). Assume that the particles are uniformly precompressed with the overlap δ_0 , see

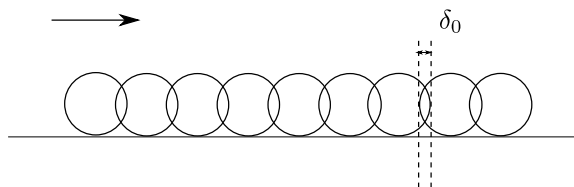


Figure 2.1 1-D granular chain of identical grains under a uniform precompression. The initial disturbance is given to the first particle on the left to the right as the arrow indicates.

Figure 2.1. The equation of motion of a particle in a chain of N identical particles is given by

$$\ddot{u}_i = A(\delta_0 - u_i + u_{i-1})^{3/2} - A(\delta_0 - u_{i+1} + u_i)^{3/2}, \quad 2 \leq i \leq N - 1, \quad (2.2)$$

$$m = \frac{4}{3}\pi R^3 \rho, \quad A = \frac{E(2R)^{1/2}}{3(1 - \sigma^2)m},$$

where u_i is the displacement of the i th granule from its initial position, and m , ρ and R are the mass, density and the radius of a particle, respectively. We consider now a chain with imposed perturbation on one side of the chain, and discuss how this perturbation propagates through the chain. Depending on the relative size of the perturbation and precompression, we find two cases.

2.1.1 Strongly Compressed Chains $|u_{i-1} - u_i| \ll \delta_0$

Under the assumption $|u_{i-1} - u_i| \ll \delta_0$, we can expand the first two terms on the right hand side of Eq. (2.2) into power series using the expansion

$$(1 + z)^n = 1 + nz + \frac{n(n-1)}{2!}z^2 + \dots, \quad |z| < 1, \quad (2.3)$$

with z being $|u_{i-1} - u_i|/\delta_0$ and $n = 3/2$. Neglecting higher order terms, the new equation of motion becomes

$$\ddot{u}_i = \alpha(u_{i+1} - 2u_i + u_{i-1}) + \beta(u_{i+1} - 2u_i + u_{i-1})(u_{i-1} - u_{i+1}), \quad 2 \leq i \leq N - 1, \quad (2.4)$$

$$\alpha = \frac{3}{2}A\delta_0^{1/2}, \quad \beta = \frac{3}{8}A\delta_0^{-1/2}.$$

Expanding the neighboring points about a central point, $u_i = u$, in power series in terms of a small parameter $\epsilon = 2R/L$ up to the fourth order where L is a characteristic spatial size of the perturbation propagation through the chain,

$$u_{i-1} = u - u_x(2R) + \frac{1}{2}u_{xx}(2R)^2 - \frac{1}{6}u_{xxx}(2R)^3 + \frac{1}{24}u_{xxxx}(2R)^4 + \dots, \quad (2.5)$$

$$u_{i+1} = u + u_x(2R) + \frac{1}{2}u_{xx}(2R)^2 + \frac{1}{6}u_{xxx}(2R)^3 + \frac{1}{24}u_{xxxx}(2R)^4 + \dots \quad (2.6)$$

Using the above replacement, Eq. (2.4) becomes

$$u_{tt} = c_0^2 u_{xx} + 2c_0 \gamma u_{xxxx} - \nu u_x u_{xx}, \quad (2.7)$$

$$c_0^2 = A\delta_0^{1/2}6R^2, \quad \gamma = \frac{c_0R^2}{6}, \quad \nu = \frac{c_0^2R}{\delta_0}.$$

Assuming u has the form $u = u(x - c_0t)$ and letting $u_x = -\xi$, Eq. (2.7) then can be transformed into the KdV equation

$$\xi_t + c_0\xi_x + \gamma\xi_{xxx} + \frac{\nu}{2c_0}\xi\xi_x = 0, \quad \xi = -u_x. \quad (2.8)$$

Start with a trial solution

$$\xi(x, t) = z(x - \beta t) \equiv z(u).$$

Substituting the trial solution into Eq. (2.8), we are led to the ordinary differential equation

$$-\beta\frac{dz}{du} + \left(c_0\frac{dz}{du} + \frac{\nu}{2c_0}z\frac{dz}{du}\right) + \gamma\frac{d^3z}{du^3} = 0.$$

Integration can be done directly. It follows that

$$-\beta z + \left(c_0z + \frac{\nu}{2c_0}\frac{1}{2}z^2\right) + \gamma\frac{dz^2}{du^2} = c_1$$

where c_1 is the constant of integration. A multiplication with dz/du yields

$$-\beta z\frac{dz}{du} + \left(c_0z\frac{dz}{du} + \frac{\nu}{2c_0}\frac{1}{2}z^2\frac{dz}{du}\right) + \gamma\frac{dz^2}{du^2}\frac{dz}{du} = c_1\frac{dz}{du}.$$

Integration of both sides again with c_2 as the constant of integration leads to

$$-\beta\frac{1}{2}z^2 + \left(c_0\frac{1}{2}z^2 + \frac{\nu}{2c_0}\frac{1}{6}z^3\right) + \gamma\frac{1}{2}\left(\frac{dz}{du}\right)^2 = c_1z + c_2. \quad (2.9)$$

It is required that in case $x \rightarrow \pm\infty$ we should have $z \rightarrow 0$, $\frac{dz}{du} \rightarrow 0$, $\frac{d^2z}{du^2} \rightarrow 0$. From these requirements it follows that $c_1 = c_2 = 0$.

With $c_1 = c_2 = 0$ Eq. (2.9) can be written as

$$\int_0^z \frac{d\zeta}{\zeta\sqrt{\frac{\beta-c_0}{\gamma} - \frac{\nu}{6c_0\gamma}\zeta}} = \int_0^u d\eta. \quad (2.10)$$

Using the transformation

$$\zeta = \frac{1}{\frac{\nu}{6c_0\gamma}} \frac{\beta - c_0}{\gamma} \operatorname{sech}^2 \omega = 6c_0 \frac{\beta - c_0}{\nu} \operatorname{sech}^2 \omega, \quad (2.11)$$

we obtain

$$\frac{\beta - c_0}{\gamma} - \frac{\nu}{6c_0\gamma} \zeta = \frac{\beta - c_0}{\gamma} - \frac{\beta - c_0}{\gamma} \operatorname{sech}^2 \omega = \frac{\beta - c_0}{\gamma} \tanh^2 \omega. \quad (2.12)$$

Furthermore we have

$$-\frac{\nu}{6c_0\gamma} \frac{d\zeta}{d\omega} = 2 \frac{\beta - c_0}{\gamma} \tanh^2 \omega \operatorname{sech}^2 \omega,$$

or

$$\frac{d\zeta}{d\omega} = -12c_0 \frac{\beta - c_0}{\nu} \frac{\sinh \omega}{\cosh^3 \omega}. \quad (2.13)$$

The upper integration limit of the left side integral in Eq. (2.10) due to Eq. (2.11) is transformed to

$$w = \operatorname{sech}^{-1} \sqrt{\frac{1}{6c_0 \frac{\beta - c_0}{\nu}}} z. \quad (2.14)$$

Substituting Eq. (2.12), Eq. (2.13), and Eq. (2.14) into Eq. (2.10), we get

$$\begin{aligned} u &= \int_0^\omega \frac{-12c_0 \frac{\beta - c_0}{\nu} \frac{\sinh \omega}{\cosh^3 \omega} d\omega}{6c_0 \frac{\beta - c_0}{\nu} \operatorname{sech}^2 \omega \cdot \sqrt{\frac{\beta - c_0}{\gamma}} \tanh \omega} \\ &= -\frac{2}{\sqrt{\frac{\beta - c_0}{\gamma}}} \int_0^\omega d\omega \\ &= -\frac{2}{\sqrt{\frac{\beta - c_0}{\gamma}}} \omega \\ &= -\frac{2}{\sqrt{\frac{\beta - c_0}{\gamma}}} \operatorname{sech}^{-1} \sqrt{\frac{1}{6c_0 \frac{\beta - c_0}{\nu}}} z, \end{aligned}$$

or

$$z(u) = 6c_0 \frac{\beta - c_0}{\nu} \operatorname{sech}^2 \left(\frac{\sqrt{\frac{\beta - c_0}{\gamma}}}{2} u \right).$$

Now we finally get

$$\xi(x, t) = 6c_0 \frac{\beta - c_0}{\nu} \operatorname{sech}^2 \left[\frac{1}{2} \sqrt{\frac{\beta - c_0}{\gamma}} (x - \beta t) \right].$$

We put

$$\xi(x, t) = 24c_0 \frac{\gamma}{\nu} W^2 \operatorname{sech}^2 [W(x - \beta t)],$$

$$W = \frac{1}{2} \sqrt{\frac{\beta - c_0}{\gamma}}$$

where W is the width of the wave and β is the wave velocity.

2.1.2 Weakly Compressed Chains $|u_{i-1} - u_i| \gg \delta_0$

Suppose the difference of displacement change between two adjacent particles is much larger than their initial compression, δ_0 , so particles are weakly compressed initially, then δ_0 can be neglected in Eq. (2.2) to give

$$\ddot{u}_i = A(u_{i-1} - u_i)^{3/2} - A(u_i - u_{i+1})^{3/2} \quad (2.15)$$

In the same way as Eq. (2.5) and Eq. (2.6),

$$u_{i-1} - u_i = -u_x(2R) + \frac{1}{2}u_{xx}(2R)^2 - \frac{1}{6}u_{xxx}(2R)^3 + \frac{1}{24}u_{xxxx}(2R)^4 + \dots = N(x) + \phi(x),$$

$$u_i - u_{i+1} = -u_x(2R) - \frac{1}{2}u_{xx}(2R)^2 - \frac{1}{6}u_{xxx}(2R)^3 - \frac{1}{24}u_{xxxx}(2R)^4 - \dots = N(x) + \psi(x),$$

$$N(x) = -u_x(2R),$$

$$\phi(x) = +\frac{1}{2}u_{xx}(2R)^2 - \frac{1}{6}u_{xxx}(2R)^3 + \frac{1}{24}u_{xxxx}(2R)^4 - \dots, \quad (2.16)$$

$$\psi(x) = -\frac{1}{2}u_{xx}(2R)^2 - \frac{1}{6}u_{xxx}(2R)^3 - \frac{1}{24}u_{xxxx}(2R)^4 - \dots \quad (2.17)$$

Now Eq. (2.15) can be written as

$$\ddot{u} = A(N(x) + \phi(x))^{3/2} - A(N(x) + \psi(x))^{3/2}. \quad (2.18)$$

Since Eq. (2.5) and Eq. (2.6) are expanded in power series of the small parameter $\epsilon = \frac{2R}{L}$, one finds

$$\frac{\phi(x)}{N(x)} \sim \frac{\psi(x)}{N(x)} \sim \epsilon,$$

Using Eq. (2.3), one obtains

$$\begin{aligned} & (N(x) + \phi(x))^{3/2} \\ &= (N(x))^{3/2} + \frac{3}{2}(N(x))^{\frac{1}{2}}\phi(x) + \frac{3}{8}(N(x))^{-\frac{1}{2}}(\phi(x))^2 - \frac{1}{16}(N(x))^{-\frac{3}{2}}(\phi(x))^3 + \dots, \\ & (N(x) + \psi(x))^{3/2} \\ &= (N(x))^{3/2} + \frac{3}{2}(N(x))^{\frac{1}{2}}\psi(x) + \frac{3}{8}(N(x))^{-\frac{1}{2}}(\psi(x))^2 - \frac{1}{16}(N(x))^{-\frac{3}{2}}(\psi(x))^3 + \dots \end{aligned}$$

where $N(x) = -2Ru_x > 0$. Using the above equations, Eq. (2.18) becomes

$$\ddot{u} \approx A \left[\frac{3}{2}(N(x))^{\frac{1}{2}}(\psi(x) - \phi(x)) + \frac{3}{8}(N(x))^{-\frac{1}{2}}(\psi(x)^2 - \phi(x)^2) - \frac{1}{16}(N(x))^{-\frac{3}{2}}(\psi(x)^3 - \phi(x)^3) \right]. \quad (2.19)$$

From the expressions for $\phi(x)$ and $\psi(x)$ (Eq. (2.16) and Eq. (2.17)), the following approximate expressions can be found:

$$\begin{aligned} \phi - \psi &\approx (2R)^2 u_{xx} + \frac{1}{12}(2R)^4 u_{xxxx} + \mathcal{O}(\epsilon^6), \\ \phi^2 - \psi^2 &\approx -\frac{1}{5}(2R)^5 u_{xx} u_{xxx} + \mathcal{O}(\epsilon^7), \\ \phi^3 - \psi^3 &\approx \frac{1}{4}(2R)^6 u_{xx}^3 + \mathcal{O}(\epsilon^7). \end{aligned}$$

Now Eq. (2.19) becomes

$$u_{tt} = c^2 \left[\frac{3}{2}(-u_x)^{\frac{1}{2}} u_{xx} + \frac{(2R)^2}{8}(-u_x)^{\frac{1}{2}} u_{xxxx} - \frac{(2R)^2}{8} \frac{u_{xx} u_{xxx}}{(-u_x)^{\frac{1}{2}}} - \frac{(2R)^2}{64} \frac{(u_{xx})^3}{(-u_x)^{\frac{3}{2}}} \right],$$

$$-u_x > 0, \quad c^2 = A(2R)^{\frac{5}{2}}.$$

And the above equation can be rewritten as

$$u_{tt} = -c^2 \left\{ (-u_x)^{3/2} + \frac{(2R)^2}{12} \left[((-u_x)^{3/2})_x x - \frac{3}{8} ((-u_x)^{-1/2}) u_{xx}^2 \right] \right\}_x,$$

Suppose u can be found in the form $u(x - Vt)$ and we introduce the new variables $\xi = -u_x$, then we obtain

$$\frac{V^2}{c^2} \xi_x = \frac{3}{2} \xi^{1/2} \xi_x - \frac{a^2}{64} \xi^{-3/2} \xi_x^3 + \frac{a^2}{8} \xi^{-1/2} \xi_x \xi_{xx} + \frac{a^2}{8} \xi^{1/2} \xi_{xxx},$$

where $a = 2R$, or

$$\frac{V^2}{c^2} \xi_x = \frac{3}{2} \xi^{1/2} \xi_x - \frac{a^2}{64} \xi^{-3/2} \xi_x^3 + \frac{a^2}{8} \xi^{-1/2} (\xi \xi_{xx})_x.$$

Integrate and suppose that as $\xi \rightarrow \infty$, $\xi \rightarrow \xi_0$, $\xi_x \rightarrow 0$, and $\xi_{xx} \rightarrow 0$, and replace ξ by $\xi = z^{4/5}$, then we have

$$\frac{V^2}{c^2} z^{4/5} = z^{6/5} + \frac{a^2}{10} z^{1/5} z_{xx} + c_1$$

where c_1 is an integration constant. Now introduce the change Change of variables,

$$y^{4/5} = y^{6/5} + y^{1/5} y_{\eta\eta} + c_2, \quad (2.20)$$

$$z = \left(\frac{V}{c}\right)^5 y, \quad x = \frac{a}{\sqrt{10}} \eta$$

where c_2 is a constant and Eq. (2.20) is in dimensionless form. We rewrite Eq. (2.20) as follows with a new constant c_3 :

$$y_{\eta\eta} = -\frac{\partial W(y)}{\partial y}, \quad (2.21)$$

$$W(y) = -\frac{5}{8} y^{8/5} + \frac{1}{2} y^2 + c_3 y^{4/5}. \quad (2.22)$$

For the special case $c_3 = 0$, we make the ansatz $y = A \cos^5(kx)$ on Eqs. (2.21) and (2.22) and find

$$k = \frac{1}{5}, \quad A = \left(\frac{5}{4}\right)^{5/2}.$$

Thus in this case,

$$\xi = \left(\frac{5V^2}{4c^2}\right)^2 \cos^4\left(\frac{\sqrt{10}}{5(2R)}x\right). \quad (2.23)$$

Unlike the solitary wave solution found in a strongly compressed chain, this wave has the same width regardless of amplitude. The width of the wave is roughly five particle diameters and is independent of system parameters.

2.2 Other Nonlinear Lattices

Solitary waves are also found in other well-known lattice-based systems. We give a brief review of two well-known ones. We will explore the similarities of the system of interest to us with these systems in the proposed work.

2.2.1 The Fermi-Pasta-Ulam Lattice

The Fermi-Pasta-Ulam (FPU) lattice is a chain of particles joined by springs which obey Hooke's law but with a nonlinear term. The equations of motion [4] are

$$\ddot{x}_i = (x_{i+1} - 2x_i + x_{i-1}) + \alpha [(x_{i+1} - x_i)^2 - (x_i - x_{i-1})^2], \quad (2.24)$$

$$\ddot{x}_i = (x_{i+1} - 2x_i + x_{i-1}) + \beta [(x_{i+1} - x_i)^3 - (x_i - x_{i-1})^3] \quad (2.25)$$

where x_i gives the i^{th} particle's displacement from equilibrium.

Eq. (2.24) and Eq. (2.25) are called *FPU* - α model and *FPU* - β model, respectively. Under the long-wave approximation, the α model can be converted into the KdV equation and the β model turns into a modified KdV equation.

2.2.2 The Toda Lattice

The Toda lattice [82] was discovered by the Japanese physicist Morikazu Toda. The basic idea of this lattice is a chain of identical particles linked by nonlinear springs.

Assume the springs have potential energy $U(r)$ where r is the distance between adjacent particles from the resting position at which the springs have minimum energy and the corresponding force

$$F = -\frac{dU}{dr}$$

is zero. If x_n still denotes the horizontal displacement of the i^{th} particle from its equilibrium, then the motion of the i^{th} particle is determined by

$$m \frac{d^2 x_i}{dt^2} = U'(x_{i+1} - x_i) - U'(x_i - x_{i-1}).$$

This gives the set of ODEs

$$m \frac{d^2 r_i}{dt^2} = \left(\frac{dU(r_{i+1})}{dr_{i+1}} - \frac{dU(r_i)}{dr_i} \right) - \left(\frac{dU(r_i)}{dr_i} - \frac{dU(r_{i-1})}{dr_{i-1}} \right) \quad (2.26)$$

where $r_i = x_{i+1} - x_i$. The Toda lattice is obtained for an anharmonic potential of the form

$$U(r) = \frac{a}{b}(e^{-br} + br - 1) \quad (2.27)$$

where $a, b > 0$. With unit masses ($m = 1$), Eq. (2.26) becomes

$$\frac{d^2 r_i}{dt^2} = a(2e^{-br_i} - e^{-br_{i+1}} - e^{-br_{i-1}}), \quad (2.28)$$

which are called the Toda-lattice equations.

In the limit $b \rightarrow 0$ with ab finite, the potential $U(r)$ is a harmonic potential, and Eq. (2.28) reduces to

$$\frac{d^2 r_n}{dt^2} = ab(r_{n+1} - 2r_n + r_{n-1}). \quad (2.29)$$

If b is large, the potential $U(r)$ appears as a hard sphere potential. Equation (2.28) has an exact solitary wave solution of the form

$$r_n = -\frac{1}{b} \log[1 + \sinh^2 \kappa \operatorname{sech}^2(\kappa n \pm t\sqrt{ab} \sinh \kappa)] \quad (2.30)$$

where κ is the amplitude parameter, see [70].

CHAPTER 3

2-D GRANULAR SYSTEMS WITH BOUNDARY EXCITATIONS

3.1 Introduction

One critical issue in the physics of granular materials is the basic physical mechanism of energy and/or stress propagation. Resolving some aspects of this issue has been a subject of numerous works. One can roughly distinguish two groups of efforts here. The first one concentrates on forces and energy fluctuations inherent in granular systems, including force transmission. The second one discusses signal (such as sound) propagation and is often based on a continuum description of a granular system. One important issue is how to link these approaches. More generally, an issue is how to connect micro- and meso- spatial scales, in addition to the relevant time scales.

In the first direction, there has been much recent debate regarding static force propagation. A substantial range of models has been proposed, with dramatically different properties. Some of these approaches, based on probabilistic model for force propagation, predict diffusive (parabolic) propagation of forces [13]. Diffusive behavior has been also reported in experiments [76], although with very small systems. Others, also probabilistic approaches, lead to a response which may be either wave-like or elastic-like [6, 7]. Related conclusions have been reached in other works [8, 64]. Assemblies of frictionless particles are shown to lead to wave-like signal propagation [81]. Recent experiments, however, seem to be consistent with an elastic response to an applied point force [24, 25, 67]. It is puzzling that in different experiments and models one can observe such a variety of signal propagation mechanisms. One wonders whether different behavior is triggered as the parameters of a granular system are modified [28, 49].

Continuum models used in the engineering literature (e.g., [27, 37, 55, 69]) commonly assume elastic or elasto-plastic response, which does not seem to be consistent with the propagating, hyperbolic (or parabolic) type of response often obtained under microscopic picture. There is a question whether the models based on elasticity theory can be used to explain signal propagation through granular systems [51]. Some progress in connecting discrete and continuum descriptions has been reached in recent works that show that the system's response may change depending on the scale: one can see wave-like response on short (meso) scales, but elastic response on larger scales [28, 29]. These works also point out that friction and anisotropy can have an important effect on force propagation. Still, there are numerous questions to be answered, even regarding relatively simple configurations of static granular material exposed to a localized perturbation.

An issue of signal, such as sound, propagation through granular systems is closely connected to force and energy propagation, although it is often treated differently. Within continuum theory, the issue of sound propagation is typically approached via effective medium theory [27, 75, 86]. Most of the works explore theoretically and experimentally the response of a granular system to a spatially independent perturbation which is large compared to a particle size, such as a piston moving in a granular system. It has been shown that the speed of signal propagation, c , follows a power law dependence on the applied pressure p , $c \propto p^\alpha$, where α typically varies between 1/6 and 1/4, although there is some discussion on how general this result is [26, 39, 40, 50, 51, 78, 86]. Furthermore, it has also been pointed out that force chains may be important in sound propagation [35, 36, 46, 47, 48]. Some recent papers try to reconcile the apparent differences between earlier works [39, 40] by pointing out that the direct and strongly scattered signal components should be treated separately. However, this issue is still not completely understood, in particular regarding propagation through fragile systems close to the rigidity threshold.

A different approach to signal propagation through granular samples is based on considering one-dimensional particle chains, which allow for formulation of continuum models from first principles, as discussed in Chapter 2. In some cases, one can even obtain closed form solutions [15, 57, 59, 73]. We note that the review [57] points out the differences in formulation between the case of compressed and uncompressed, or weakly compressed systems. In the former case, one obtains (under certain conditions) a KdV equation leading to solitary wave solutions, while the latter case leads to a more complicated nonlinear high-order wave equation. This difference may be of relevance to the properties of granular systems that are close to jamming. Additional issues of disorder, polydispersity, and different models for particle interactions enter into the problem, leading to a number of effects, some of which have been observed experimentally [14, 15, 45]. Extensions of the one-dimensional results to two-dimensional and three-dimensional geometry lead to effects which are expected to be of importance to signal propagation in physical granular systems [35, 60, 77].

In this work, we consider computationally a dense granular system exposed to a perturbation that is space and time dependent. The main motivation for using a relatively complex perturbation is that by varying the critical parameters, such as the spatial scale of the imposed perturbation, we can learn about the nature of signal propagation through the granular sample. Our computations are carried out using a discrete element method (DEM). In the last part, we present the comparison of the DEM results to the ones resulting from a relatively simple continuum model. This comparison provides further insight into the mechanisms responsible for signal propagation through dense granular matter.

3.2 Methods

We choose a relatively simple granular geometry in two spatial dimensions with the granular particles constrained between two rough walls (up-down) with periodic

boundary conditions (left-right). We use the constant volume (CV) protocol where the walls' positions prescribe the volume fraction, ρ , of the considered system; we also briefly consider the constant pressure (CP) protocol where constant load is applied to the top boundary. We consider ρ 's in the interval $[0.80 - 0.90]$ under CV protocol, and the loads which lead to similar average volume fractions for CP protocol. The particles are polydisperse disks, with the radii varying randomly in some range r about the mean. For simplicity, we put gravity to zero. Particle-particle and particle-wall collisions are modeled as described in Appendix A. Here we proceed with the simulation details which are specific to the considered problem.

The walls in the simulations are made of particles that are rigidly attached, thus creating an impenetrable boundary. The wall particles are chosen as strongly inelastic and frictional in order to reduce the reflection phenomena.

The simulations are prepared by very slow compression without applied perturbation until the required ρ is reached. After this initial stage, the system is relaxed. The upper boundary is fixed and the lower boundary is perturbed. The perturbations are of the form $z(x) = A \sin(2\pi ft) \sin(\lambda x)$, where A , f , and λ are the amplitude, the frequency, and the wavelength of the imposed perturbation, respectively. We also consider a simpler functional form $z(x) = A \sin(2\pi ft)$ corresponding to piston-like motion in and out of the domain. Formally, the limit $\lambda \rightarrow \infty$ reduces the more complex form to the simpler one. This form is chosen so that ρ is kept constant in time.

Particle properties: The (Normal) spring constant is given value of $k_n = 4000$; we use the tangential spring constant $k_t = 0.8k_n$. Dissipation is specified by γ_n and γ_t which are given the values leading to the coefficient of restitution $e_n = 0.5$, defined in Appendix A; polydispersity is $r = 0.1$; the coefficient of friction is $\mu = 0.5$. The wall particles are characterized by $e_n = 0.1$, $\mu = 0.9$, and are taken as monodisperse

Table 3.1 Parameters of the Model

Parameter	Value
particle diameter d	4 mm
collision time t_{col}	7.0×10^{-4} s
normal spring constant $k_{n,p}$	656.5 N/m
friction constant μ	0.5

$r = 0.0$. Table 3.1 lists the values of parameters, which correspond to the typical photoelastic disks used in experiments at Duke [24].

System properties: The perturbation as described above is applied by perturbing the lower wall which defines the x axis; typically 40,000 particles are used, with the x dimension of the system being $250 d$. The reason for using so many particles is to reduce the boundary effects. The typical volume fraction is $\rho = 0.90$.

Perturbation properties: Amplitude $A = 0.6 d$; $f = 30$ Hz. First we consider the system characterized by infinite λ (spatially uniform perturbation) and then consider finite λ 's. Typically $\lambda = 250 d$. These values are used in all the simulations except if specified differently. The particular numerical values used for the perturbation are chosen so that wave propagation can be clearly observed.

The results that follow are given in dimensionless form, using average mass of a particle as a mass scale, collision time as the time scale, and average particle diameter as the length scale. In some cases, it is convenient to also present the results using the scales related to the properties of the imposed perturbation. These cases are clearly marked.

3.3 Results

In this section, we start by considering the simplest case of infinite wavelength perturbation (essentially a piston moving in and out) in Section 3.3.1. In Section 3.3.2, we will consider the case of finite wavelength perturbations and use this example to illustrate the influence of the spatial structure of the perturbation on the propagation. In Sections 3.3.3 and Section 3.3.4, we discuss the influence of the parameters. In Section 3.3.5, we will digress briefly from considering the constant volume setup to discuss the modifications of the results if the system is instead constrained by constant applied load.

3.3.1 Infinite Wavelength Perturbation

We first consider the limit $\lambda \rightarrow \infty$ with the main goal of connecting our results to the existing experiments and simulations [35, 39, 40, 46, 47, 48, 51, 78, 86]. We note here that there are still many open questions regarding signal (sound) propagation through granular matter. Some works argue that force chains and their response to applied perturbation are important in understanding the system response [35], while others do not find force chains important [51]. Also, other works find that signal speed (measured by the time of flight) in their DEM simulations is 40% more than what would be expected based on elasticity theory [78]. These differences could possibly be a result of different scales and the nature of the experiments and simulations; for example, it is not obvious that the results of the approach that measures system response to an infinitesimal compression or shear [51] can be directly related to continuous and often strong perturbation used in other works [35, 78].

Figure 3.1 shows snapshots of the forces that granular particles experience at four different times during one period of the boundary motion right after the creation of perturbation at the lower wall. The color scheme shows the forces on particles, with blue (dark) corresponding to low, and green-yellow/light to large forces (force is

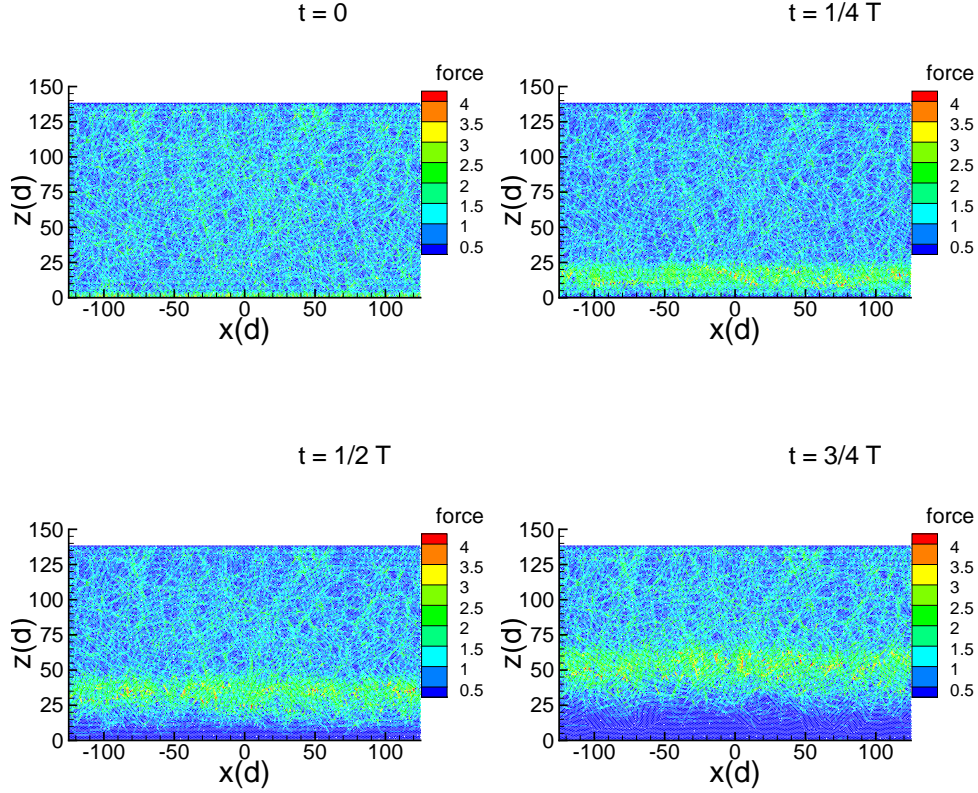


Figure 3.1 Total force on granular particles at four different phases during one period of the boundary oscillation; The upper wall is static, and the lower one performs standing type of motion. In this and the following figures, we use $r = 0.1$, $f = 30$ Hz, amplitude $A = 0.6 d$, and 40,000 particles except if specified differently.

normalized by the mean). We note the force chains in the interior of the domain, as typically observed for dense granular systems.

While the evolution, dynamics, and distribution of force chains are of significant interest in understanding dense granular systems (see e.g., [35, 78]), in what follows we concentrate on the system quantities which can be averaged over a volume which is small compared to the system size, but still includes a relatively large number of particles: we use a network of 64×64 rectangular cells for spatial averaging. We also average over time intervals long compared to t_{col} , but short compared to $1/f$. The

results do not depend on the details of the averaging procedure, for the conditions specified above.

The averaging procedure is illustrated by considering the local elastic energy, E , defined as the cell average of the compression energies contained in the individual collisions taking place in a given cell during the specified time-averaging period. More precisely, elastic energy in a given cell l is defined by

$$E_l = \frac{1}{N_t n_l} \frac{k_f}{2} \sum_{k=1}^{N_t} \sum_{j=1}^{n_l} \sum_{c=1}^{n_{c,j}} [x_{j,c}]^2, \quad (3.1)$$

where $x_{j,c}$ is the compression of particle j due to the collision c , normalized by the average particle diameter, d . Next, n_l is the number of particles in the cell l at a given time, and \bar{n}_l is the average number of particles during the period of $k = 1$ to $k = N_t \gg 1$ time steps (in practice, the averaging time scale is sufficiently short so that to a high degree of accuracy $n_l = \bar{n}_l$). Collisions may last over relatively long times, but even the fastest collisions are well resolved due to the short simulation time step.

A similar averaging procedure is carried out for other quantities, such as kinetic energy of the granular particles. The considered quantities are calculated by averaging over a large number (typically 30) periods of the boundary motion in order to increase the signal to noise ratio, and to ensure that we are not seeing transient effects. For the same reason, initial results obtained for the first few periods of the oscillations are discarded. In addition, we have verified the steady nature of the results by carrying out the selected simulations for much longer time periods.

Figure 3.2 shows the results for the elastic energy obtained using the averaging procedure described above, for the same system and at the same times as shown in Figure 3.1. For this particular case, we observe wave-like propagation of energy through the system. Analysis of this propagation is the main focus of the discussion that follows.

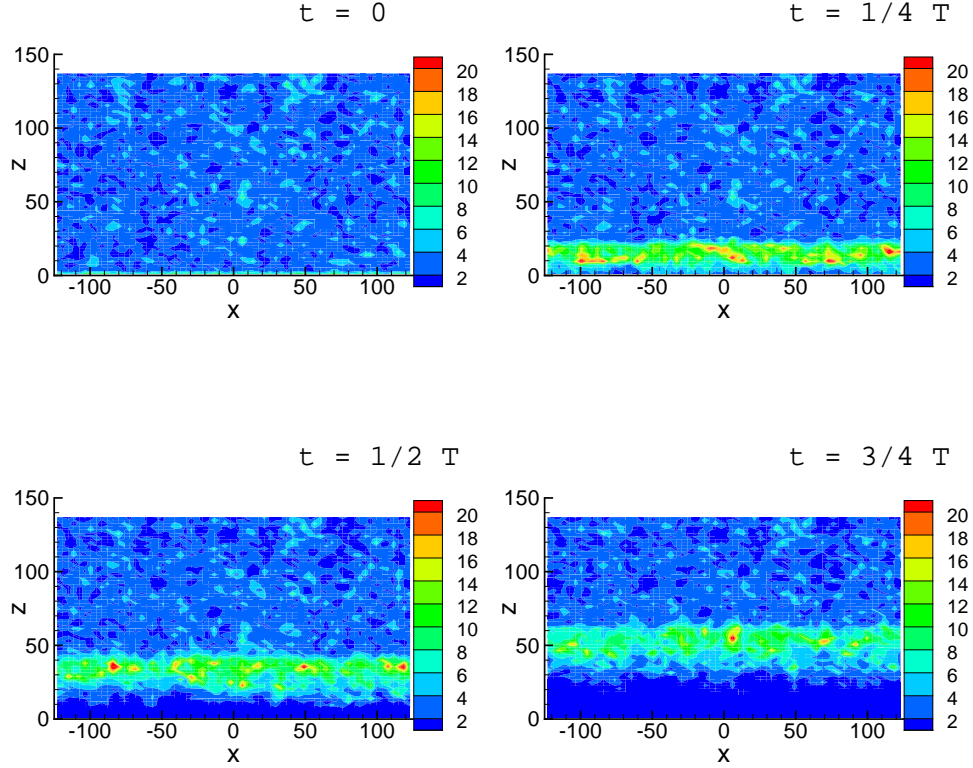


Figure 3.2 Elastic energy at four times during one period of the boundary oscillation; The upper wall is static, and the lower one moves in and out.

Figure 3.3 justifies concentration on the elastic energy. This figure shows elastic and kinetic energies averaged over the x direction and over time, for different frequencies of the boundary motion. We uniformly find that the elastic energy is significantly larger than the kinetic one, particularly away from the moving boundary. Even close to the moving boundary, the energy contained in the elastic degrees of freedom is at least a couple of times larger than the kinetic one, except for the highest frequency of driving (shown in part d) of Figure 3.3). We note in passing that the relation between kinetic and elastic energies is connected to collisional and streaming contributions to the total stress [10, 11].

To analyze the properties of propagation and their dependence on the perturbation itself, we carry out a Fourier transform FZ-AXAT (Fourier expansion in the z direction

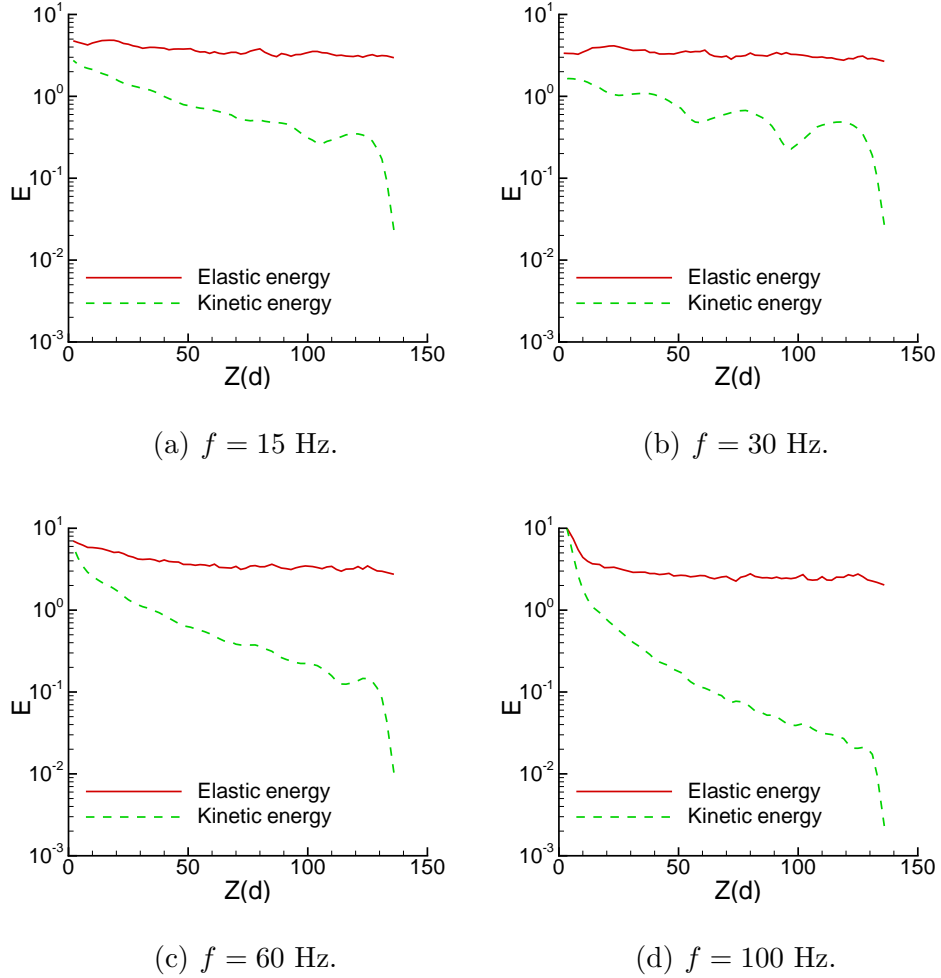


Figure 3.3 Elastic and kinetic energy of the granular particles as the frequency of the perturbation on the lower boundary is modified.

and then average over the x direction and time) of the particle elastic energy, which provides information about the wavelength chosen by the system in the z direction. FZ-AXAT is obtained from the simulations carried out with perturbation frequencies $f = 15, 30, 60$ and 100 Hz, and are given in Figure 3.4. The FZ-AXAT's show that the dominant modes for propagation in the z direction increase from 1 to 5 as the frequency is increased, although for higher frequencies we find the presence of multiple modes, suggesting stronger dispersion. We emphasize the long time averaging is used to obtain the results in this figure (and the figures below); therefore the structures

shown in the figures are not traveling waves but instead a combination of traveling and standing waves. In this work, we do not concentrate on the details of this combination, but simply ask whether the waves are present or not.

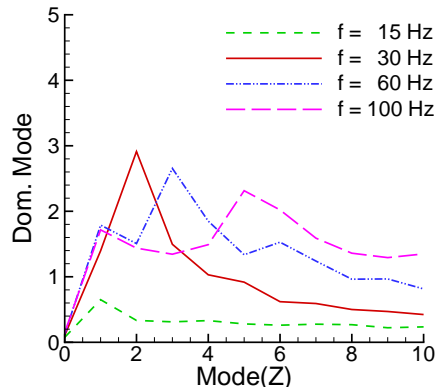


Figure 3.4 Fourier spectrum (FZ-AXAT) of the elastic energy for four representative frequencies of boundary excitations.

Next we measure the speed of propagation by examining the time interval required for information about the perturbation to reach the top wall. Figure 3.5 shows the results for the force experienced by the particles close to the walls (more precisely, in the center cells adjacent to the top and bottom walls) as a function of time. We find that approximate speed (sound speed in the system) is $c \approx 2.0$. Additional simulations with different perturbation frequencies give similar results for the sound speed. We will use this result to discuss a continuum model of energy propagation.

The continuum model to which we use for comparison in general includes elastic behavior and diffusive damping. We chose such a model since static force transmission well above jamming densities is, to date, best described in terms of an elastic picture [24, 29], and because we expect dissipative processes. Assume that the space-time properties of E are given by

$$\nabla^2 E - \frac{1}{c^2} \frac{\partial^2 E}{\partial t^2} - \frac{1}{D} \frac{\partial E}{\partial t} = 0, \quad (3.2)$$

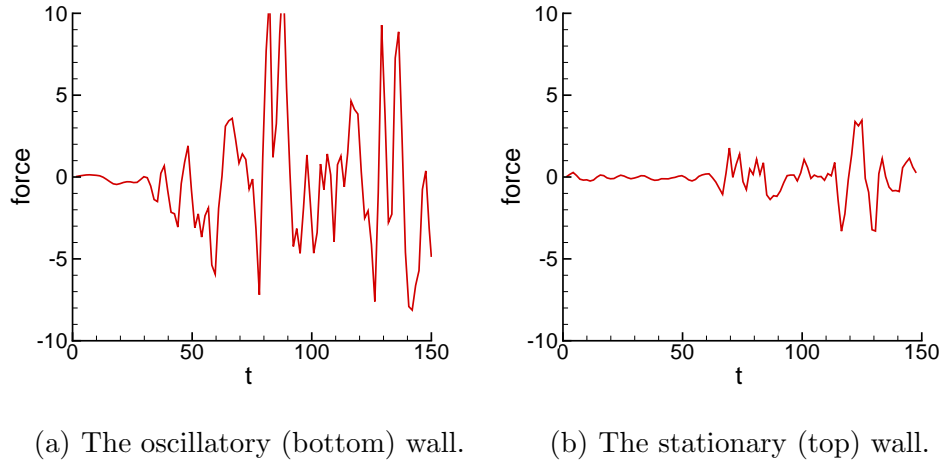


Figure 3.5 Total force on the particles close to the boundaries.

which as $D \rightarrow \infty$ becomes a linear wave equation often used to describe wave propagation in elastic solids, and as $c \rightarrow \infty$ a diffusion equation (see [39]). Equation (3.2) is given in a dimensionless form. We take the diffusion D , and the speed of propagation, c , as constants. We emphasize that this model is not meant as a full description of the data, but only a basis for comparison; discussion regarding various nonlinear effects relevant to compressed granular matter can be found in, e.g., [57] and references therein.

Here we discuss the predictions of this simple model for the one-dimensional case of Equation (3.2) in the limit of no damping. In Appendices C.1, we derive the results for the complete two-dimensional case (where the perturbation itself depends on x) and where damping is included. In this simple case of spatially independent perturbation with no damping, the dispersion relation is simply $\omega = cq$, where $\omega = 2\pi f$, and q is the wave number specifying the wavelength $2\pi/q$ of the propagating waves in the z direction. With the value of c as given above, we find that the obtained value of q closely corresponds to the dominant mode obtained from the Fourier transform of the DEM results shown in Figure 3.4. Note that exact comparison of numerical values cannot be expected to be very precise due to the fact

that the system chooses either an integer or half integer number of waves in the domain. More explicit comparisons can be also carried out as discussed in Appendix C.1 where we present the results of a continuum model including damping. Figure C.3 shows the predicted results which agree well with what is seen in the DEM simulations - compared with the dominant mode results shown in Figure 3.4. Therefore, at least approximately, we find that the simple wave equation explains reasonably well the main features of the propagation waves in the system where the perturbation itself is spatially independent. In what follows, we consider spatially dependent perturbations and discuss whether the above conclusions extend to this more complex case.

3.3.2 Finite Wavelength Perturbation

In this section, we discuss finite wavelength perturbations. We first concentrate on the signal characterized by the wavelength $\lambda = 250 d$ (equal to the domain size), frequency $f = 30$ Hz, and amplitude $A = 0.6 d$. Polydispersity is characterized by $r = 0.1$. We will refer to this configuration as the ‘basic case’. Later in the section, we will discuss the influence of f , λ , and other parameters on the results.

Figure 3.6 shows the elastic energy of the granular particles at a few different phases during one period of the boundary oscillation. We note the clear and well defined wave form propagating from the lower boundary towards the upper boundary.

To discuss more precisely the properties of the signal, it is convenient to consider again Fourier transforms (FT’s). Significant information about the signal can be obtained from two-dimensional (2D) FT (Fourier transforms in the x and z direction, averaged over time). Figure 3.7 shows the result: we see the dominant modes for this case being the mode 1 in the x -direction, and the mode 2 in the z -direction. Note that the system is divided into 64×64 cells, and the central row/column corresponds to the 0 mode. Instead of considering this 2D FT for the other configurations to be discussed below, we find it convenient to consider instead simpler FT in the x

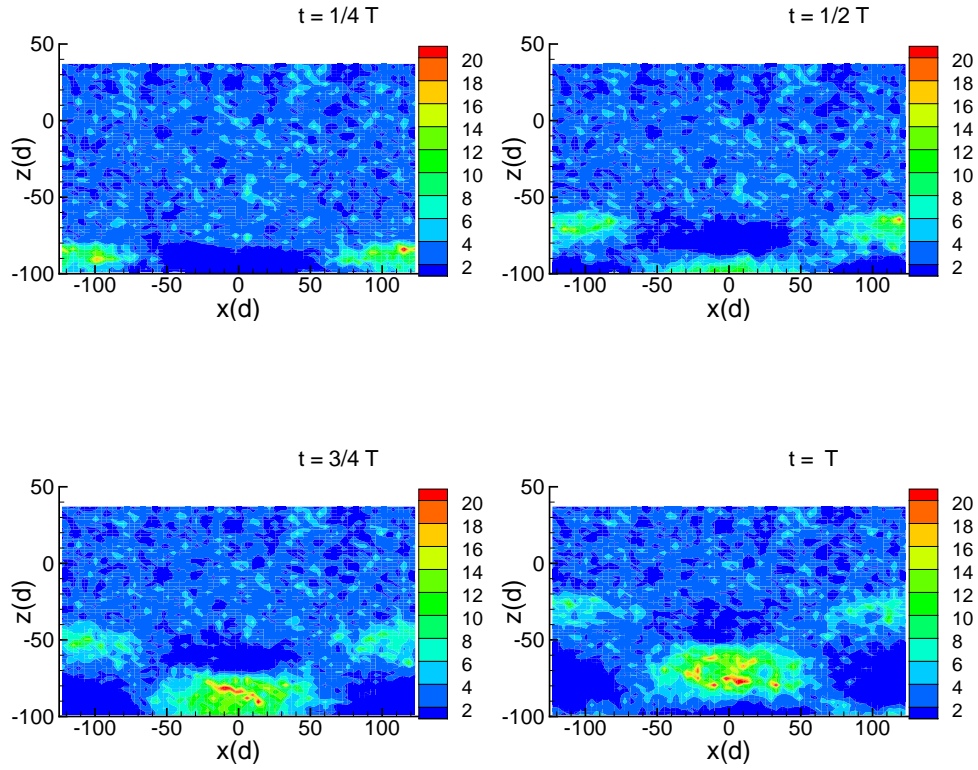


Figure 3.6 Elastic energy at four times during one period of the boundary oscillation; The upper wall is static, and the lower one performs standing type of motion. In this and following figures, we use $r = 0.1$, $f = 30$ Hz, $\lambda = 250 d$, $A = 0.6 d$, and 40,000 particles except if specified differently.

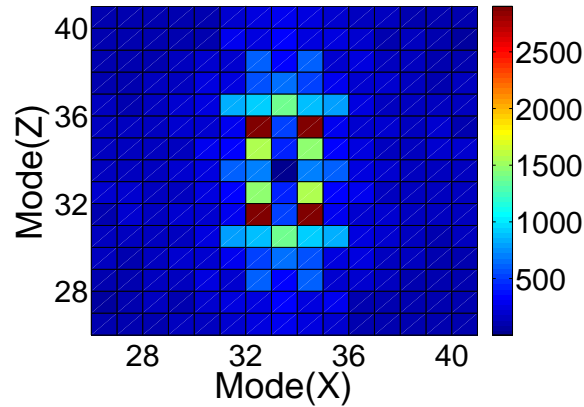


Figure 3.7 Two-dimensional Fourier transform of the elastic energy for the ‘basic’ case ($\lambda = 250 d$, $f = 30$ Hz, $A = 0.6 d$). The system is divided into 64×64 cells and the central row/column corresponds to the 0 mode in the x/z directions, respectively.

direction only, followed up by the time averaging, and consider the dependence of the FT on z ; this FXAT (Fourier in x , average in time) provides information on how well the properties of the original signal are preserved as it propagates through the system. Note that these FT's are different from the ones used in the one-dimensional case (FZ-AXAT).

Figure 3.8 shows the FXAT of the elastic energy. The part a) shows the spectral power, and the part b) the amplitude of the imposed (dominant) Fourier mode of the signal, as a function of z . We see essentially damped wave-like propagation of the energy away from the boundary.

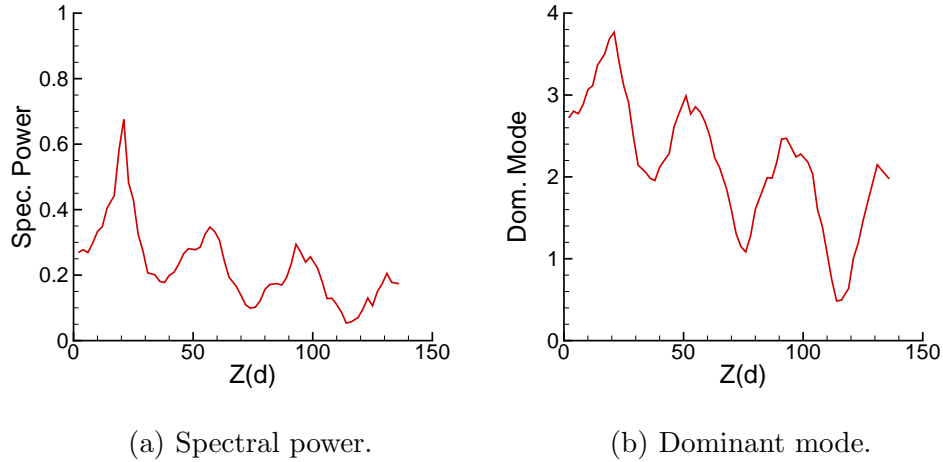


Figure 3.8 Fourier spectrum (FXAT) of the elastic energy as a function of z , the distance from the shearing wall.

3.3.3 Parametric Dependence I: System Parameters

An obvious question is whether the behavior as illustrated in the proceeding section is general. Do we expect similar kind of behavior for the systems consisting of different types of particles, or different volume fractions, for perturbations characterized by different amplitudes and/or frequencies? Do the results depend on the system size? We answer these questions here. Note that we use $r = 0.1$, $f = 30$ Hz, $\lambda = 250 d$, $A = 0.6 d$ except if specified differently.

Reproducibility Figure 3.9 shows the results for FXAT for three systems prepared independently. These results suggest that the main features of the results are independent of the initial condition.

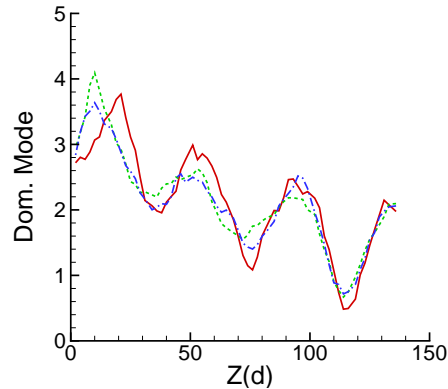


Figure 3.9 Fourier spectrum (FXAT) of three independently prepared systems.

System size dependence Figure 3.10 concentrates on the possible dependence of the results on the system size in the x direction. Here we keep the perturbation wavelength the same ($\lambda = 125 d$), and carry out simulations in different domain sizes. We see that the main features of the results are similar although they differ in details (clearly, different initial conditions had to be used for these simulations, so part of the difference may be attributed to the dependence on the initial configuration of particles). We have also considered the influence of the domain size in the z direction, by changing the total number of particles from approximately 40,000 to 50,000 (the domain size in the x direction is kept fixed to $250 d$). Figure 3.11 shows the corresponding results, where we see that the larger domain can accommodate an additional $1/2$ wavelength, but aside from this obvious change, the results are consistent between the two different domain sizes - most importantly, there is no change of the dominant Fourier mode describing propagation in the z direction.

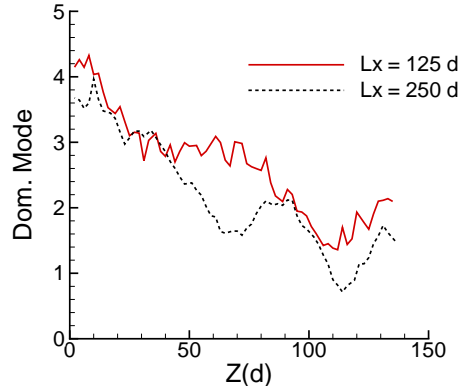


Figure 3.10 Fourier spectrum (FXAT) in two systems where the domain size in the x direction is varied. $Lx = 250 d$ (solid line) and $Lx = 125 d$ (dashed line) are shown. Here $\lambda = 125 d$.

Force model dependence The simulations that we typically carry out are performed using a given value of dynamic friction and coefficient of restitution. One may ask what is the influence of these quantities, as well as of the static friction, which is not included in the force model that we use in this work.

Figure 3.12 shows the Fourier spectrum (FXAT) of the elastic energy for different restitution coefficients. e_n is reduced from 0.9 to 0.5 and we see the results are almost indistinguishable. Modifying e_n does not influence the properties of the propagating waves. In Figure 3.13, $\mu = 0.0$ and $\mu = 0.5$ (Model I), together with $\mu = 0.5$ (Model II) (see Appendix A), are presented. The similarity of the results obtained using Model I shows that in this (kinetic friction based) model, friction does not have an influence on the properties of the propagating signal. The results obtained using Model II are however different. We find that the wavelength characterizing the propagation is longer, leading to a smaller number of waves in the considered domain. To understand the reason for this difference, we recall that the dispersion relation in the simplest case (ignoring damping, and for infinite wavelength of perturbations) suggests that the wavenumber, q , describing the propagation in the z direction is inversely proportional to the speed of sound ($\omega \approx cq$). Therefore, we recalculated

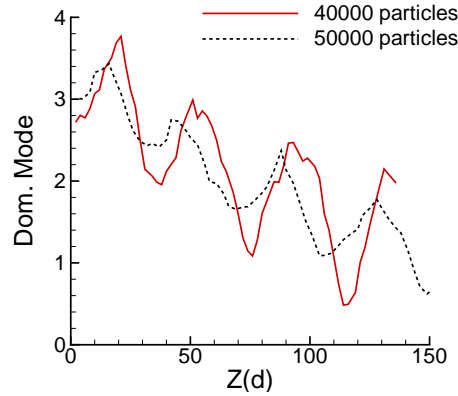


Figure 3.11 Fourier spectrum (FXAT) in two systems where the domain size in the z direction is varied. The simulations with 40,000 particles (solid line) and 50,000 particles (dashed line) are shown.

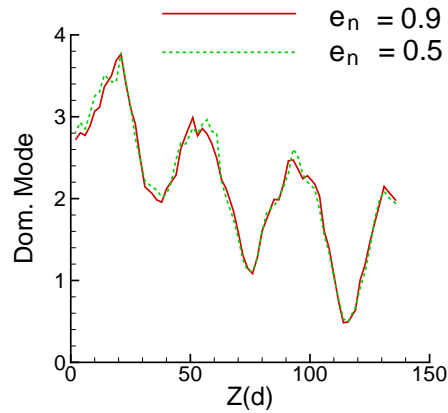


Figure 3.12 Fourier spectrum (FXAT) of the elastic energy for different elastic particle properties.

the speed of sound using a similar approach as discussed in connection to Figure 3.5 and found that the speed of sound is indeed larger in the system with static friction (Model II), reaching the value of $c \approx 2.4$. This larger speed of sound leads to smaller q and larger wavelength, as illustrated in Figure 3.13.

Stiffness of the particles The force constant, k_n , in our simulations can be easily related to the material properties, Young modulus and Poisson's ratio, as discussed in, e.g., [43]. One could ask what is the influence of these material properties

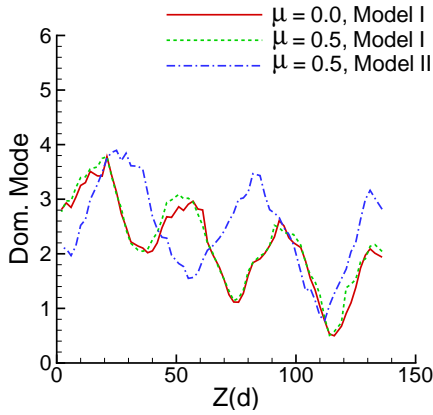


Figure 3.13 Fourier spectrum (FXAT) of the elastic energy for different elastic and frictional particle properties. Influence of dynamic and static friction : $\mu = 0$ (solid line, model I), $\mu = 0.5$ (dotted line, model I) and $\mu = 0.5$, $k_t = 0.8k_n$ (dashed line, model II) are shown.

(or, correspondingly of the force constant) on the propagating signal. Within the linear force model, the force constant defines one of the time scales of the problem, the typical time two colliding particles spent in contact (assuming only two-body interactions). The collision time t_{col} and spring constant k_n is related by $t_{col} \propto 1/\sqrt{k_n}$ (see Appendix A). Another obvious time scale is $1/f$, where f is the frequency of perturbation. So, the question is whether changing both time scales, but keeping their ratio constant would lead to the same or similar results.

Figure 3.14 shows the results for three different k_n 's and frequencies of driving. These curves were normalized and scaled by the value of the dominant mode of the 'basic case' at $z = 0$ and by its amplitude (the difference between the first maximum at $z \approx 20$ and the first minimum at $z = 0$) in order to remove the influence of much larger input energy in the case of larger frequency of perturbation. With the scaling and normalization as described, we find that the curves collapse very well, suggesting that the above time scale argument is satisfied to a high degree of accuracy.

We note that we have also carried out simulations with Hertzian interaction between the particles (normal force proportional to $x^{3/2}$) with very similar results as the ones presented here.

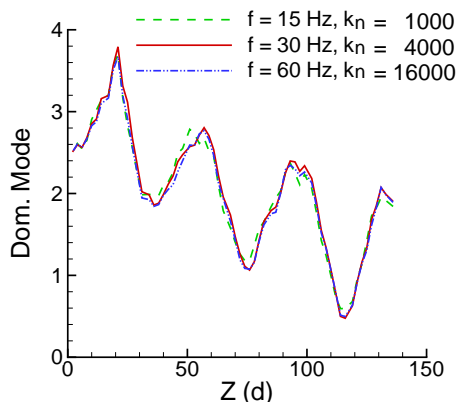


Figure 3.14 Fourier spectrum (FXAT) in the systems where the stiffness of the particles as well as the frequency of driving were modified, but their ratio was kept constant.

Volume fraction Figure 3.15 shows that a decrease of volume fraction leads to a loss of well defined properties of the propagating signal, compared to the basic case $\rho = 0.90$. This change is due to the fact that the number of contacts between particles is smaller and they are easier to break, thus reducing the energy propagation. Figure 3.16 shows this number of contacts for the three considered volume fractions - clearly, in particular close to the oscillating wall, the number of contacts is significantly smaller for smaller values of ρ . These results were obtained by averaging over the whole duration of simulation, after removing the initial transient part. We will discuss in Section 4.5 in much more detail the influence of closing and opening contacts on the process of energy propagation.

Polydispersity Figure 3.17 shows FXAT for the systems characterized by different degrees of polydispersity. We see that the main features of the results do not depend on this system property, as long as there is some degree of polydispersity. But

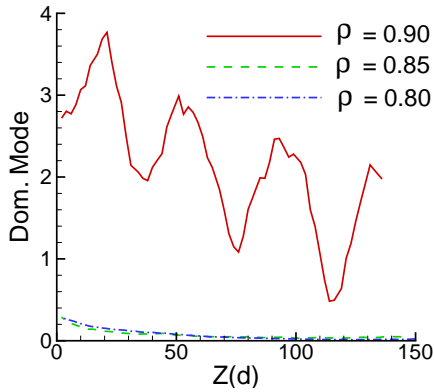


Figure 3.15 Fourier spectrum (FXAT) of three systems whose only difference is the volume fraction: $\rho = 0.90$ (solid line) $\rho = 0.85$ (dashed line) and $\rho = 0.80$ (dotted line).

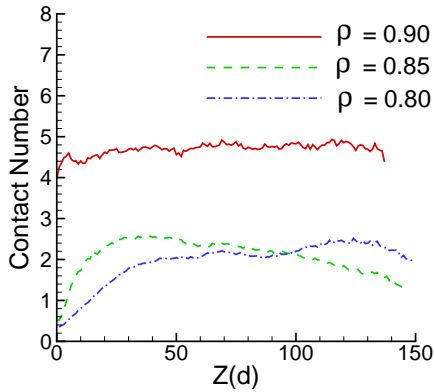


Figure 3.16 Numbers of contacts for $\rho = 0.90$ (solid line), $\rho = 0.85$ (dashed line) and $\rho = 0.80$ (dotted line).

when the system becomes monodisperse, well defined propagating signals are lost. An insight into this result can be reached by considering the total elastic energy. Figure 3.18 shows that this energy is much smaller in the monodisperse systems, compared to polydisperse cases. This is a consequence of better packing of monodisperse particles, leading to a weaker interaction between the particles under the constraint of fixed volume. Compressing the monodisperse system further, in order to reach the elastic energy roughly comparable to the one of polydisperse systems, brings us back to well-defined propagating signal.

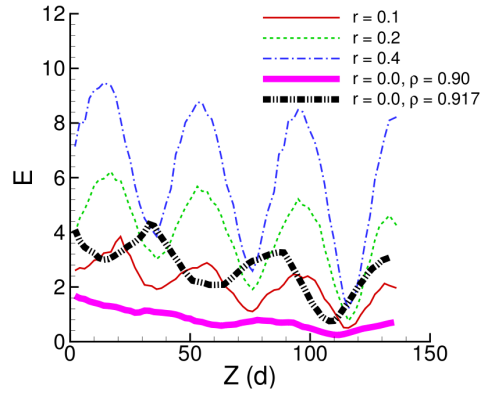


Figure 3.17 FXAT and elastic energies as polydispersity is changed from $r = 0.1$ (basic case, solid line) $r = 0.2$ (dashed line) $r = 0.4$ (dotted line), and for two monodisperse systems: $\rho = 0.90$ (thick solid line) and $\rho = 0.917$ (thick dashed line).

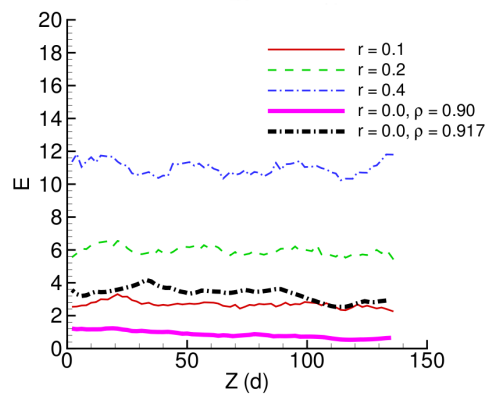


Figure 3.18 For $\rho = 0.917$, the average elastic energy of the monodisperse particles is similar to the average elastic energy of the polydisperse case $r = 0.1$.

3.3.4 Parametric Dependence II: Perturbation Properties

The imposed perturbation is defined by three parameters: the amplitude A , frequency f , and wavelength λ . The influence of the amplitude is the most straightforward and we consider it first.

Figure 3.19 shows the results where the amplitude of the perturbation is modified. While smaller/large amplitudes lead to smaller/large values of the amplitude of the dominant modes, the response of the system is qualitatively the same, suggesting that amplitudes of perturbations do not influence the properties of the propagation signal. This is important, since this result suggests that exact properties of the perturbation are not crucial, and that the conclusion reached here are not influenced by the strength of perturbation.

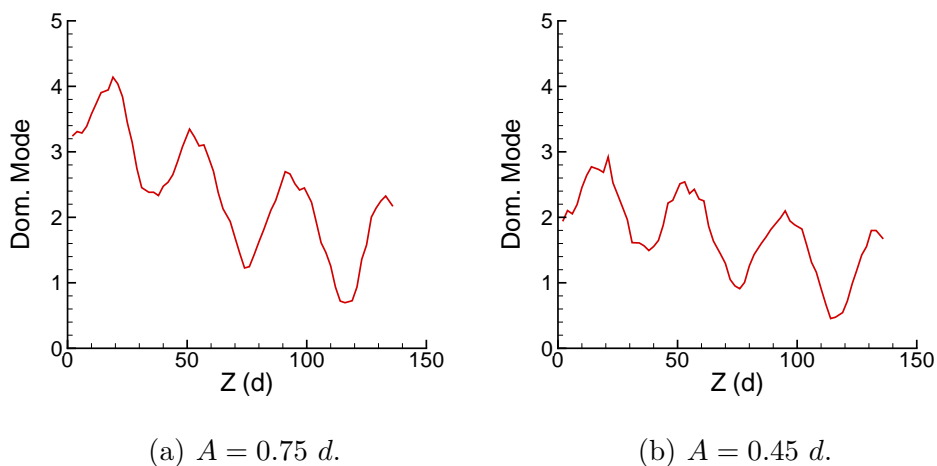


Figure 3.19 FXAT as the amplitude, A , of imposed perturbation is modified.

Figure 3.20 shows the results where the wavelength of the imposed perturbation is modified. In part a), where $\lambda = 125 d$, the main difference compared to the basic case characterized by $\lambda = 250 d$ shown in Figure 3.8 is that stronger attenuation of the signal as one moves away from the boundary. Figures 3.20 c) and d) show that as λ is further decreased, the attenuation becomes even stronger and a wave-like form of the propagating signal is completely lost. Note that although λ is significantly

decreased, it is still large compared to particle size. Therefore, we are not in the regime where the imposed length scales are so small that the particle size should be important.

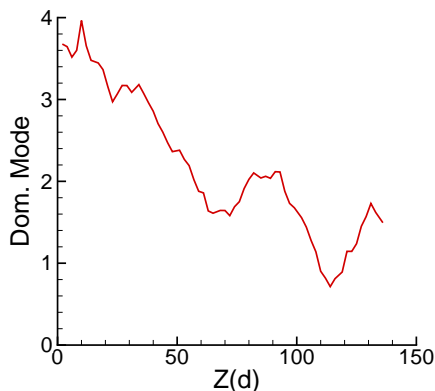
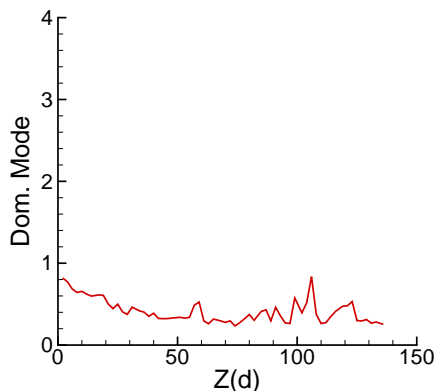
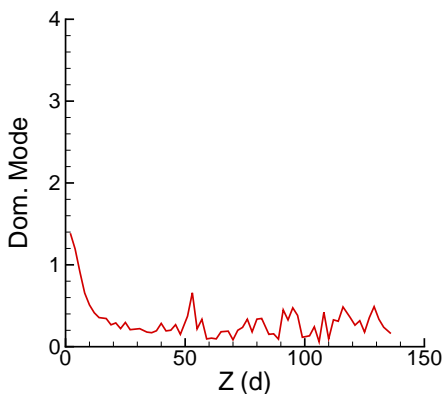
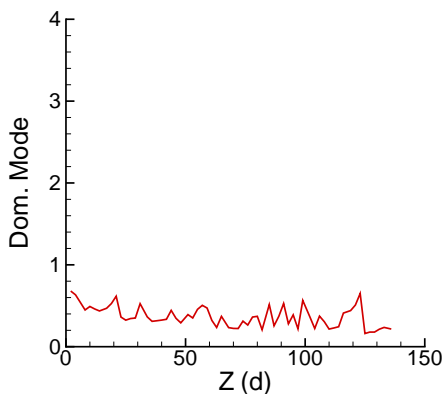
(a) $\lambda = 250 d/2$.(b) $\lambda = 250 d/4$.(c) $\lambda = 250 d/8$.(d) $\lambda = 250 d/16$.

Figure 3.20 FXAT as the wavelength of imposed perturbation is decreased.

Figure 3.21 shows the result where λ is kept fixed, but the frequency, f , is modified. We see that the imposed frequency has a strong influence on the signal properties. Well-defined wave propagation only exists in certain range of frequencies, which is consistent with what we found for infinite wavelength perturbation in the previous section.

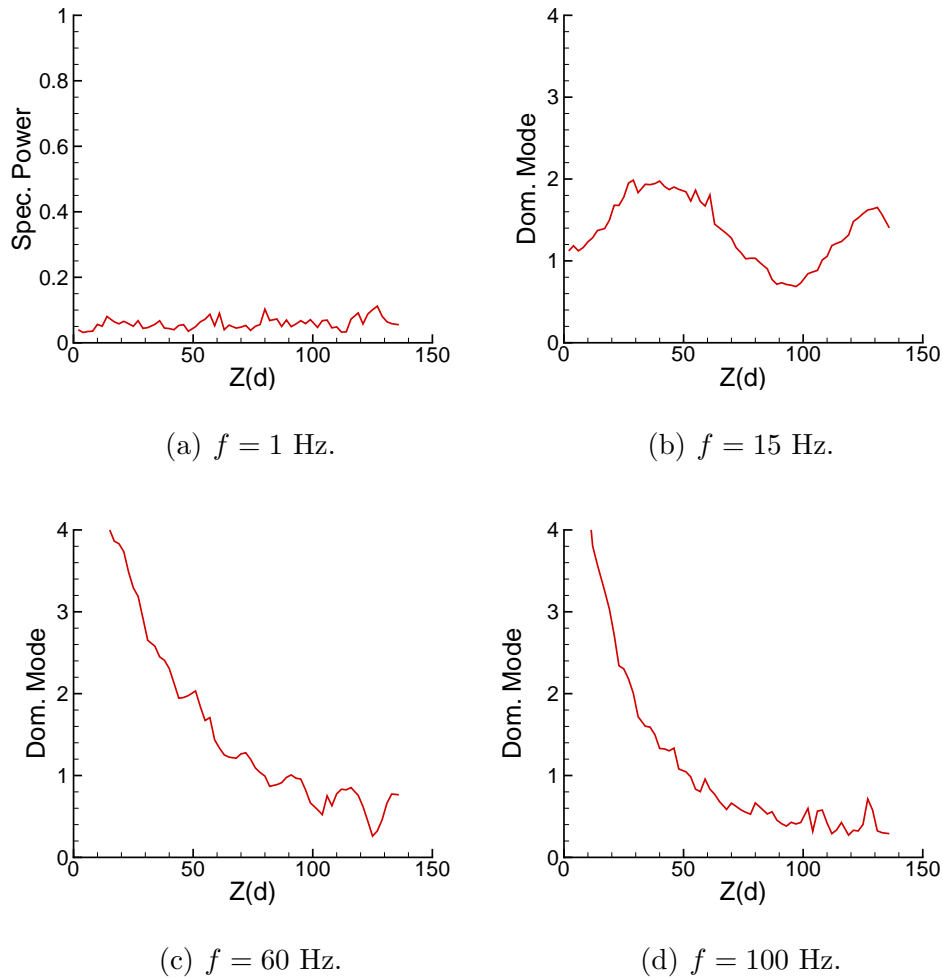


Figure 3.21 FXAT as the frequency, f , of imposed perturbation is modified. Spectral power is shown in part a) since dominant mode could not be clearly identified.

Before proceeding, we digress briefly to consider the Fourier transform in the z direction (FZ-AXAT) discussed in more detail for infinite wavelength perturbations in Section 3.3.1. Over there, we found shift to larger wavelengths as the frequency perturbation was increased. Figure 3.22, which shows the results for the perturbation of $\lambda = 250 d$, suggests that the main features of the results follow the same trend as in the case of spatially independent perturbations. The main difference is slightly lower amplitudes of the dominant mode.

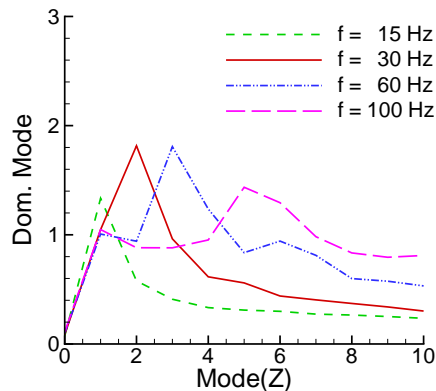


Figure 3.22 Fourier spectrum (FZ-AXAT) of the elastic energy for four representative frequencies of boundary excitations with $\lambda = 250 d$.

3.3.5 Constant Pressure (CP) System

So far, we have considered signal propagation under the constant volume (CV) protocol. Another commonly used protocol (particularly in experiments) is the constant applied pressure. To consider such a system, we apply a constant force to the top wall and let it find its own equilibrium position. We define the (constant) pressure, P , applied on the top wall as the applied force divided by the length of the top wall. This pressure is given in the unit of m/t_{col}^2 . We chose the value of applied pressures in such a way that the typical volume fraction is between 0.87 and 0.90.

Based on the results presented so far, in particular regarding the influence of the volume fraction on the properties of propagating waves, we expect that systems exposed to large pressures would lead to better propagating waves. Figure 3.23 shows that this is indeed the case: as the applied pressure is decreased, the wave-like properties of the propagation gradually disappear, similarly as if the volume fraction were decreased under the CV protocol. So systems under the large applied pressure behave similarly as the large volume fraction systems.

Figure 3.24 shows that the analogy between the CV and the CP protocols extends qualitatively to the response to the perturbations of shorter wavelengths. The main difference is that the wave-like propagation is less-visible in the CP case

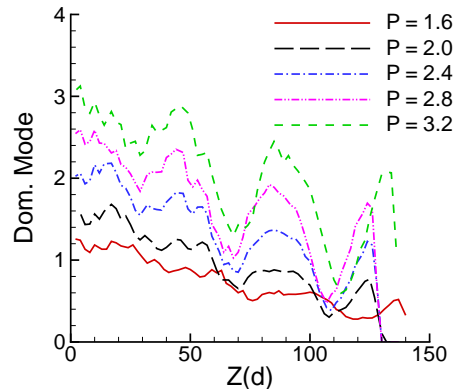


Figure 3.23 Dominant Fourier mode (FXAT) as applied pressure is varied.

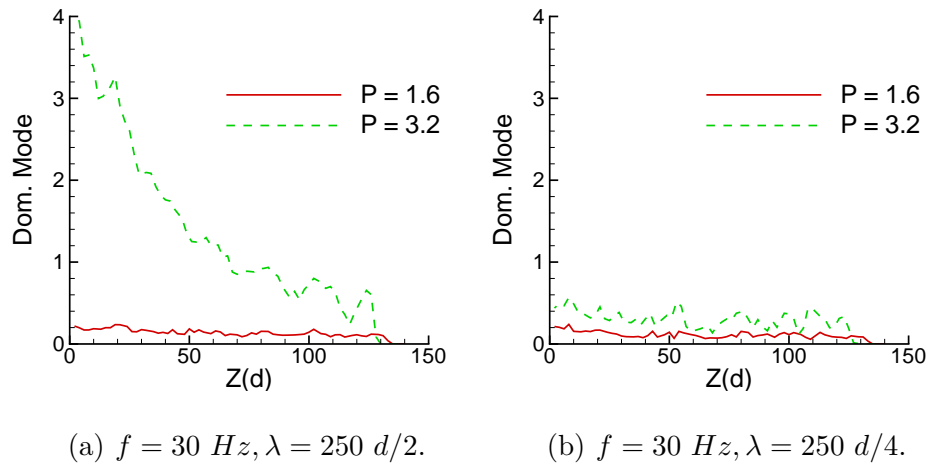
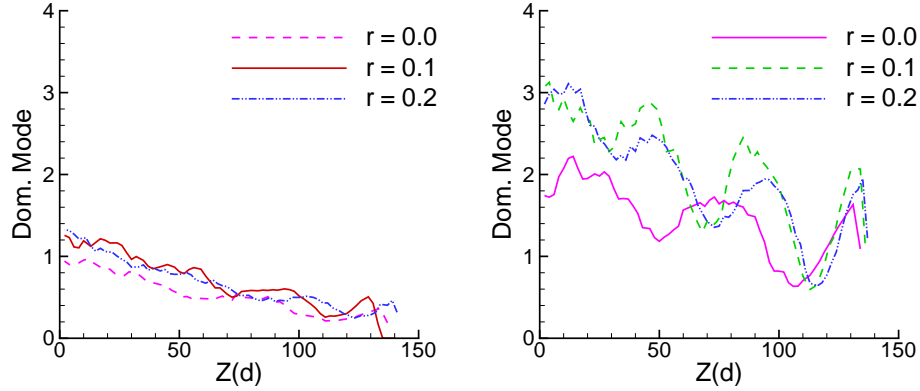


Figure 3.24 Dominant Fourier mode (FXAT) as the wavelength, λ , and frequency, f , of imposed perturbation are varied.

for the perturbations characterized by $\lambda = 250 d/2$, shown in part a) of this figure. Similar results are found as the frequency of perturbation is modified.

Next we consider the influence of polydispersity of granular particles. Figure 3.25 shows that here the differences between CV and CP protocols become more obvious, particularly for larger applied pressures shown in part b). The difference occurs for the monodisperse case. Recall that for CV protocol, the total elastic energy of monodisperse system is smaller than for the polydisperse ones, viz. Figures 3.17 and 3.18. This is, however, not the case for CP case, since here the pressure applied to the



(a) $f = 30$ Hz, $\lambda = 250$ d, $P = 1.6$. (b) $f = 30$ Hz, $\lambda = 250$ d, $P = 3.2$.

Figure 3.25 Dominant Fourier mode (FXAT) of systems with different pressures and different polydispersities, r .

top boundary determines the total elastic energy. Therefore, monodisperse system is compressed more strongly (larger volume fraction results) for the monodisperse case, leading to wave-like propagation of energy. Furthermore, the speed of the sound in the monodisperse system is slightly larger, leading to longer wavelengths, as it can be seen in Figure 3.25 b) for $r = 0.0$.

Despite the outlined differences between CP and CV, we find that the systems exposed to either CV or CP protocols behave similarly. We will therefore proceed with discussing the CV case only, with the results easily extendable to the CP case.

3.4 Discussion

Here we proceed with the discussion of the results presented so far. First we will discuss in more detail the agreement between the DEM simulations and the continuum model, which we have introduced when discussing infinite wavelength perturbations. Next, we will consider additional quantities which will help us understand more precisely the mechanism responsible for energy propagation.

3.4.1 Continuum Model

Following Eq. (3.2), assuming a plane wave solution as a zeroth order approximation to more complex waves that can be expected in dense granular matter [35, 57, 73] in the form

$$E(x, z, t) = E_0 e^{i\omega t} e^{ikx} e^{iqz},$$

we obtain the dispersion relation

$$q^2 + k^2 - \frac{\omega^2}{c^2} - \frac{\omega}{D}i = 0,$$

or

$$\omega = \pm c \sqrt{k^2 + q^2 - \frac{c^2}{4D^2}} + i \frac{c^2}{2D} = i \frac{c^2}{2D} \pm K,$$

If $k^2 + q^2 < \frac{c^2}{4D^2}$, then ω is pure imaginary. There is no propagation. If $k^2 + q^2 > \frac{c^2}{4D^2}$, then solutions are in the form as $e^{-\frac{c^2}{2D}t} e^{i(kx+qz \pm Kt)}$. In this case, K is the angular frequency and $c^2/(2D)$ is a damping parameter. The wave speed is given by

$$v = \frac{\pm K}{\sqrt{k^2 + q^2}} = \pm c \sqrt{1 - \frac{c^2/(4D^2)}{k^2 + q^2}}.$$

For higher wave numbers, $v = c$; For lower wave numbers, v decrease to zero when $k^2 + q^2 = c^2/(4D^2)$.

Back to the DEM results, for relatively large k and q , the wave speed v is relatively large, so we believe that waves travel faster and are quickly damped out. This leads to the loss of energy propagation we observe for high frequency perturbation. The model agrees with the DEM results. In Appendix C.1, we obtain the exact solution to the boundary value problem. The constant c is obtained as described earlier, and the constant $D = 2.5 \times 10^2$ is measured using the damping parameter $\frac{c^2}{(2D)}$ on the DEM results.

3.4.2 Particle Scale Response

Here we discuss response of the system to imposed perturbation on the particle scale. This approach is useful to clarify some aspects of the large-scale wave propagation. For this purpose, we compute affine and non-affine (conforming and non-conforming) components of the particle motion. The implemented procedure is described in Appendix D.

Affine Motion Figure 3.26 shows the affine component, $\mathbf{A}_f = \mathbf{A} \cdot (\mathbf{r}(t) - \mathbf{r}(t - \delta t))$, of particle dynamics at a given time for our ‘basic’ system. We see that the affine part of the motion still shows wave-like properties as expected from the results shown up to now. Figure 3.27 shows the influence of the frequency (part a) and of the wavelength (part b) on the affine component. We see that in both cases, the affine component decreases very quickly away from the oscillating boundary.

We have also computed Fourier transform of the affine component. Figure 3.28 shows the results of FXAT transforms for few selected systems. Similarly as it was found in analysis of ‘raw’ DEM results in Section 3.3.3, we see wave-like propagation for our ‘basic’ system (part a)), while change of the frequency or wavelength of the imposed perturbation leads to a quick decay of the amplitude of the dominant mode. Note also that larger frequency (parts c) - d) of this figure) lead to much larger amplitude of the affine component, compared to lower frequency shown in parts a) - b). To conclude, we find that the intensity of the affine component of particle dynamics is strongly correlated with the wave-like propagation of energy.

Non-Affine Motion We proceed by discussing non-affine component of particle motion, computed in the Appendix D. This component is quantified via quantity \mathcal{D}_{min} which measures the non-affine component: large \mathcal{D}_{min} corresponds to large non-affine part of the particles’ dynamics. This discussion will let us understand better various

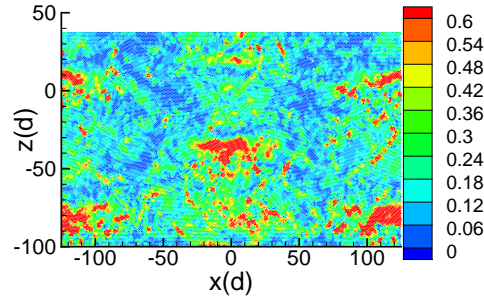
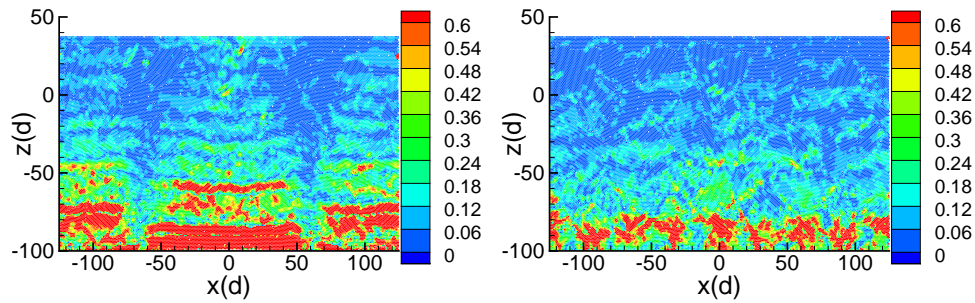


Figure 3.26 Affine component of particle dynamics for the ‘basic’ system ($f = 30$ Hz, $\lambda = 250 d$) at $t = 240$.



(a) $f = 100$ Hz, $\lambda = 250 d$.

(b) $f = 30$ Hz, $\lambda = 250 d/4$.

Figure 3.27 Affine component of particle dynamics at $t = 240$ for specified systems.

features of energy transport discussed up to now, and their dependence on the system properties.

Figures 3.29 and 3.30 show the snapshot of non-affine component of particle motion together with the number of contacts which particles experience. In Figure 3.29, which presents the results for monodisperse case, $r = 0.0$, we see formation of zones with the boundaries characterized in part b) of the figure by smaller number of contacts. Visual comparison of the parts a) and b) of this figure suggests correlation between the zone boundaries and the areas of large non-affine motion. Therefore, we

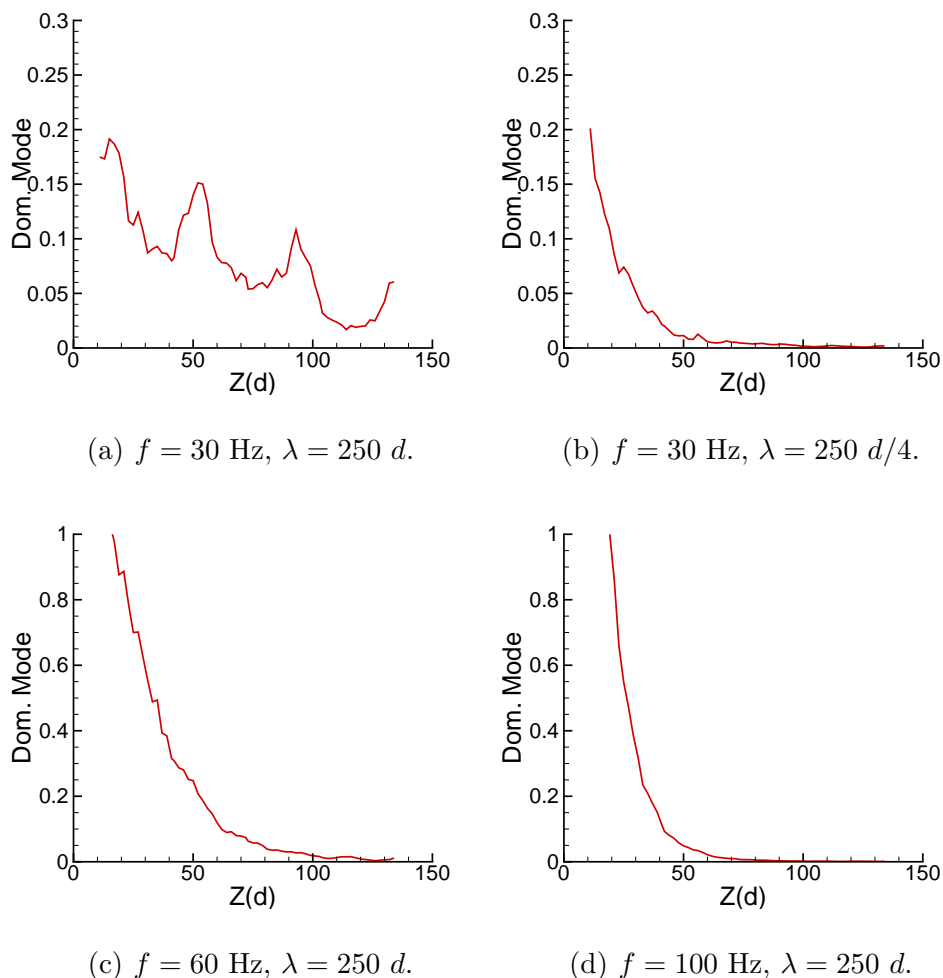


Figure 3.28 Fourier transform (FXAT) of the affine component of particle dynamics. Note different scales in a) - b) versus c) - d).

can conclude that non-affine component of particle motion is concentrated in the areas with smaller contact number Z 's. Even small amount of polydispersity is sufficient to remove both the zone formation and the correlation between Z 's and the non-affine component of particle motion measured by \mathcal{D}_{min} , as shown in Figure 3.30. We note in passing that the areas of large non-affine deformation occur in the parts of the domain where the affine component is large as well: compare Figures 3.30 b) and 3.26.

In attempt to further quantify the differences between monodisperse and polydisperse systems, we have computed pair correlation function, $g(r)$, which essentially provides

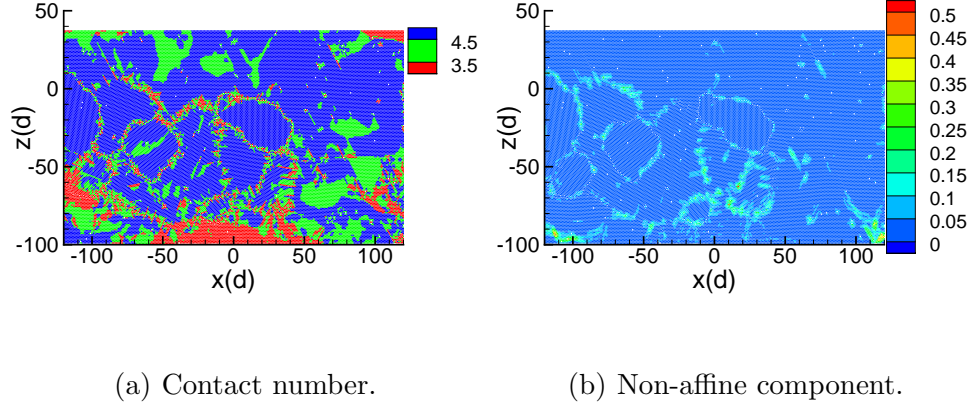


Figure 3.29 Monodisperse system ($f = 30$ Hz, $\lambda = 250 d$). The results are shown at $t = 240$.

information about the degree of ordering (crystallization) in the system. The pair distribution function is formally defined by

$$\begin{aligned}
 g(r) &= \frac{V}{N^2} \langle \sum_i \sum_{j \neq i} \delta(\mathbf{r}_i) \delta(\mathbf{r}_j - \mathbf{r}) \rangle \\
 &= \frac{V}{N^2} \langle \sum_i \sum_{j \neq i} \delta(|\mathbf{r}_{ij}| - r) \rangle
 \end{aligned}$$

where N is the total number of particles and V is the volume. This function gives the probability of finding a pair of particles a distance r apart, relative to the probability expected for a completely random distribution at the same density.

The δ function is replaced by a function which is nonzero in a small range of separations, i.e., $\delta r = 0.2 d$, and the maximal distance we examine is $r_{max} = 10 d$. All the target particles are in the domain $10 d$ away from the top and bottom boundaries. For each particle, we take its position as the center and find the numbers of particles in the rings $[k\delta r, (k+1)\delta r]$, $k = 0, \dots, r_{max}/\delta r$, respectively. These numbers are saved in $b(k)$ accordingly. We carry out this process for all the particles and N_{step} time steps, so that $b(k)$ has the total number of particles for the k th ring. We normalize this number by $n(k) = b(k)/(NN_{step})$. Assume the average number of particles in the

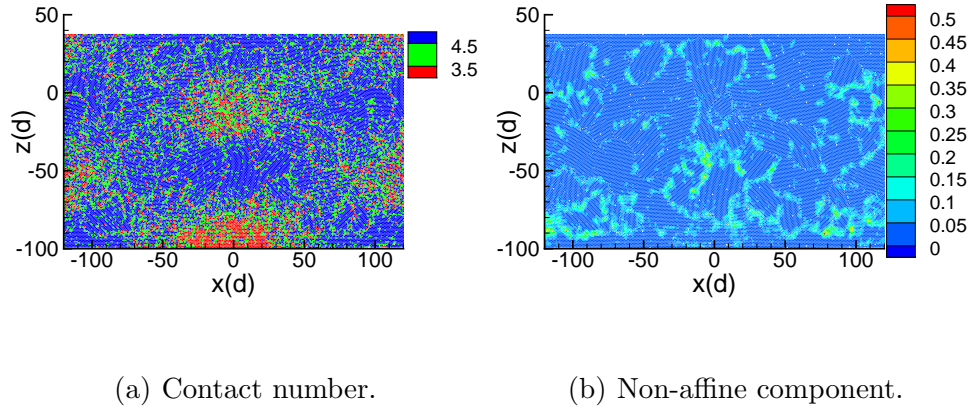


Figure 3.30 Monodisperse system ($r = 0.0$). The results are shown at $t = 240$.

same range in a completely random material at the same volume fraction ρ is

$$n^{id}(k) = \pi\rho\{[(k+1)\delta r]^2 - (k\delta r)^2\} .$$

Then the pair distribution function is defined by

$$g(k\delta r + \delta r/2) = \frac{1}{NN_{step}} \frac{b(k)}{n^{id}(k)}$$

Figure 3.31 shows the results. While we find certain degree of ordering which decays as polydispersity is increased, we do not find a significant difference in $g(r)$ between the monodisperse case ($r = 0.0$) and the smallest polydispersity used ($r = 0.1$). This observation suggests that considering $g(r)$ is not sufficient to understand the differences between mono- and polydisperse system, and furthermore that some degree of ordering of particles is not crucial for the process of energy propagation.

Additional insight can be reached by computing the correlation between the quantities of interest computed at different times. Here we consider only the contact number correlations. Figure 3.32 shows these correlations computed as follows. Choose a random particle, and find its' current number of contacts (for simplicity, we separate the particles in two groups: those having $Z \leq 3$ and those characterized by $Z \geq 4$).

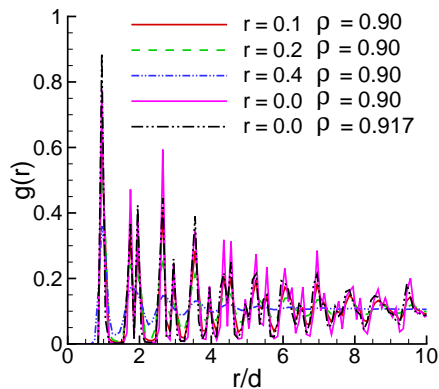


Figure 3.31 Pair-pair correlation function for the systems characterized by different polydispersities and volume fractions.

Then, follow this particle in time and record whether it still belongs to the same group, according to the Z value. Repeat for all particles. Finally, compute the probability that if particle belongs to one of the two groups at time t_0 , it will belong to the same group at the time t_i . The results shown in Figure 3.32 a) are intriguing, since they suggest that to a large degree there are always the same particles whose contacts open and close during boundary oscillations. On the time scale shown in the figure, there is no visible decay of correlations: if a particle belongs to a given group, at time t_0 , there is a high probability that it will belong to the same group at the time $t = t_0 + 1/f$, where f is the frequency of the boundary motion. Figure 3.32 b) shows much smaller degree of correlation for the monodisperse system, particularly for the particles characterized by $Z \leq 3$. Note that higher probabilities for $Z \geq 4$ (for both mono- and polydisperse systems) show that only small percentage of contacts is broken during the time corresponding to a large number of oscillations of the boundary.

Next we discuss the influence of the frequency and wavelength of perturbation on the number of contacts and non-affine component of particle dynamics. Figures 3.33 and 3.34 both show slightly decreased number of contacts next to the oscillating boundary. Much more prominent feature of the results is how strong non-affine

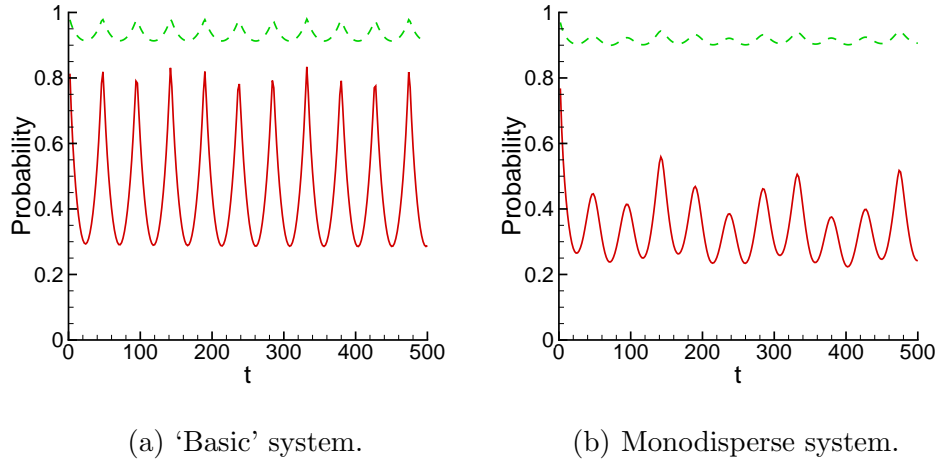


Figure 3.32 The probability that number of contacts of a given particle remains through time in one of the considered groups: $Z \leq 3$ shown by the red (solid) curves, and $Z \geq 4$ shown by the green (dashed) curves. The period of oscillations corresponds to the motion of the boundary.

component close to the oscillating boundary. To confirm that this is general feature of the results, Figure 3.35 shows the non-affine component averaged over the x direction and over time. We see large \mathcal{D}_{min} for short wavelengths and high frequencies of perturbations, consistently with the snapshots shown in Figures 3.33 and 3.34. These results suggest strongly that non-affine part of the particle motion is responsible for removal of wave-like propagation of energy, at least for the considered configurations.

For completeness, Figure 3.36 shows the correlation plots similar to Figure 3.32. We find similar degree of correlation as for the 'basic' case, still suggesting that to a large degree, the same contacts break up as time evolves.

3.5 Conclusions

In this work, we have discussed the energy propagation through dense granular system. We find that the main features of the propagation can be reasonable well described by a continuum model based on linear wave equation with damping. To reach this finding, we found it useful to consider space-time dependent perturbation of

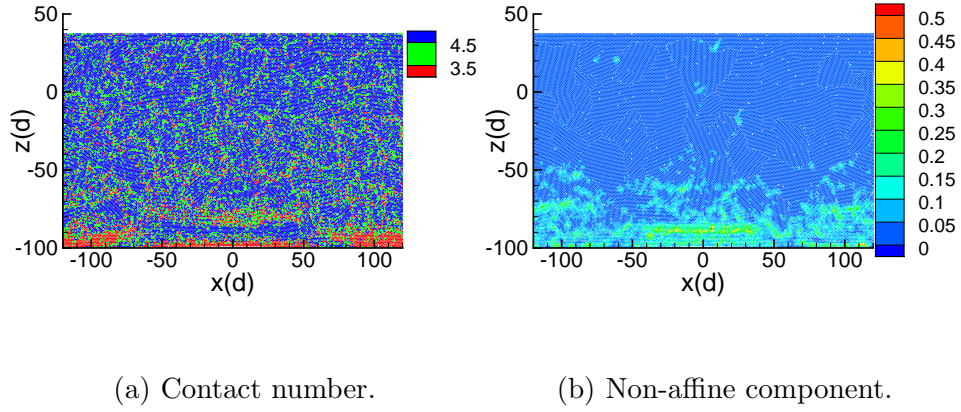


Figure 3.33 High frequency driving $f = 100$ Hz ($\lambda = 250 d$, $r = 0.1$). The results are shown at $t = 240$.

the boundary since this type of excitation provides additional parameter (in our case the wavelength of the imposed perturbation) which can be used to test the prediction of a continuum model. We find that the influence of this additional parameter is non-trivial: excitations characterized by the wavelengths which are smaller than approximately 100 particle diameters lead to stronger dispersion and loss of the wave-like properties of the signal propagation from the boundary excitation. To analyze more precisely the source of this dispersion for the perturbations which are still considerably larger than the particle size, we have computed affine and non-affine components of particle dynamics. The affine parts agree well the predictions of the continuum model, as expected. We find however strong non-affine component of particle dynamics close to the source of the signal (oscillating boundary). We conjecture that this strong non-affine component leads to significant energy loss and that it is responsible for the loss of wave-like properties of propagation energy pulse. We expect that this finding will serve as a basis for the future work which should discuss the exact mechanisms which determine the length scale on which non-affine part of particle dynamics becomes significant.

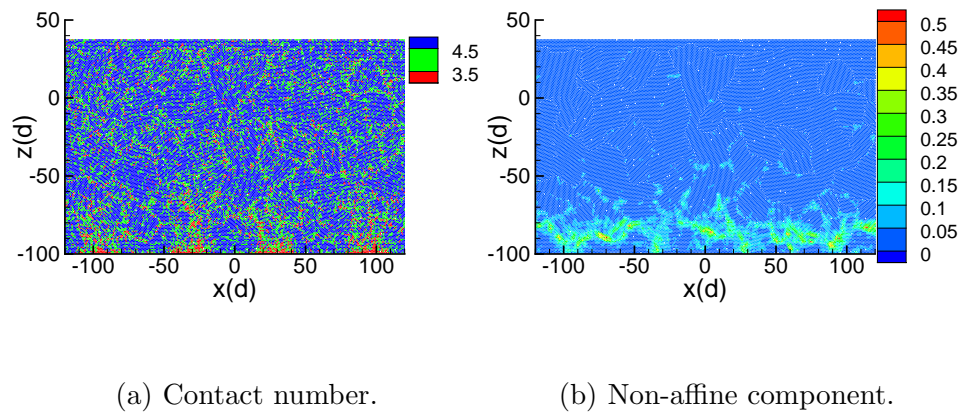


Figure 3.34 Short wavelength perturbation: $\lambda = 250 d/4$ ($f = 30$ Hz, $r = 0.1$). The results are shown at $t = 240$.

One interesting and perhaps unexpected result is that we find very satisfactory description of the main features of energy propagation based on a simple linear model involving wave equation with damping, without the need to consider complex nonlinear models discussed in Chapter 2. Our results suggest that similarly good type of agreement can be reached if Hertzian force model is used.

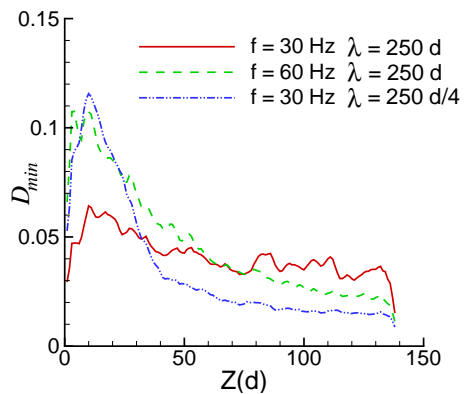
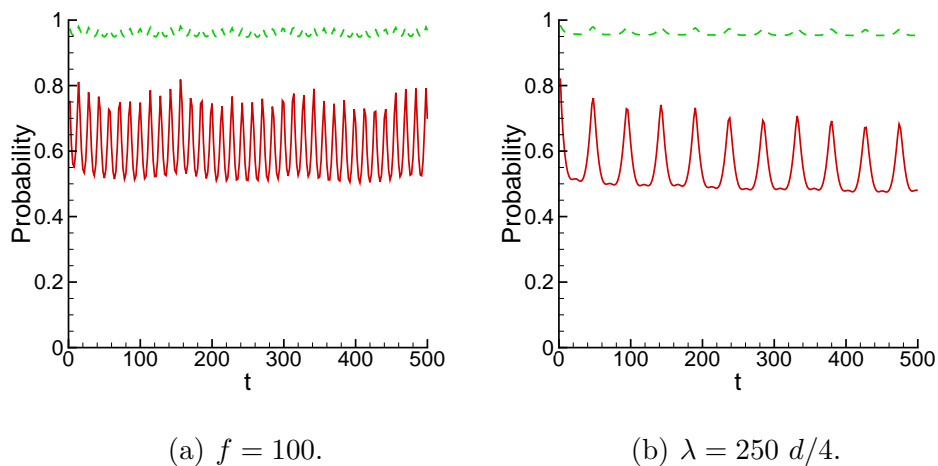


Figure 3.35 Non-affine component as a function of the distance from the oscillating boundary for few frequencies and wavelengths of the perturbations. Here $r = 0.1$.



(a) $f = 100$.

(b) $\lambda = 250 d/4$.

Figure 3.36 The probability that number of contacts of a given particle remains through time in one of the considered groups: $Z \leq 3$ shown by the red (solid) curves, and $Z \geq 4$ shown by the green (dashed) curves. The period of oscillations corresponds to the motion of the boundary.

CHAPTER 4

IMPACT ON 2-D GRANULAR SYSTEMS

4.1 Overview

We study the impact of an intruder on a dense granular material. The process of impact and interaction between the intruder and the granular particles is modeled using discrete element simulations in two spatial dimensions. In the first part of this chapter, we consider the influence on impactor dynamics of 1) the intruder's properties, including its size, shape and composition, 2) the properties of the grains, including friction, packing, and elasticity, and 3) the properties of the system, including its size and gravitational compaction. It is found that packing and frictional properties of the granular particles play a crucial role in determining impact dynamics. Then, we proceed to consider the response of the granular system itself. First, we discuss the force networks that develop, including their topological evolution. The role of friction and packing on force propagation, including the transition from hyperbolic-like to elastic-like behavior is discussed as well. Then, we discuss the affine and non-affine components of the grain dynamics. Several broad observations include the following: tangential forces between granular particles are found to play a crucial role in determining impact dynamics; both force networks and particle dynamics are correlated with the dynamics of the intruder itself.

4.2 Introduction

The problem of impact on a dense granular material has been explored extensively due to its relevance to processes that vary from asteroid impact, numerous technological applications, defense from high speed projectile impact, or to simply walking on a sandy beach. While a large amount of research has been done over hundreds of years,

only during last few decades has significant progress been reached in formulating relatively simple but realistic effective models which characterize the basic features of the interaction between an intruder and a granular material itself.

These effective models have allowed for much better understanding of the dependence of the forces due to impact on various parameters. A simple model due to Poncelet and dating from the 19th century is based on the concept that the force experienced by an intruder may be separated into independent speed- and depth-dependent parts [65]. The speed-dependent part is hydrodynamic-like, while the depth-dependent part is considered to be due to forces of either hydrostatic or frictional origin. While careful experiments [1, 2, 12, 18, 31, 42, 84, 85] and simulations [9, 12, 62, 72, 83] have improved our understanding of the physics of impact considerably, they have also opened a new set of questions. Some of these questions include scaling of the penetration depth with the impact speed and intruder size, for which a variety of sometimes contradictory results exist, see e.g., [31, 42] and discussions therein. The dependence of the granular force on the intruder speed is not always clear [31], and the role of various effects which determine the depth-dependent part of the force is also a subject of discussion, with models that suggest either frictional [83] or hydrostatic-like [72] forces. The picture which has evolved as a result of recent work is that there are multiple regimes where different aspects of the interaction between an intruder and granular particles may be relevant, and it has become obvious that it is necessary to look into the granular system itself in order to understand the basic physical mechanisms responsible for determining large scale dynamics of an intruder.

In this work, we take a different approach by correlating the results for the dynamics of an intruder with the evolution of the microstructure of the granular material itself. In particular, we concentrate on the influence of frictional properties of the granular particles, and on their packing. In particular, we show that these quantities may strongly influence the response of the granular material, the interaction

between the granular particles and intruder, and, consequently, the dynamics of the intruder.

The structure of this chapter is as follows. The simulation techniques and system setup are discussed in Appendix E and Section 4.3. In Section 4.4, we present results for the intruder dynamics for various parameters characterizing the intruder, and the granular system. We compare our results with existing simulations and experiments, with a significant part of this comparison in the Section 4.6. In the present work, we limit ourselves to the regime where total penetration depth is no larger than the intruder size. In Section 4.5, we then consider the granular material itself. In Section 4.5.1, we explore properties of the force field, the influence of packing and friction on force propagation, and topological quantities describing structure of the force field. In Section 4.5.2, we discuss affine and non-affine components of the dynamics of the granular particles. We conclude by discussing the question of energy expenditure, and we further elaborate on the role of friction and packing.

4.3 System Setup

Figure 4.1 shows the system setup. Here, H and W are the height and width of the granular bed, respectively. Periodic boundary conditions are implemented on the left and right boundaries. From below and above, the domain is bounded by rigid horizontal walls made up from monodisperse particles, with particle properties the same as in Chapter 3. The role of the top wall is essentially to contain those few particles which would be ejected during particularly violent impacts. However, the upper boundary is positioned sufficiently high that collisions with this wall are very rare.

We consider both circular and elliptical intruders. An elliptical form is one way to represent an ogive shape. The initial height of the intruder is fixed so that the lowest part of the intruder is 5 average particle diameters above the granular

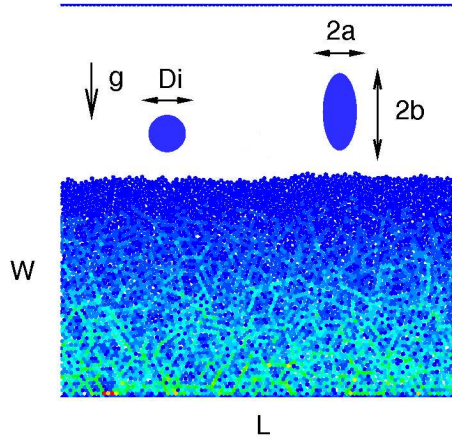


Figure 4.1 System setup. For illustration we show implementations of both circular and elliptic intruders. In the simulations, one of these shapes is incident on the middle of the upper surface of the granular system.

surface; we then vary the initial intruder velocity. The implementation of a circular intruder is straightforward. It is still considered to be a single large particle, with its own set of parameters, e.g., stiffness, and friction. We model elliptical/ogive intruders as a cluster of 360 granular particles with a mass appropriate to the intruder. This cluster forms a rigid shell on the surface of an ellipse; i.e., the particles in the cluster are rigidly attached to each other. In the simulations, the total force on the cluster is computed, and then the positions of all cluster particles are updated by applying Equations. (E.1) and (E.2) to the cluster as a whole. We have confirmed that implementing a circular intruder as either a single particle or as a cluster does not influence the results, as discussed below. Although we position the cluster particles on the surface only, we typically consider solid intruders, by choosing the cluster moment of inertia appropriately. More precisely, for solid intruders, the moment of inertia is given by $I = M(a^2 + b^2)/4$, where a and b are the semi-axes of an ogive intruder, and M is its mass.

The speed of sound, c , in the system will be needed below in order to put the results in perspective. We estimate this property by the time needed for information

to propagate across the domain. Specifically, we apply a point force at the top of the granular bed and measure the time needed for the force information to reach the bottom. When using the kinetic friction model, we find (in dimensionless units) $c \approx 2$, while for the static friction model, we find slightly larger $c \approx 2.4$. In our simulations, we concentrate on the subsonic regime, and consider intruder speeds up to 1.

In order to examine the effect of the granular microstructure on the impact, we model two types of packings. One is an exact hexagonal lattice with particles of identical size, and the other is a randomly packed system with $r = 0.0, 0.1, 0.2, 0.3$ and 0.4 . The hexagonal lattice is prepared by simply positioning the particles so that they initially touch each other. The random systems are prepared by positioning the particles on a square lattice, giving them random initial velocities, letting them settle under gravity, and then smoothing the irregular top surface roughness, if there is any. To consider reproducibility and the influence of a particular configuration on the results, we modify the initial random velocities assigned to the particles, and repeat the simulation.

Typically, no additional compaction of the bed is used; we have experimented with shaking of the bed to increase the volume fraction, but have not found any influence of this (minor) additional compaction on the results that follow. If not otherwise specified, we use 6000 particles, with the initial width of the domain, in units of the mean particle diameter, given by $W = 100$, and the initial height of the granular bed, given by $H = 60$, see Figure 4.1. After settling, the particles form a system of height ~ 56 for random polydisperse systems. This system size is at least moderately large. However, to test for system size independence, we have also carried out simulations in much larger domains containing up to 90,000 particles.

4.4 Results for the Penetration Depth

In this section, we discuss results for the penetration depth, and its dependence on parameters characterizing the granular system and of the intruder. We also briefly compare our results to the existing data, and we present more detailed comparisons in Section 4.6. In Section 4.5, we discuss the properties of the force field in the system, its dynamics, and their influence on the penetration depth, defined as the distance between the position of the bottom part of the intruder and the initial upper boundary of the granular bed at the point of impact.

We start by considering a randomly packed system with particles characterized by polydispersity $r = 0.2$, Coulomb friction $\mu = 0.5$, coefficient of restitution $e_n = 0.5$, and with kinetic friction only, $k_t = 0.0$. The intruder is a disk, with diameter of $D_i = 10$ in units of the average particle diameter, and otherwise possessing the same material properties as the granular particles. Figure 4.2 shows the time evolution of the penetration depths of an intruder impacting the granular bed with one of seven different speeds, ranging from 0.05 to 1.

The main properties of the results presented in Figure 4.2 are as follows. As expected, slower intruders create shallow craters; specifically, the penetration depth is less than the intruder's own diameter. By contrast, intruders of higher speeds are entirely submerged in the granular bed. For the larger impact velocities, we find an overshoot in the penetration depth, i.e., the intruder rebounds towards the surface of granular layer somewhat, as also observed experimentally [31]. The 'stopping time' at which the intruder essentially stops is somewhat ambiguous for smaller impact velocities, for which there is no overshoot, and this time might be considered to be either approximately constant, as in [12], or a decreasing function of the impact velocity, as in [42].

The origin of the small oscillations seen in plots of the intruder depth versus time for longer times in Figure 4.2 will be discussed later. Here, we proceed to analyze

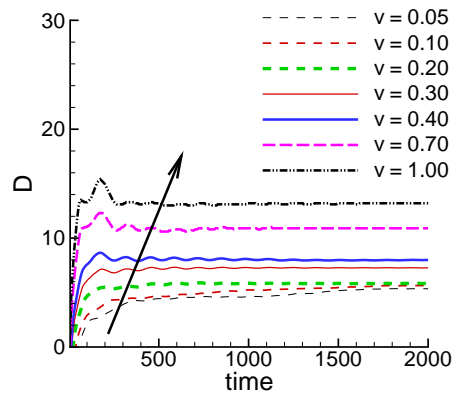


Figure 4.2 Penetration depth of $D_i = 10$ intruder impacting with different speed. Here we use $r = 0.2$, $k_n = 4 \cdot 10^3$, $k_t = 0.0$, $e_n = 0.5$, $\mu = 0.5$. Material properties of the intruder are the same as of the granular particles. The arrow shows the direction of increasing impact speed.

the influence of the properties of the intruder and of the granular system itself on the penetration depth.

4.4.1 Intruder Properties

Effect of Size: Figure. 4.3 shows the penetration of different size intruders in identical granular systems. For larger intruders of the same initial speed, we see deeper penetration. The results presented here agree well with the experimental and numerical results on penetration depths presented in [12], where similar granular materials, sizes of intruders, and system setup were considered.

Effect of Shape: Realistic intruders are often not circular, and therefore it is relevant to explore the influence of the intruder shape on the interaction with granular matter. This issue was considered experimentally [61], and it was found that as expected, more pointed objects penetrated deeper, although only in the case of shallow penetration.

To be specific, we consider here a particular shape, an elliptic ogive, and examine how the aspect ratio affects the penetration depth. As explained in Section 4.3, we

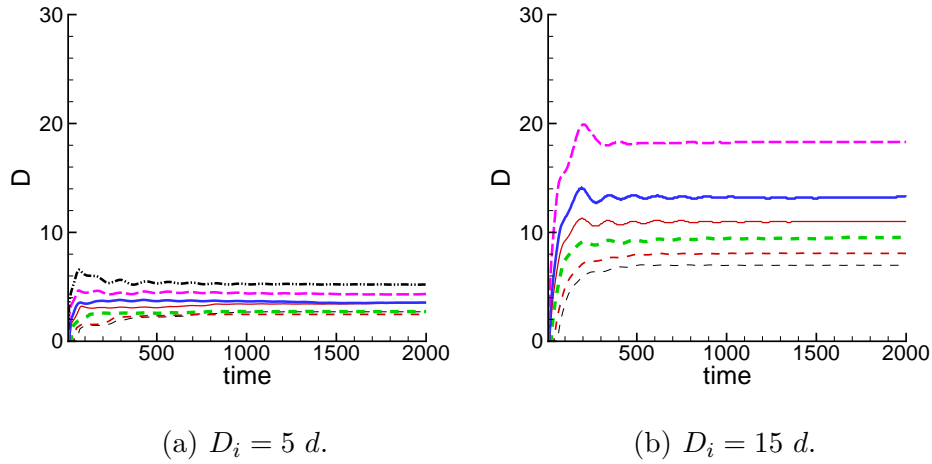


Figure 4.3 Penetration depths of intruders of different sizes. The other parameters and line patterns are the same as in Figure 4.2.

simulate elliptic intruders by preparing a ‘composite’ intruder made up from rigidly attached particles. To isolate the effect of the intruder’s shape, we fix the intruder masses to that of a disk with $D_i = 2a$ by changing the intruders’ density. Figure 4.4 show the penetration depth of the intruders characterized by different a ’s, b ’s, and impact velocities. We find that for the intruder sizes and aspect ratios considered here, the penetration depth increases approximately linearly with the aspect ratio, b .

Effect of Composition and Stiffness: The equations of motion determining the intruder’s dynamics are also influenced by the moment of inertia. To consider the influence of this quantity, we consider hollow intruders, consisting of only a shell of thickness d . In order to ensure that the ‘composite’ intruders behave identically to a single-particle, we model solid intruders using both approaches. All three configurations (single-particle solid, composite solid, and composite hollow) yield essentially identical results, showing that (i) modeling of an intruder either as a composite or as a single particle produces indistinguishable results, and (ii) the influence of moment of inertia of an intruder, at least with the present choice of

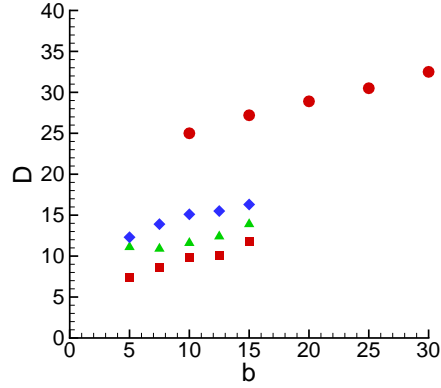


Figure 4.4 Penetration depth for intruders characterized by different elliptical ogives; we show the results for (i) $a = 5$ and $v = 0.1$ (red squares), $v = 0.4$ (green triangles), $v = 0.7$ (blue diamonds), and for (ii) $a = 10$, $v = 0.7$ (red circles). The domain size was increased in (ii) to $H = 100$, $W = 100$. The other parameters are as in Figure 4.2.

parameters, is minimal. We have also considered briefly the influence of the intruder’s stiffness on penetration, and simulated infinitely stiff intruders (limit of infinite spring constant k_n in our force model) interacting with soft granular particles. We find that the penetration depth for these stiff intruders is only slightly smaller compared to the finite- k_n ones. This result suggests that direct interaction of an intruder with granular particles plays only a minor role in determining final presentation depth, while particle-particle interactions are much more important. This interaction is discussed next.

4.4.2 System Properties

Effect of Particle Stiffness and the Coefficient of Restitution: Particle stiffness, modeled by the spring constant, k_n , modifies the collisional time scale in the problem, $t_{col} \propto 1/\sqrt{k_n}$. Conceivably, one might expect that as k_n varies at constant (nondimensional) impact speed, the results would not change. That is, dynamics expressed in units of t_{col} might be independent of dimensional properties such as k_n . However, this invariance is broken by the presence of gravity. While

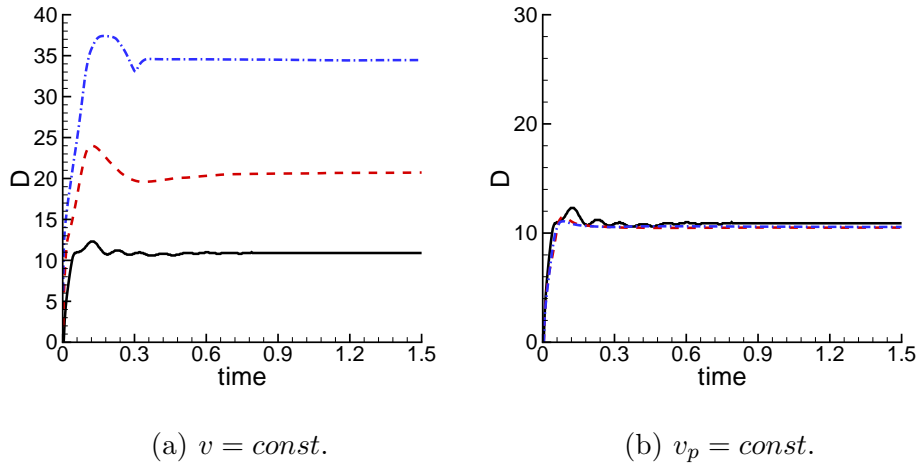


Figure 4.5 Penetration depth of an intruder in systems with varying stiffness: $k_n = 4 \times 10^3$ (black solid); $k_n = 4 \times 10^4$ (red dashed); $k_n = 4 \times 10^5$ (blue dash-dot). In the part a), the impact speed is $v = 0.7$; in part b), the impact speed in physical units (m/s, for example) is kept fixed at the value $v_p = 0.7d/t_{col}$ ($k_n = 4.0 \cdot 10^3$). The other parameters are as in Figure 4.2.

the role of gravity is explicitly considered later, we can already see its influence on the dynamics in the results of Figure 4.5 a). This figure shows that as k_n increases at fixed dimensionless impact speed, the impact depth becomes significantly larger. This result can be understood by realizing that: (i) the influence of gravitational compaction is much weaker for stiffer particles; and (ii) the energy of impact is much larger in the case of larger k_n , since impact velocity (in physical units) scales as $\sqrt{k_n}$. Note that larger stiffness is one of the reasons for significantly larger penetration depths in recent simulations [72], where stiffer particles were considered. To conclude this discussion, Figure 4.5 b) shows that, as expected, the penetration depth decreases if an impactor of fixed speed in physical units interacts with a granular system made of stiffer particles.

Figure 4.6 shows the influence of elasticity of the granular particles, measured by the coefficient of restitution, e_n . A large coefficient of restitution leads to a significantly deeper penetration, as it would be expected, since the energy loss is

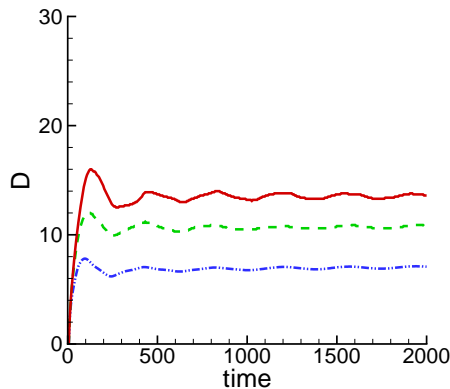


Figure 4.6 Penetration depth of an intruder in systems with varying coefficient of restitution, $e_n = 0.9, 0.5, 0.1$ shown by red (solid), dashed (green) and blue (dash-dot) lines, respectively. Here, $v = 0.7$, the system size is $W = 200, H = 200$; the other parameters are as in Figure 4.2.

reduced relative to a lower restitution coefficient. Interestingly, while a decrease of e_n reduces the depth of penetration, it does not remove the overshoot of the $D(t)$ curve. Also, we will see below that a different behavior results when the frictional properties of granular particles are modified. Later in this section, we will also discuss the influence of e_n on the long-time oscillations of the intruder depth, $h(t)$. Note that in the simulations reported in Figure 4.6, we find it necessary to increase the domain size to avoid its influence on the results.

Effect of Friction: The role of friction between the granular particles on the penetration depth in particular, and on the response of the granular material to an intruder in general is not immediately obvious. For example, in considering the response of a system to a point force, it has been found that friction plays a role in determining how forces and stresses propagate through the system [29]. Of course, a response to an intruder is expected to be more complicated since it leads to a large scale rearrangement of granular particles, which is not expected in a response to a localized (small) point force. Indeed, it has been suggested that friction is not necessary crucial in understanding this response [72]. Here, we illustrate the influence

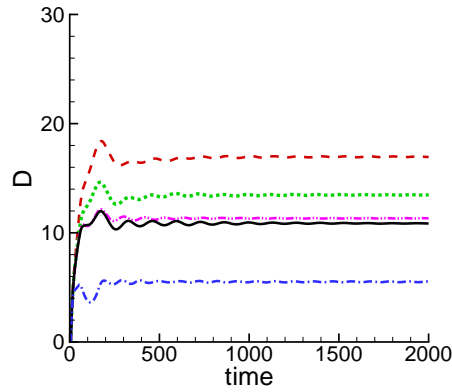


Figure 4.7 Penetration depth for different friction models and Coulomb thresholds; here we show the results as follows (top to bottom): $\mu = 0$ (red dashed); $\mu = 0.1$, $k_t = 0.0$ (green dotted); $\mu = 0.1$, $k_t = 0.8k_n$ (pink dash-dot-dot), $\mu = 0.5$, $k_t = 0.0$ (black solid); $\mu = 0.5$, $k_t = 0.8k_n$ (blue dash-dot). Here $v = 0.7$, the other parameters are as in Figure 4.2.

of friction on the penetration depth for a particular system. We discuss more generally the manner in which friction influences the dynamics of an intruder in Section 4.6, and the corresponding behavior of the granular material of different frictional properties in Section 4.5.

To illustrate the influence of friction, we consider two effects: first, the effect of the friction model, and second of Coulomb threshold. Figure 4.7 shows the corresponding results. We find that having a model with static friction leads to a significantly smaller penetration depth (blue dash-dotted curve in Figure 4.7) than a model without static friction, particularly for a large Coulomb threshold. For a smaller Coulomb threshold, the influence of static friction is weaker, and the response of the system in that case turns out to be similar to the one obtained using kinetic friction only (compare green dotted and pink dash-dot-dot curves in Figure 4.7). Furthermore, an ‘overshoot’ in the intruder depth may be removed in the case of (strong) static friction.

Effect of Packing and Polydispersity: One of the focal points of this work is the influence of granular microstructure on impact. Microstructure is strongly influenced by the packing and polydispersity of granular particles. To analyze the influence of these parameters, we have carried out simulations where we have varied the parameter r determining polydispersity between 0.0 and 0.4. We have also carried out simulations using a perfect hexagonal lattice of particles as the initial configuration. We typically find that the results for a system with $r = 0.0$, prepared as described in Section 4.3, are similar to results obtained using a hexagonal lattice. This is not surprising, since monodisperse particles tend to crystallize, as confirmed by the pair correlation function, which shows only small differences between monodisperse ‘random’ and hexagonal lattices. (These results are not shown here for brevity.) Here, we show the results obtained using a hexagonal lattice in place of an $r = 0.0$ system prepared using our usual protocol.

Figure 4.8 shows the intruder depth as a function of time for an impact on a hexagonal lattice. We immediately note very different properties of the $D(t)$ curves compared to an impact on a polydisperse system, viz. Figure 4.2. For the impact velocities considered here, the intruder very quickly reaches a depth at which its velocity reverses, and then the intruder actually rebounds *outside* of the granular layer, falls again under gravity, and then settles at the final depth. This final depth does not depend in any obvious manner on the impact velocity, which essentially influences only the initial depth which the intruder reaches (before rebound), and the length of the interval after impact which the intruder spends outside of the granular layer (this interval being longer for larger impact velocities). Finally, by comparing the penetration depth between an impact on a hexagonal lattice, shown in Figure 4.8, and on a disordered granular system, such as the one shown in Figure 4.2, we note that the penetration depth in the former case is much smaller. We will discuss the reasons for this difference later in Section 4.5.

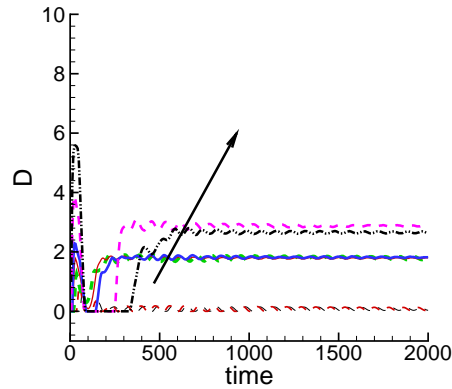


Figure 4.8 Penetration depth for an impact on a hexagonal lattice; here $r = 0.0$ and the other parameters and line patterns are as in Figure 4.2. Note the different range on the vertical axis compared to the one typically used.

Figure 4.9 shows in more detail how the final penetration depth depends on the polydispersity. To help interpretation of the results we show both the final depth as a function of r for fixed v 's (part a)) and the final depth as a function of v for fixed r 's, part b). Clearly, the penetration is deeper in polydisperse systems compared to the hexagonal one, for all considered impact velocities. However, we find that the degree of polydispersity has no significant effect on the penetration depth as long as the system is not monodisperse and ordered.

Figure 4.9 b) shows that the penetration depth depends approximately linearly on the impact speed of the intruder for larger velocities and deeper penetration. This observation agrees with results reported earlier [12, 18, 31], where it was found that the penetration depth increases linearly with the impact speed for a range of impact depths that are comparable or larger than the intruder size. For smaller impact velocities, we find deviations from the linear scaling, again consistently with the literature [1, 2, 84]. We discuss this scaling in some more detail in Section 4.6.

Effect of Gravity: We discuss here in more detail the influence of the acceleration of gravity on the penetration depth. As mentioned earlier, the value of the gravitational

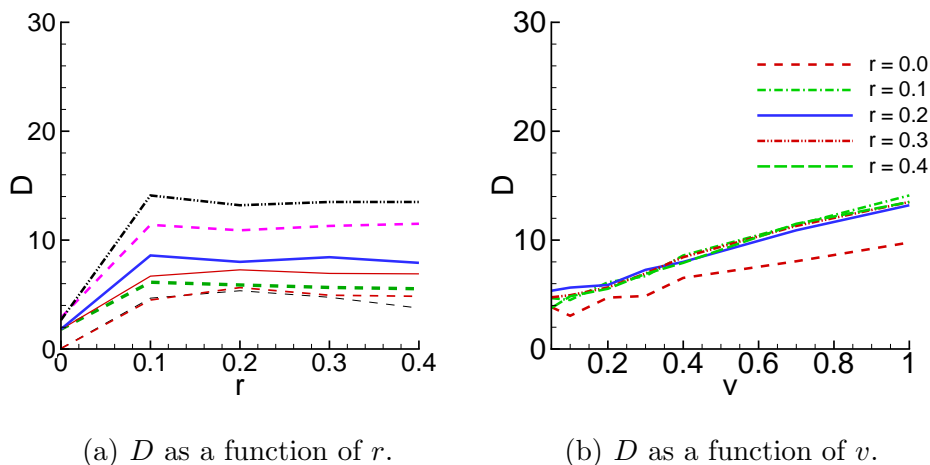


Figure 4.9 Final (long time) penetration depth for the systems characterized by different polydispersities, r ; the other parameters are as in Figure 4.2.

acceleration is expected to play a role, since it influences the mobility of the particles following impact. For brevity, we consider the effect of gravity only for the ‘basic’ system characterized by $r = 0.2$, $k_t = 0.0$. Here, as the initial configuration we consider a system prepared under Earth’s gravity and then left to relax until any dynamics ceases, prior to impact under appropriate g . Figure 4.10 compares the results for Earth’s gravity with data for several other planets/satellites, specifically, Pluto, Moon, Mars, Jupiter. We find significantly deeper penetration for smaller gravitational accelerations, see Figure 4.10. Furthermore, the maximum penetration is reached at much later times, as expected from the discussion in [31, 72] and in Section 4.6. Figure 4.11 shows significantly increased mobility of the particles after impact, confirming the intuitive argument presented above. Note that we modify only gravitational force on the particles, and not their stiffness, which remains the same. We also note that change of impact speed due to modified gravity is minor, only a fraction of a percent.

Effect of System size and reproducibility: System size has been recognized in previous work as one of the factors which may influence the results [9, 41, 42,

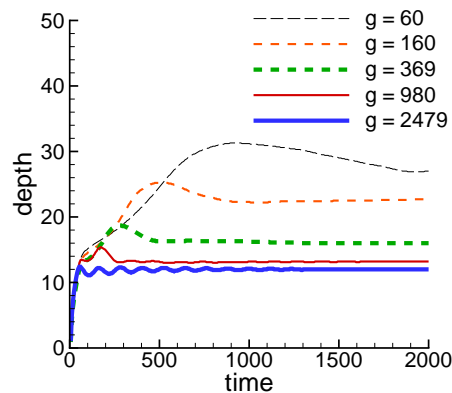


Figure 4.10 Influence of gravitational acceleration on impact; here, $v = 1.0$ and the other parameters are as in Figure 4.2. We chose g 's (given in cm/s^2), appropriate to various objects in the Solar system: Pluto, Moon, Mars, Earth, Jupiter.

71, 72, 79]. To explore this effect, we have carried out additional simulations where the system size was varied. Since changing the system size also requires changing the configurations of the particles, which, we affect reproducibility, we also consider that issue here, that is, we consider the variations between realizations for the same macroscopic parameters. It is to be expected that changing the initial particle configuration will lead to different dynamics, and the different realizations give us a measure of statistical fluctuations on macroscopic properties such as the penetration depth.

Figure 4.12 shows results for six different system sizes, corresponding to different depths, H , and widths, W . First we note that despite different visual appearance of the the detailed trajectories, the final penetration depth (the value reached for long times) varies only very little (less than a particle diameter) between systems of different sizes. This variation is smaller than that due to different initial conditions, and therefore we conclude that for the systems considered here, the system size is sufficiently large that there is no significant influence on the total penetration depth. This observation agrees with the experiment results found in [71] and [56]. We note

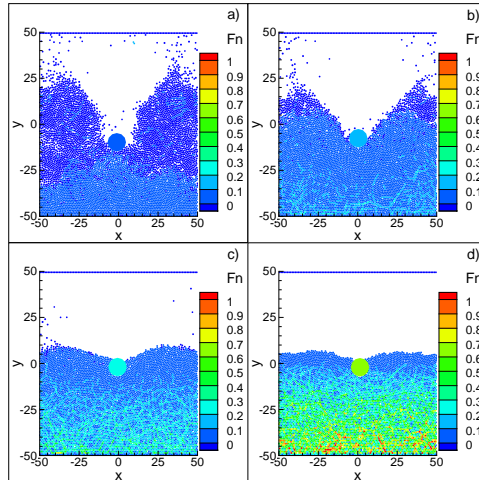


Figure 4.11 Snapshots of a granular system after impact under the four larger gravities considered here ($g = 160, 369, 980,$ and 2479 cm/s^2) from Figure 4.10 at $t \approx 300$. Gravity is monotonously increasing from a) to d).

in passing that the presence of overshoot in $D(t)$ is not influenced by the system size, as also found in a recent experimental work [31].

Next, we comment on the oscillations of the penetration depth that are clearly visible in Figure 4.12. Perhaps contrary to an intuitive expectation, these oscillations *do not* decrease for the largest systems considered here; on the contrary, they increase in amplitude. Below, we first discuss the origin of these oscillations, and then their dependence on the system size.

Recall that the penetration depth is defined with respect to the initial ($t = 0$) top surface of the granular system. During an impact, the kinetic energy of the intruder is mostly transferred into elastic energy that propagates through the system in the form of (damped) elastic waves [9]. (Note that some of the energy goes into friction; this issue is discussed briefly in the Conclusions.) These elastic waves interact with the system boundaries, and in the case of the bottom boundary they partially reflect and lead to an expansion of the whole granular bed. We have confirmed this by comparing the period of oscillations visible in the Figure 4.12 with the time it takes for the elastic waves to cross the system twice. For example, note that for shallower systems, the

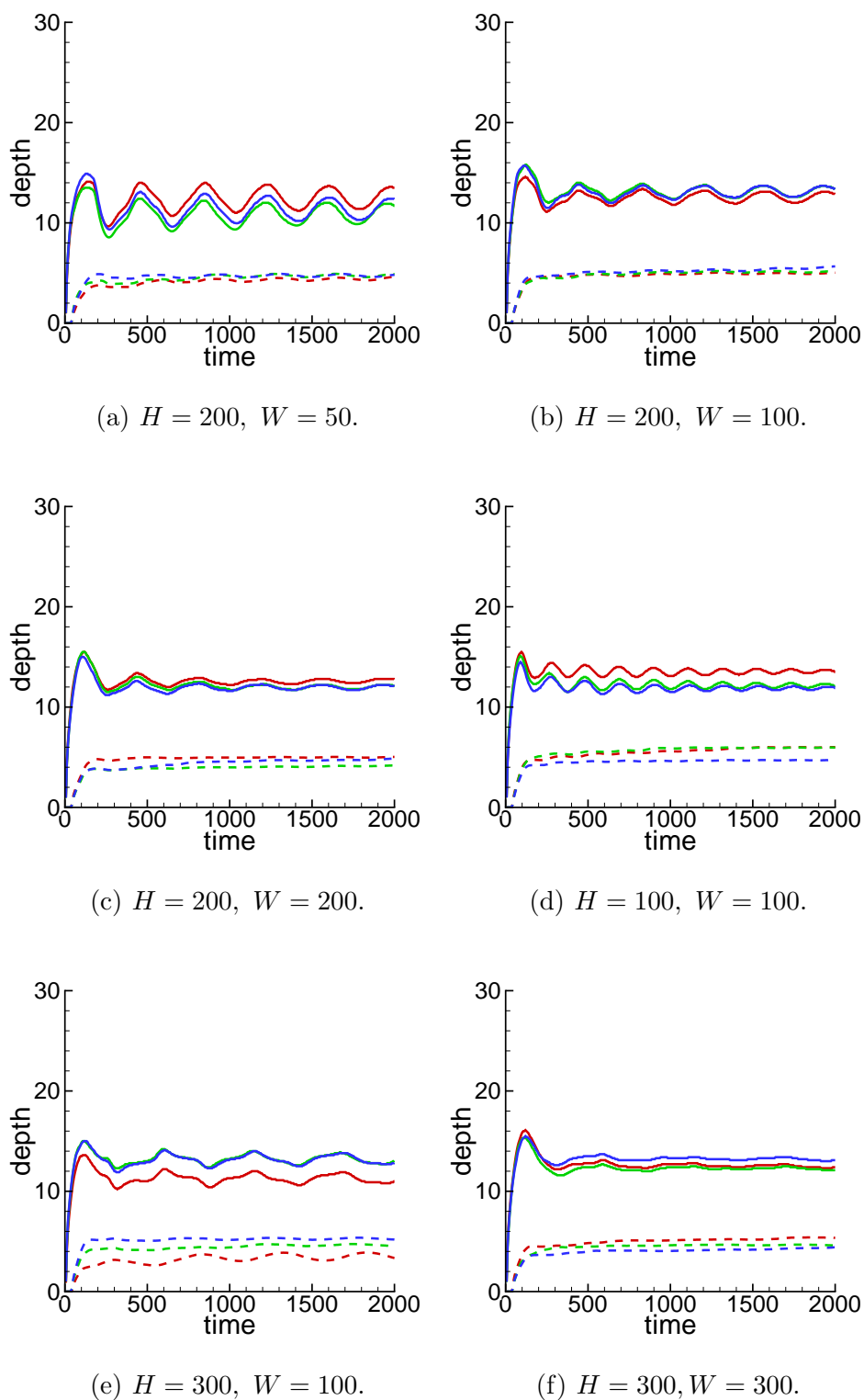


Figure 4.12 Influence of the system width, W , and height, H , on the penetration depth as a function of time. The solid/dashed lines show three realizations of impacts with the speed $v = 1.0/0.1$, respectively. The other parameters are as in Figure 4.2.

period of the oscillations is shorter, as expected based on the above argument. It is important to note that for the present choice of parameters these elastic waves do not influence in any significant manner the motion of the intruder *relative* to the granular particles surrounding it: they essentially lead to global oscillations of the system. To confirm this statement, Figure 4.13 shows the depth of the intruder with respect to the *time – dependent* position of the interface, calculated at the same time as the intruder’s position. The long-time oscillation are not visible anymore. A different regime, with intruders comparable in size to the granular particles, and therefore more susceptible to the pressure due to the propagating elastic waves, has been discussed recently [9].

The next question is the influence of the system width, W , on the oscillations. Again, for the widths considered, there is no influence on the final penetration depth. More narrow systems, however, lead to increased amplitude of the oscillations. This is a consequence of our periodic boundary conditions imposed at the right and left boundaries: the waves propagating right/left from the impact point ‘re-appear’ from the other side of the domain and increase the oscillatory behavior. In the case of large systems, these waves lead to non-sinusoidal oscillations, as can be seen in Figure 4.12 f).

The final question is why don’t the oscillations diminish with the system height, H , for the system sizes considered here. The answer to this question has to do with the properties of the elastic waves propagating through the system. It is known that propagation is enhanced in the systems characterized by stronger compression, or, correspondingly to some degree, larger volume fractions, as discussed recently [44]. In larger systems, there is stronger gravitational compaction in the deeper layers, leading to stronger wave propagation and rebound, and correspondingly, to more visible oscillations. This conjecture is supported by the results for different gravity (Figure 4.10) where we observe that in the systems under smaller gravity, the oscillations

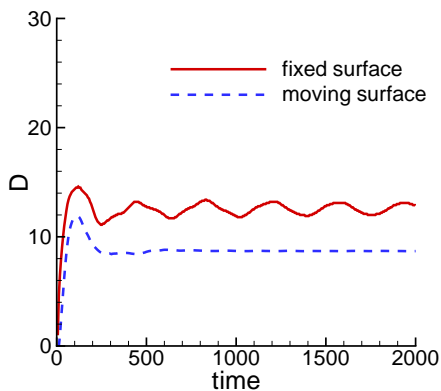


Figure 4.13 Penetration depth for a system characterized by $W = 100$ and $H = 200$; the impact speed is $v = 0.7$; the other parameters are as in Figure 4.2.

are weaker as well. We note that for significantly larger systems compared to the ones considered here, one expects that damping and/or friction would be strong enough to reduce or eliminate the influence of elastic waves. Consistently, for the systems considered here, Figure 4.6 shows that stronger damping significantly dampens the oscillations.

4.5 Microstructure Evolution, Force Networks, and Granular Dynamics during Impact

In this section, we discuss the internal response of the granular system to impact, and the role which microstructure plays in determining the macroscopic results, such as penetration depth. We concentrate in particular on the role which polydispersity, ordering, and friction play in determining the granular response. We consider two separate sets of measures to quantify the response: (i) the geometric and topological properties of the force field evolving in a granular system during impact, and (ii) the dynamics of the granular particles quantified by measuring affine (conforming) and non-affine (non-conforming) components of granular motion.

4.5.1 Properties of the Force Field

Figures 4.14 - 4.17 show snapshot of the normal and tangential forces which granular particles experience due to impact on a polydisperse system at four different times. Before the impact itself (part a), we see the force chains due to gravitational compaction, already discussed earlier. During the impact, we observe approximate isotropic expansion of the area in which particles experience large normal force. Properties of this large-force area are discussed next.

One issue of interest is the influence of inter-granular friction on the properties of the force field. By comparing Figures 4.14 and 4.16, we find no significant differences, suggesting that the friction model is not crucial in determining the properties of the normal force field between the granular particles. On the other hand, Figures 4.15 and 4.17 suggest that tangential forces depend much stronger on the friction model. Recalling now that the penetration depth is much smaller for the particles modeled by static friction and large Coulomb threshold, viz. Figure 4.7, we conclude that at least for the systems considered, tangential forces are the ones which play a significant role in determining the dynamics and final penetration depth of an intruder. The influence of friction on force network is even more obvious in the impact on hexagonally ordered system, which we discuss next.

Figures 4.19 to 4.22 show the structure of the normal and tangential force field during impact on an ordered, hexagonal system. We find that the forces propagate in very a different way, compared to what we find for an impact on a random, polydisperse system: in the case of the ordered packing, we see predominant propagation in the lattice directions, combined with a (weaker) uniform, isotropic front. Therefore, we conclude that geometric microstructure plays a significant role in determining the force field in a granular system. We note that any degree of polydispersity and related disorder leads to a transition from ray-like propagation, shown in Figures 4.19 and 4.21, to isotropic propagation, seen in Figures 4.14 and 4.16. We have confirmed

this by carrying out corresponding simulations with smaller r 's (not shown here for brevity). Since we observe larger magnitudes of the forces in the ordered system, we expect that these larger forces manifest themselves as larger forces on the intruder itself, and therefore lead to more shallow penetration.

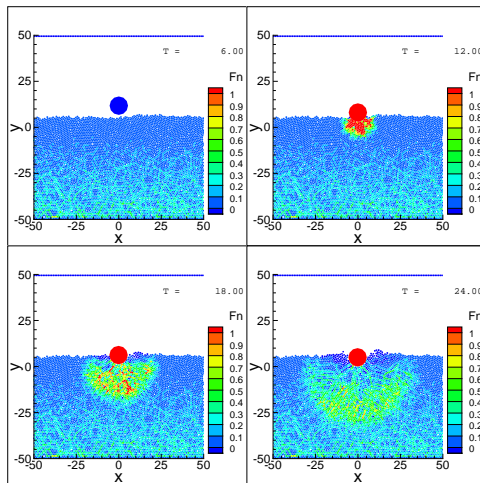


Figure 4.14 Normal force experienced by the granular particles at four different times. Here, $v = 0.7$, and the other parameters are as in Figure 4.2 (kinetic friction).

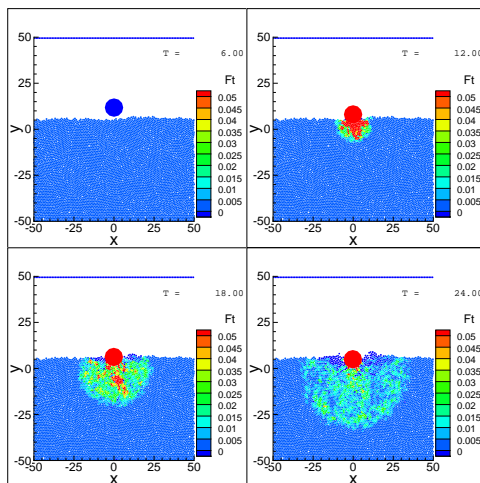


Figure 4.15 Tangential force experienced by the granular particles at four different times for the same parameters as in Figure 4.14 (kinetic friction).

Next we discuss the influence of friction on force propagation in an ordered system. Regarding normal forces, by comparing Figures 4.19 and Figure 4.21, we

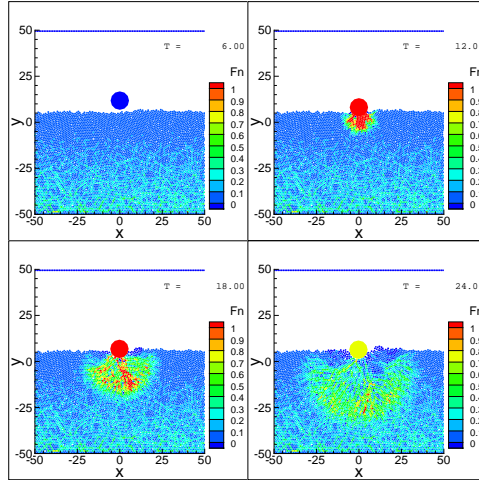


Figure 4.16 Normal force experienced by the granular particles at four different times for $k_t = 0.8k_n$; the other parameters are as in Figure 4.14 (static friction).

again see no significant differences on the temporal and spatial scales considered. However, one can still observe the effect of friction on some features of force propagation, which have been discussed recently from the point of view of elastic versus hyperbolic force propagation [29, 30]. Static friction is expected to lead to a more elastic-like response, that is, the force (or pressure) on granular particles is expected to reach a maximum value directly below the source, while kinetic or no friction, is expected to lead to a more a hyperbolic-like response, with a pressure dip below the source. By comparing the results in Figures 4.19 and 4.21 at $t = 24$, one can observe a variation of this effect, with the significantly more pronounced force dip below the source for kinetic or no friction. Figure 4.18 shows this effect precisely: here we show the normal forces on the granular particles at $t = 24$ at fixed depth below the surface, for systems characterized by different friction models, and by different Coulomb thresholds. We note that having an ordered structure is important to observe this effect; polydispersity and associated disorder have masked it in Figures 4.14 and 4.16, which show the normal force for a polydisperse system.

As for the disordered system discussed above, the influence of friction is much more significant for tangential forces than for normal forces. Figures 4.20 and 4.22

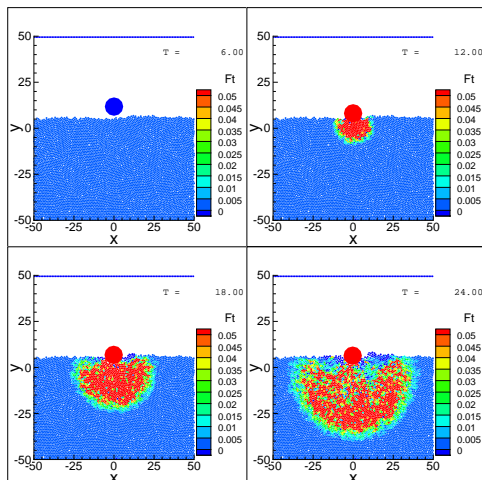


Figure 4.17 Tangential force experienced by the granular particles at four different times for the same parameters as in Figure 4.16 (static friction).

illustrate this effect. In addition to observing significantly larger tangential forces when static friction is included, we again find more hyperbolic-like force propagation in the case of kinetic friction, and a more uniform, elastic-like response when static friction is present.

Figure 4.23 shows F_y , the total force on the intruder in the y direction, for different friction models and polydispersities/ordering. We see that this force is very large immediately after impact, and then decreases significantly on a very short time scale. The second, much smaller peak in the force visible in some of the results is due to reflected elastic waves as discussed before. The influence of these waves on the intruder dynamics is minor. While we note larger force for impact on polydisperse particles modeled by static friction model (blue dash-dot line in the part a)), perhaps the most important observation regarding the results shown in this figure is how similar they are for the different systems considered here, suggesting that it may be difficult to extract the main features about the intruder's dynamics based on this information alone: recall that the penetration depths differ significantly between the different friction models and different polydispersities.

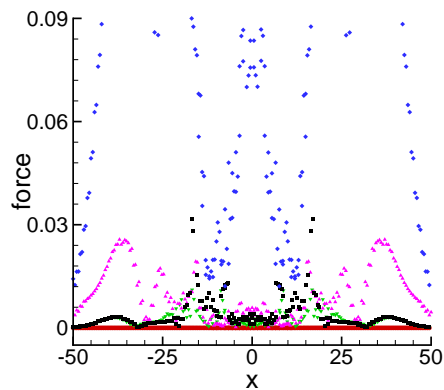


Figure 4.18 Normal force experienced by the granular particles at fixed distances below the surface due to an impact on a hexagonal lattice at time $t = 24$; $\mu = 0$ (red up-triangles); $\mu = 0.1$, $k_t = 0.0$ (green down-triangles); $\mu = 0.1$, $k_t = 0.8k_n$ (pink squares), $\mu = 0.5$, $k_t = 0.0$ (black diamonds); $\mu = 0.5$, $k_t = 0.8k_n$ (blue circles). Here $v = 0.7$, the other parameters are as in Figure 4.2.

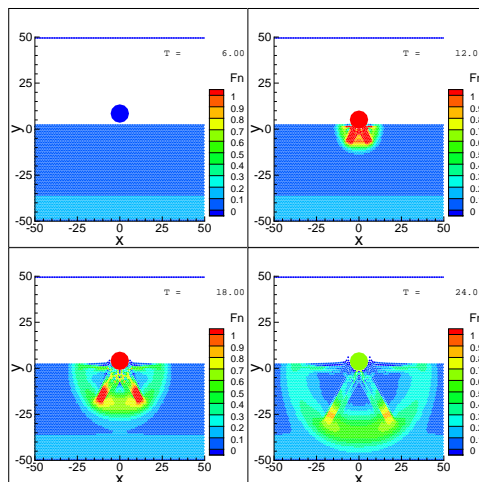


Figure 4.19 Normal force experienced by the granular particles at four different times during impact on a hexagonally ordered system. Here, $r = 0.0$, and the other parameters are as in Figure 4.14 (kinetic friction).

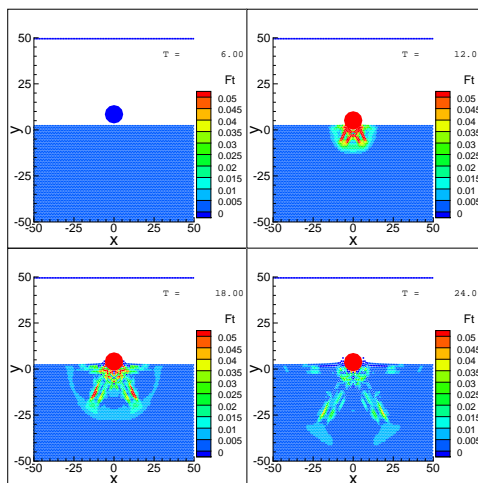


Figure 4.20 Tangential force experienced by the granular particles at four different times for the same system as in Figure 4.19 (kinetic friction).

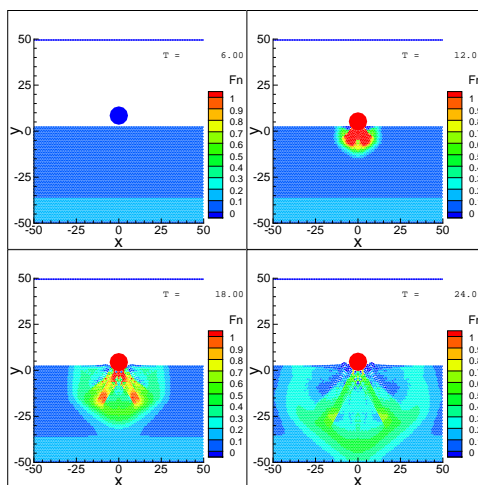


Figure 4.21 Normal force experienced by the granular particles at four different times for $k_t = 0.8k_n$; the other parameters are as in Figure 4.19 (static friction).

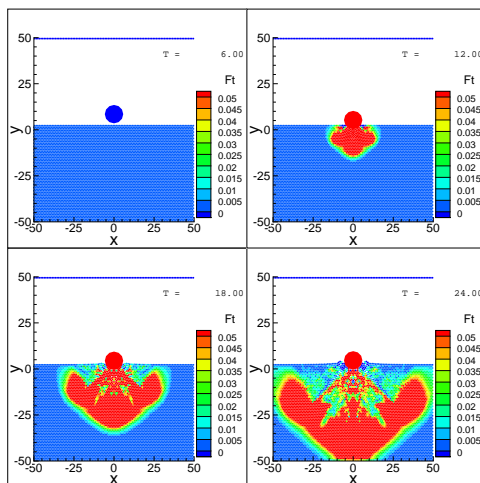


Figure 4.22 Tangential force experienced by the granular particles at four different times for the same system as in Figure 4.21 (static friction).

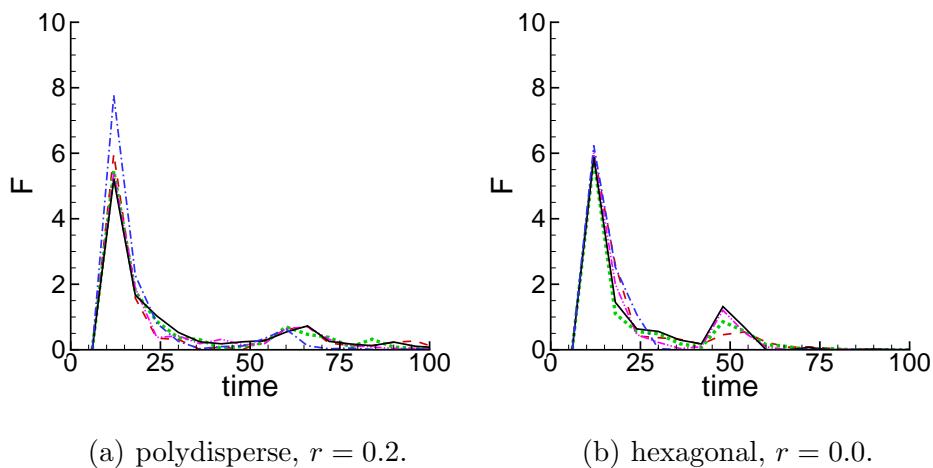


Figure 4.23 The total force on the intruder as a function of time for the following systems (depth versus time for the systems in part (a) is available in Figure 4.7): $\mu = 0$ (red dashed); $\mu = 0.1$, $k_t = 0.0$ (green dotted); $\mu = 0.1$, $k_t = 0.8k_n$ (pink dash-dot-dot), $\mu = 0.5$, $k_t = 0.0$ (solid black); $\mu = 0.5$, $k_t = 0.8k_n$ (blue dash-dot). Here $v = 0.7$; the other parameters are as in Figure 4.2.

Topological Properties of the Force Field The force fields, in particular in disordered systems, may have very complicated structures. Therefore, it is difficult to extract their generic properties, and to reach, for example, an answer to the question of global changes of the force field due to impact. For this reason, we consider topological properties of the force network, by computing its connectivity. One measure of the connectivity can be formulated in terms of Betti numbers, which are global topological measures specifying the properties of a network. In particular, the zeroth Betti number, B_0 , measures the number of connected components, and the first Betti number, B_1 , measures the number of holes inside a network. Clearly, these quantities depend on the force threshold chosen. For example, if one chooses zero threshold (considering all the particles), B_0 , will provide an information about the fabric of the material. As the force threshold is increased, the number of particles experiencing a force larger than a given threshold decreases, and consequently, the topology of the network changes. The computations are carried out using the publicly available software package [52] CHOMP. These computations involve thresholding a particular force level and producing a binary image (black less than or equal to the threshold and white above the threshold), and then computing Betti numbers, measuring connectivity of the resulting images. Here, we will concentrate only on B_0 , with the main goal of quantifying the differences between the force networks developing during impact for different friction models, and for different packings. We note that here we explore connectivity on the particle scale; an alternative approach where connectivity is considered on the level of individual contacts is possible as well [66]. Future work should address the differences, if any, resulting from these two different approaches to computing connectivity. For brevity, here we concentrate only on the force fields in polydisperse systems.

Figure 4.24 shows B_0 's for the impact on a polydisperse system with (a) kinetic and (b) static friction. The snapshots of the corresponding force field for the part

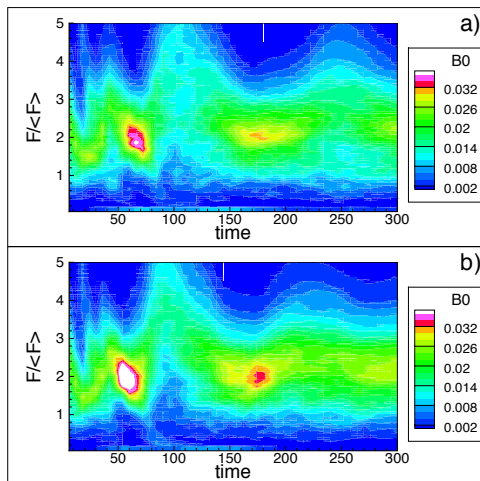


Figure 4.24 Zeroth Betti number, B_0 , for the normal force during impacts on polydisperse, $r = 0.2$, systems with $v = 0.7$ and (a) kinetic friction; (b) static friction; the other parameters are as in Figure 4.2. In this and the following figures, B_0 's are normalized by the number of particles, and the forces by the average (normal) force on all particles. Note that the peaks in the B_0 's for $F / \langle F \rangle \approx 2$ are due to the elastic waves propagating through the system.

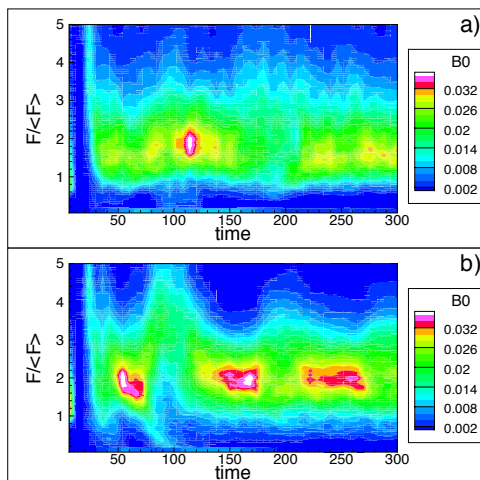


Figure 4.25 Zeroth Betti number, B_0 , for the tangential force during impacts on the systems as in Figure 4.24.

a) can be seen in Figure 4.14. We see that for very small and for very large forces, the B_0 's are very small, since for very small forces all particles are found to form a cluster (due to being in contact with each other), while the number of particles experiencing very large forces is small, so that there are no components/clusters to be seen. The main difference between the two parts of the figures is larger number of components/clusters for the system where static friction is included. Recalling more shallow penetration for the system where static friction is included, we conjecture that there is a correlation between larger number of components/clusters and corresponding resistance to an impact. To our knowledge, this influence of static friction on the structure of force network has not been discussed previously in the literature.

Figure 4.25 shows the tangential forces for the same system as in Figure 4.24. The information which can be obtained from this figure is consistent with the insight which we reached by considering the normal forces: larger number of components/clusters for the systems where static friction is present.

We conclude by summarizing our current results regarding properties of the force field during an impact. For disordered, polydisperse system, we find the following:

- The main influence of static friction on the force field is a significant increase of tangential forces;
- Both normal and tangential forces show increased ramification (in the sense of increased number of components/clusters) in the presence of static friction.

For monodisperse, ordered systems, we find:

- As for polydisperse systems, there is only a minor influence of friction on the normal forces, while tangential forces are increased strongly by static friction. In addition, the total force on an intruder is similar for monodisperse ordered and polydisperse disordered systems, suggesting that it may be difficult to extract

information about the intruder’s dynamics based on the information about the total force on the intruder alone.

- The normal force field is highly uniform; however, the tangential force field is much more structured, suggesting that a significant amount of disorder of the tangential interactions between the particle is introduced during an impact.

We note that the current results concentrate only on the global, large scale features. More work is needed to analyze the detailed, local, features of the force fields, including their temporal evolution.

4.5.2 Properties of the Displacement Field

Next, we consider the dynamics of the granular particles due to impact. It is of interest to consider both affine/conforming and non-affine/not conforming parts of the displacement field. For this purpose, we use the approach from [22], which is explained in Appendix D.

Figure 4.26 shows snapshots of the affine deformation for the polydisperse systems characterized by different friction models. We show the x and y components of the vector $\mathbf{A}_f = \mathbf{A} \cdot (\mathbf{r}(t) - \mathbf{r}(t - \delta t))$. These figures reveal outward motion of the granular particles away from the point of impact (parts a) and b)), downward motion in the area below the impact, combined with the upward motion at the surface of the granular bed just next to the impact point. While the results for the two systems are fairly similar, we see increased mobility for the particles experiencing kinetic friction only, in particular for the y -component of affine deformation.

Figure 4.27 shows \mathcal{D}_{min}^2 , measuring the strength of the non-affine component. This component of motion is more prominent for the case where only kinematic friction is present; however, the differences between the two cases are only moderate.

As for the earlier results showing forces on granular particles, precise information about affine and non-affine components of granular dynamics for hexagonally ordered

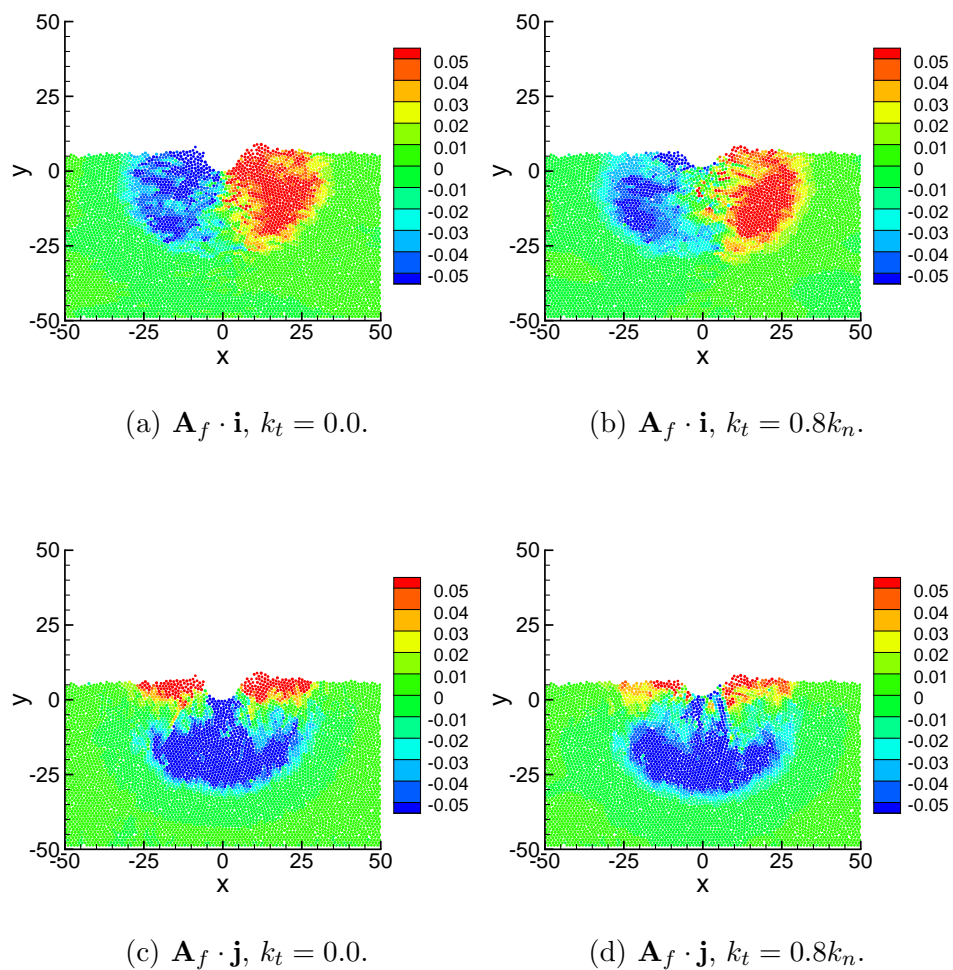


Figure 4.26 Affine deformation at $t = 24$ for impact on polydisperse systems modeled by different friction models; \mathbf{i} and \mathbf{j} are the unit vectors in the x and y directions; here $v = 0.7$, the other parameters are as in Figure 4.2.

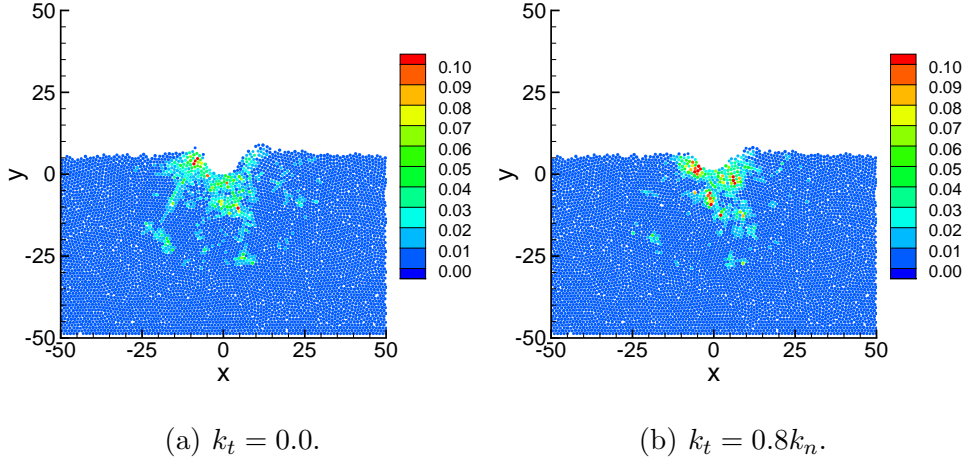


Figure 4.27 \mathcal{D}_{min}^2 distribution at $t = 24$ for impact on polydisperse systems modeled by different friction models; the parameters are as in Figure 4.26.

systems is also of interest. Figures 4.28 and 4.29 show corresponding results, again for the systems characterized by kinematic and static friction. for systems prepared in hexagonal arrays. Here, we also include the L_2 norm of the affine deformation since it provides useful additional insight. Figure 4.28 shows significantly stronger affine deformation for the kinetic friction case, particularly visible when considering the norms, parts e) and f) of the figure. Granular particles interacting only by kinetic friction clearly respond much stronger to an impact. Consistently, Figure 4.29 then shows that non-affine component is also much more pronounced for the kinetic friction case, suggesting that static friction reduces also non-affinity of particle motion.

4.6 Comparison to Effective Models and Experimental Results

A simple model for the force describing interactions between an intruder and granular material can be outlined as follows [83]. The total force on the intruder includes gravity, and the force due to interaction with the granular material. The force due to the interaction may be considered as a separable function of two variables, $(y(t), u(t))$, where $y(t)$ is the time dependent position of the intruder, and $u(t)$ is its

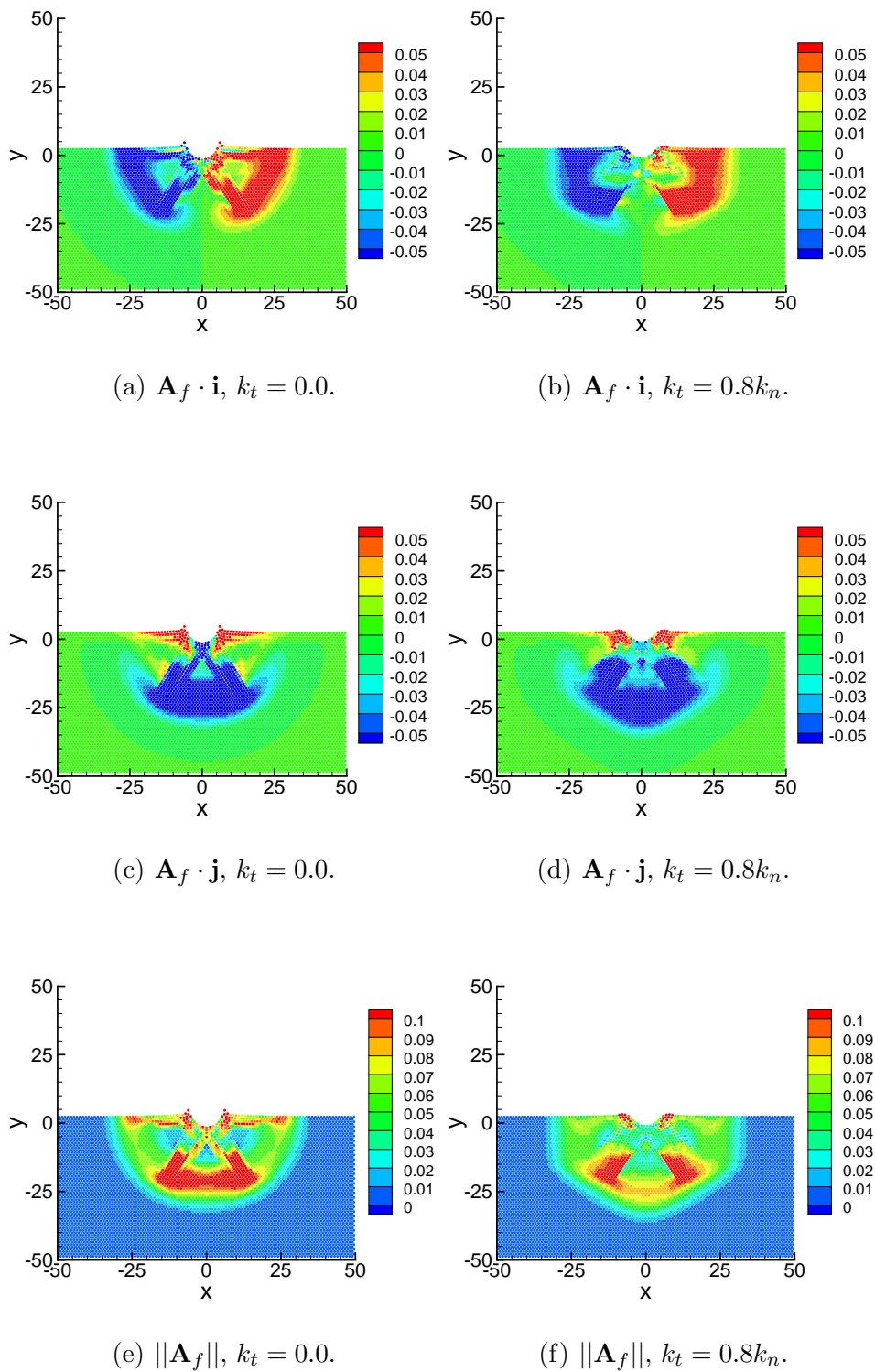


Figure 4.28 Affine deformation at $t = 24$ for impact on monodisperse hexagonal systems modeled by different friction models; here $v = 0.7$, the other parameters are as in Figure 4.2.

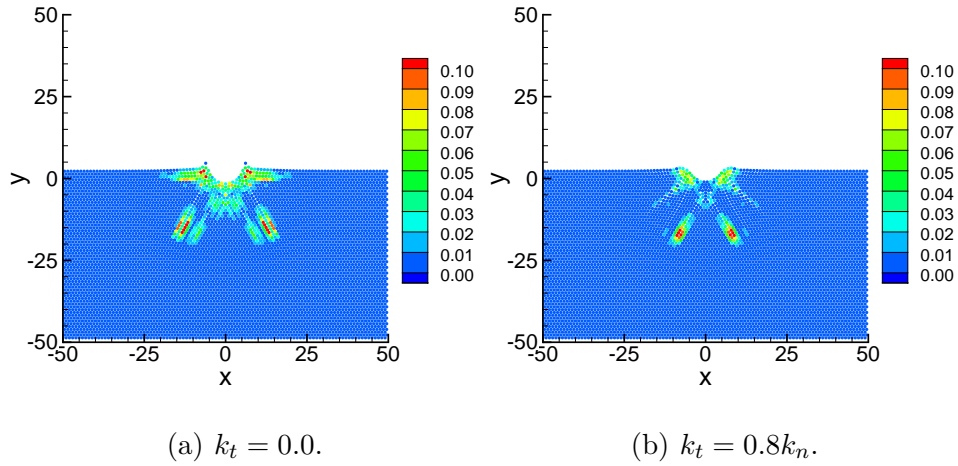


Figure 4.29 \mathcal{D}_{min}^2 distribution at $t = 24$ for impact on polydisperse systems modeled by different friction models; the parameters are as in Figure 4.28.

time-dependent velocity

$$\sum F = Mg + F_d(y) + F_v(u), \quad (4.1)$$

where M is the mass of the intruder and the positive y directions points in the direction of gravity (for simplicity, we also use y to refer to the time dependent depth of the intruder). It should be noted here that there is a strong assumption that this separation can actually be done, which is not clear *a priori*. However, assuming that this separated model is appropriate, one can proceed to discuss the origin of the force terms. The depth-dependent force, $F_d(y)$, may be taken to be a result of resistance by the granular material to impact, which is present even for vanishing velocity. This force is commonly considered to be due to friction, although it was recently observed to be present even if frictional effects were absent [72]. As reported in the literature [31, 42, 72, 83], by exploring analogy with hydrostatic forces which govern propagation through a Newtonian fluid, $F_d(y)$ is expected to vary linearly with y , $F_d \propto y$ for large y , with more complicated behavior expected for smaller y 's [83]. The velocity dependent force, $F_v(u)$, is the inertial drag force, required to push away

the particles in front of the intruder. For an intruder of diameter D and having velocity u , a simple argument [83], suggests that this component of the force scales as $F_v \propto u^2$, although one can also find evidence for linear scaling $F \propto u$ [12, 31].

To examine the depth dependent force $F_d(y)$, we consider a number of different impact velocities, v , and we find the intruder's acceleration as a function of y , at fixed u . For brevity, here we discuss only impacts on polydisperse, disordered systems. Figure 4.30 a), c) and e) shows the results obtained for three systems: Coulomb threshold $\mu = 0$ (frictionless), and $\mu = 0.5$ with kinetic, $k_t = 0.0$, and static, $k_t = 0.8k_n$, friction. For the frictionless case, shown in Figure 4.30 a), we find monotonously increasing $a(h)$, with a dependence which can be described reasonably well by a linear fit, consistent with several previous studies [31, 72]. Friction, however, leads to modifications not only of the linearity, but also of *monotonicity* of the $a(y)$ dependence, as illustrated by parts c) and e) of Figure 4.30, where kinetic and static friction were considered, respectively. The deviation from monotonicity is particularly obvious for small y 's, as expected based on the arguments given in [83]. Therefore, we find that the dependence of intruder's acceleration on time-dependent penetration depth, $y(t)$, is strongly influenced by the frictional properties of the granular material.

Let us now consider the dependence of the intruder's acceleration on its time-dependent velocity, u . To do so, we again consider different initial velocities, v , and find $a(u)$ for fixed y . Figure 4.30 b), d), and e) show the results for the three different friction cases. We extract $a(u)$ for relatively small y 's, where the acceleration is relatively large, in order to decrease the scatter of the results, and we note that for the static friction case, we could extract accelerations only for $y = 1 - 3$, since the total penetration depth is small here. We note that Figure 4.30 does not show any obvious y -dependence (that is, for fixed u , a does not appear to depend on y).

By comparing Figures 4.30 b), d) and e), we see that there is a strong influence of friction on the results. For the parameters considered here, we find approximate

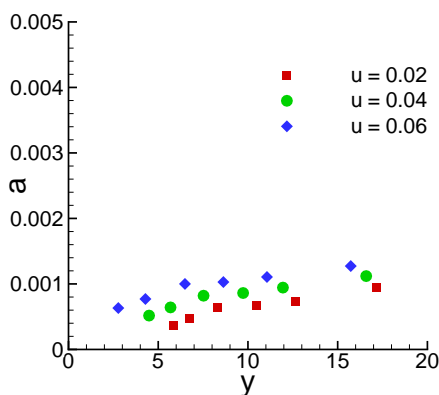
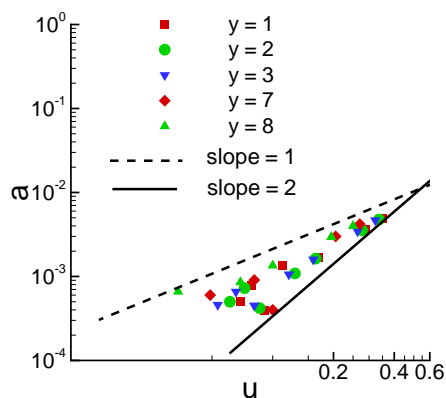
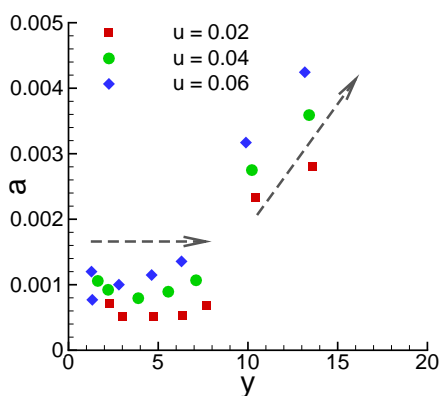
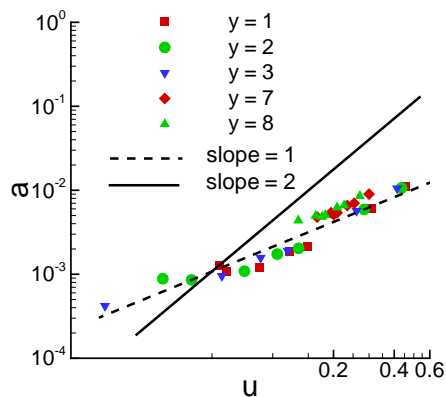
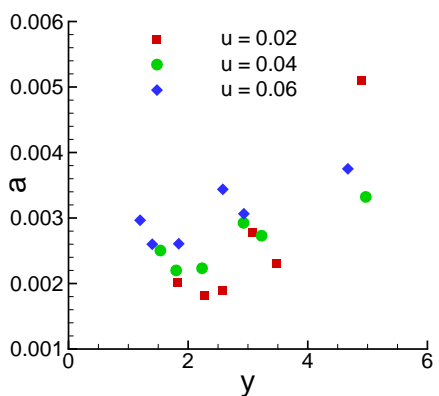
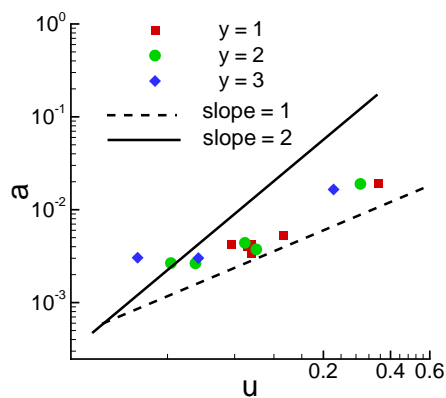
(a) $\mu = 0$.(b) $\mu = 0$.(c) $\mu = 0.5, k_t = 0.0$.(d) $\mu = 0.5, k_t = 0.0$.(e) $\mu = 0.5, k_t = 0.8k_n$.(f) $\mu = 0.5, k_t = 0.8k_n$.

Figure 4.30 Intruder's acceleration versus its time-dependent depth, $y(t)$, and time-dependent velocity, $u(t)$. The impact velocities are $v = 0.05, v = 0.1, v = 0.2, v = 0.3, v = 0.4, v = 0.7$, and $v = 1.0$. The parameters that are not varied are as in Figure 4.2.

power-law scaling, $a \propto u^k$ only for the frictionless and kinetic friction cases. As seen in Figures 4.30 b) and d), the fitting exponent, k , is smaller than the proposed value $k = 2$ [42, 72, 83]; for the frictionless case, we find a best fit with $k \approx 1.4$, and for the kinetic friction case we find $k \approx 1$ [12]. From the frictionless results shown in Figure 4.30 b) it does appear, however, that the slope increases with the depth, y , suggesting that different scaling may be found at different depths. We conjecture that the parameters and penetration depths considered here belong to the ‘intermediate range’ where there is no precisely defined scaling regime [31].

Clearly, more work is needed to understand precisely the nature of the forces determining impact dynamics, and their dependence on the quantities such as the velocity of intruder or its depth. In any case, at least from the point of view of a comparison with physical experiments carried out, necessarily, with frictional particles, the most relevant conclusion is that the speed dependence of the force on the intruder may be influenced strongly by friction model for inter-granular forces. As pointed out [83], this aspect of the problem is complicated by the fact that most particle interaction laws include velocity-dependent frictional damping, which may prevent us from reaching generic answers regarding the dependence of the force on an intruder on its speed.

Finally, we briefly compare our simulations with the available experimental results for the dependence of penetration on the falling distance. In the experiments of Durian et al. [42], it was found that the penetration depth dependence can be well fitted by $D \propto H^{1/3}$, where $H = h + D$, and h is the falling distance before impact. Other investigators have found somewhat different results, suggesting $D \propto v$ [18, 31]. We have already briefly mentioned scaling of D with v , see Figure 4.9, where we saw that approximately, $D \propto v$.

Figure 4.31 shows the results for D for a polydisperse, disordered system (part a)), and for a monodisperse, ordered system, part b). We find that for an impact

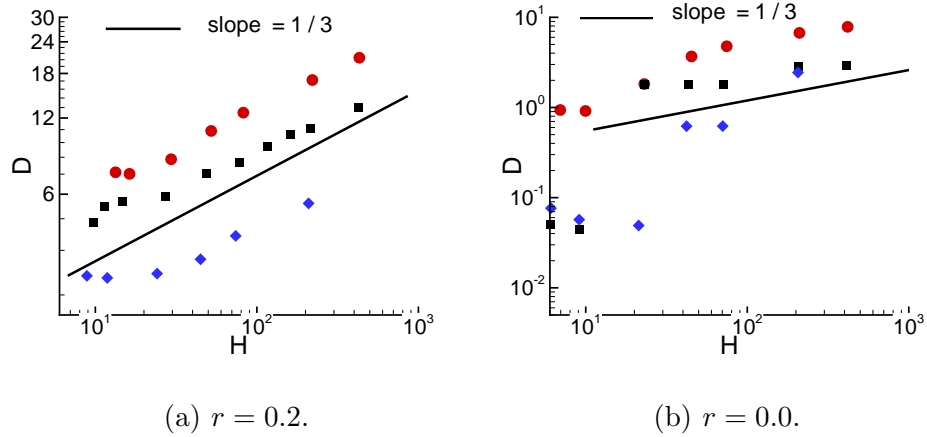


Figure 4.31 Intruder’s total penetration depth, D , versus $H = y_+$, where h is the falling distance. Here, we show $\mu = 0.0$ (red circles), $\mu = 0.5$, $k_t = 0.0$ (black squares), and $\mu = 0.5$, $k_t = 0.8k_n$ (blue diamonds). The parameters that are not varied are as in Figure 4.2.

on a polydisperse system, D can be fitted reasonably well by a power-law using an exponent which is close (although typically a bit smaller) to $1/3$. The main deviation occurs for very small values of H , for which the penetration depth is also very small. However, the quality of the fit is not sufficient to distinguish between $D \propto H^{1/3}$ scaling shown here, or $D \propto v$, suggested by Figure 4.9. We do not find a significant influence of friction model here, aside from significantly smaller penetration depths for the frictional cases.

For impacts on a monodisperse, ordered system, we find that the results are significantly different, in particular for the frictional cases. There is no obvious scaling of the penetration depth with the total falling distance H . This result underscores the fact that an ordered granular microstructure can have a significant influence on the penetration, and in particular penetration depth. Future research should show the generality of this conclusion.

4.7 Conclusion

In this work, we analyze the response of a granular system to an impact, with particular emphasis on understanding the influence of granular microstructure on intruder dynamics. The results show that the grain-scale properties of the granular system itself play a crucial role in determining the dynamics of an intruder. The penetration depth is significantly smaller for impacts on ordered granular material, and the manner in which the forces propagate is strongly influenced by packing. Stronger frictional interactions between the particles play a major role as well. For example, different friction may lead to a change from overshoot to a monotonous increase of penetration depth with time, suggesting that friction plays an important role in determining the nature of the forces that an intruder experiences during impact. Analysis of topological properties of the force field inside the granular materials suggests a strong influence of tangential forces between the granular particles, consistent with the observation that stronger frictional interaction leads to shallower penetration. By analyzing the force field in the granular material, we also confirm the proposed result that static friction leads to a transition from a hyperbolic to an elliptic type of force propagation. A more pronounced pressure dip may be seen below the point of impact in the case of a kinetic friction type of interaction between the granular particles, compared to the static friction case.

To illustrate the influence of friction and of elastic damping on the dynamics, we discuss briefly the evolution of the energy in the system consisting of the intruder and granular particles. Figure 4.32 shows the total, kinetic, potential, and elastic energies as a function of time for combined intruder/granular particles system. For brevity, only the results obtained for polydisperse systems are shown, since the results for ordered monodisperse packings are similar. The total energy, which is the sum of the others shows a monotonous decrease and illustrates faster loss of energy for the systems with friction (kinetic or static). Part b) shows that kinetic energy is lost

very quickly, again faster in the case of frictional systems. Parts c) and d) show that the exchange of energy between potential and elastic components persists for much longer times; the dynamics associated with this exchange is rather weak however, and therefore its signature is not seen in the plot of kinetic energy.

We conclude that the energy evolution is similar for the three types of systems considered here, with the differences between static and kinetic friction models being surprisingly minor. Therefore, energy balance on its own does not provide a complete picture, since, as can be seen clearly in, e.g., Figure 4.7, static friction leads to a significant decrease in the penetration depth. It is clearly necessary to go beyond energy balance and explore the structure of the force field and dynamical response of granular media, in order to gain a better understanding of the interaction of an intruder with a granular system, and its consequences on the final penetration depth.

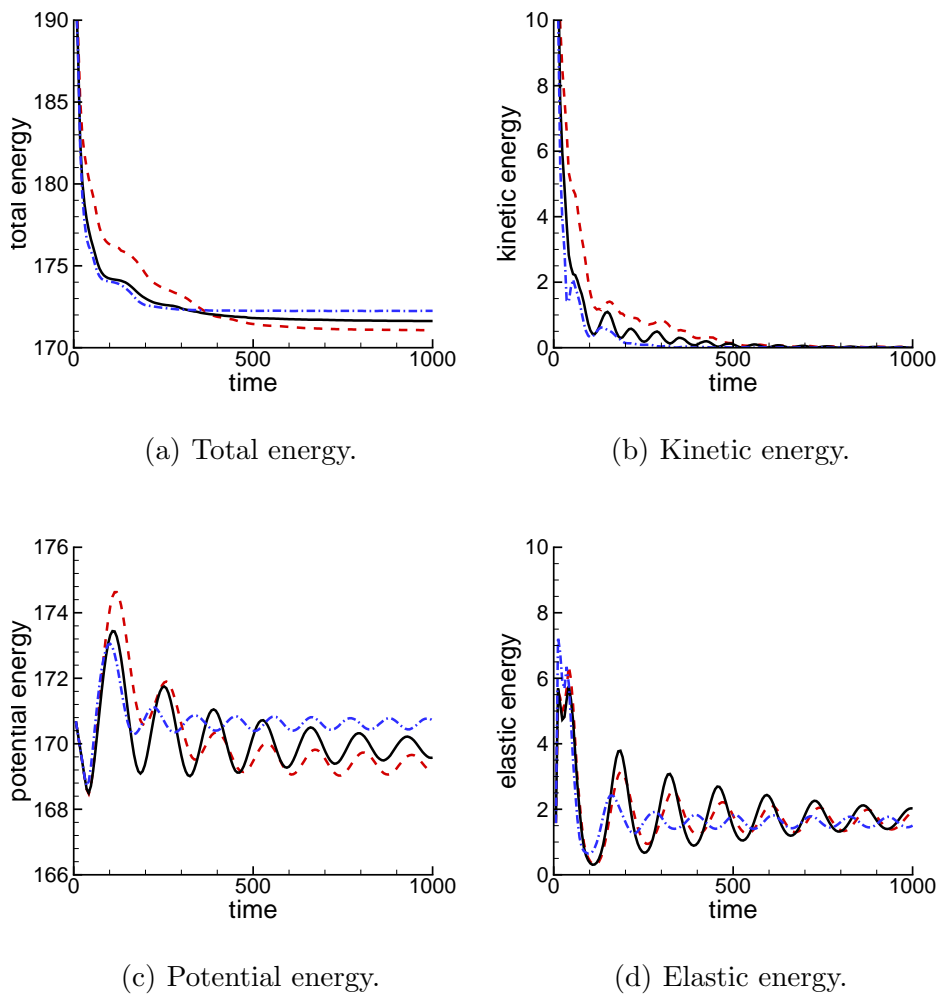


Figure 4.32 Combined energy of the intruder and granular particles during impact for three systems characterized by different frictional properties; penetration depth versus time is shown in Figure 4.7. Here we show the results for: $\mu = 0$ (red dashed); $\mu = 0.5, k_t = 0.0$ (black solid), and $\mu = 0.5, k_t = 0.8k_n$ (blue dash-dot). The parameters are as in Figure 4.7.

CHAPTER 5

HOPPER FLOW

5.1 Introduction

We report on two independent sets of simulations of the flow out of a hopper. The geometry of the setup is taken directly from the experiments reported by Tang and Behringer [80]. Then, the material properties of the granular particles are used to obtain the parameters entering the model. The simulations are based on discrete element simulations of elastic, frictional, disk-like particles. In comparing between the simulations and experiments, we concentrate, in particular, on the survival times (time between consecutive jams) and on the time needed to completely empty the hopper. In addition, we consider velocity and pressure fields in the hopper, as well as their fluctuations.

5.2 System Setup and Material Parameters

In the experiment [80], particles are poured in a hopper consisting of front and back walls, which are placed slightly over one-particle-size apart. After particles are placed in the hopper, the outlet is opened, and the particles flow through under gravity. In simulations, we attempt to reproduce as closely as possible the experimental flow geometry. Figure 5.1 shows the setup used. The width of the hopper is 43 cm. The size of the outlet and the slope of the hopper walls can be controlled. There is a total of 8750 particles, which are bidisperse disks, 62% of which are of diameter 0.602 cm, and 38% are of diameter 0.770 cm. The width of the particles is 0.32 cm. The material properties of the particles provided are as follows:

- density $\rho = 10^3$ kg/m³;
- Young's modulus $Y = 4.8 \times 10^6$ Pa;

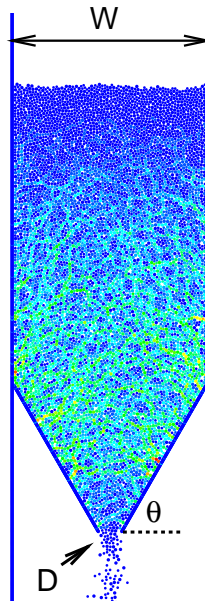


Figure 5.1 Hopper Setup. Particles in the hopper are colored according to the normal force experienced. Gravitational compaction leads to larger forces in the lower parts of the hopper.

- Poisson ratio $\sigma = 0.5$;
- Coefficient of static friction $\mu = 0.7 - 0.8$.
- diameter 0.77 or 0.602 cm.

5.3 Simulation Protocol

Initially, given the outlet size D and the angle, θ , of the inclined walls with the horizontal, particles are placed in the area above the inclined walls on a square lattice. Each particle's diameter is determined by a random number generator. The generator randomly produces a value between 0 and 1. If the number is greater than or equal to 0.62, the particle diameter is taken to be 0.602 cm, otherwise the particle diameter is 0.77 cm. Then, particles are left to settle under gravity (with hopper outlet closed).

The obtained configuration is used as initial condition for the simulations of the flow out of the hopper. As discussed later, we have found that it is necessary to carry out multiple realizations of the flow process in order to reduce statistical noise. For each realization, we re-generate initial configuration by changing the seed for the random number generator, leading to a different initial configuration.

The simulations carried out with smaller size of the outlet, D , lead to particles that jam at the outlet, as in the experiments. To unjam the flow, we shake the inclined hopper walls - similarly as in the experiments where a controlled tap is applied to unjam the flow. To monitor for possible jamming, in the simulations we keep track of the number of particles in the area just below the hopper outlet, of the height equal to $2d$. If no particles are found in this region during time

$$t_{check} = 2\sqrt{\frac{d}{g}}, \quad (5.1)$$

the flow is assumed to be jammed. This value of t_{check} is found to be sufficiently long to ensure that the system is indeed jammed. On the other hand, it is sufficiently short so that it does not lead to a large inaccuracy of the results for jamming time, discussed below. This inaccuracy results from the fact that during t_{check} , it is not known whether the system is jammed or not. The error of estimating survival time in this way is found to be of the order of 0.1 second. The shake itself consists of a single sinusoidal oscillation of amplitude and duration chosen in such a way that it is (almost always) sufficient to unjam the system, without disturbing it significantly. In rare occasions when a single oscillation is not sufficient to unjam the system, consecutive oscillation(s) are applied.

In what follows, we will discuss the empty time (time to empty the whole hopper) and the survival time. The empty time is calculated as the total time it takes to empty all the particles in the hopper, subtracting the shaking time, if any. Figure 5.2 illustrates how the survival time is defined: it is the time between two

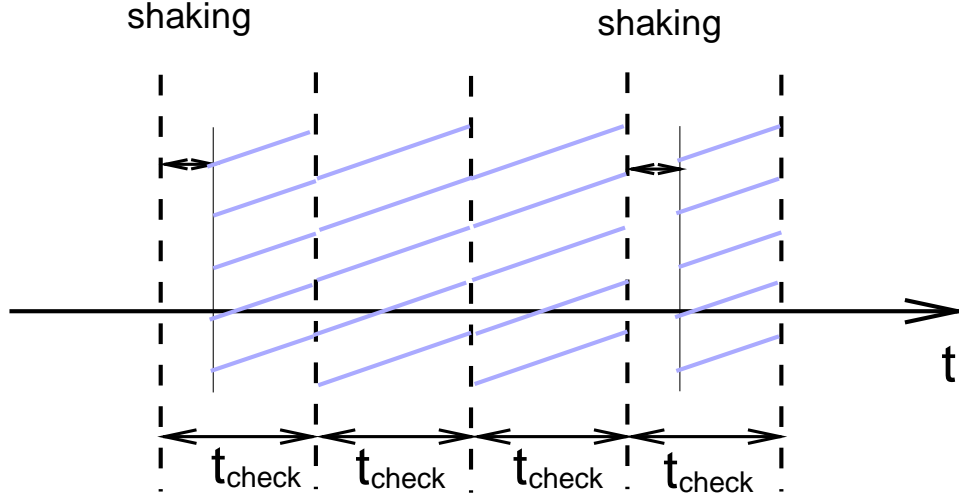


Figure 5.2 Survival time diagram.

consecutive jams/shakes. In our calculation of the survival time, we have not included the time period between after the last shake.

5.4 Calibration of the Model

In our preliminary work, we have carried out single realization simulations where we varied the parameters entering the model. The parameters on which we concentrate are the ones which are not precisely known: the coefficient of restitution, e_n , the friction coefficient, μ , and the force constant, k_n .

Tables 5.1 and 5.2 show the results for the mean survival time for given hopper outlet size, D , and the hopper angle, θ , for a set of values of e_n , μ and k_n for both granular particles and the walls. Table 5.1 concentrates on the case where the flow jams frequently (small outlet); Table 5.2 considers the case where jamming is not observed (large outlet).

The conclusions of the single realization results are as follows:

- Empty times appear insensitive to the model parameters. They are also close, although slightly shorter compared to the experimental value for the same set of parameters, which is reported as 15.87 ± 0.05 seconds.

Table 5.1 Mean Survival Time for Varied System Parameters of Outlet Size $D = 2.7$ cm and Angle $\theta = 45^\circ$ (Single Realization Results)

system e_n	wall e_n	system μ	wall μ	particle k_n	mean survival time (second)
0.5	0.5	0.5	0.8	3350.70	6.20
0.5	0.5	0.6	0.8	3350.70	5.60
0.5	0.5	0.7	0.8	3350.70	2.11
0.5	0.5	0.8	0.8	3350.70	2.76
0.8	0.5	0.5	0.8	3350.70	6.14
0.8	0.5	0.6	0.8	3350.70	5.82
0.8	0.5	0.7	0.8	3350.70	3.03
0.8	0.5	0.8	0.8	3350.70	16.54
0.5	0.3	0.8	0.8	3350.70	8.47
0.5	0.8	0.8	0.8	3350.70	5.24
0.5	0.5	0.8	0.5	3350.70	4.55
0.3	0.5	0.8	0.8	3350.70	2.89
0.5	0.5	0.8	0.8	1000.00	14.46
0.5	0.5	0.8	0.8	3000.00	4.43
0.5	0.5	0.8	0.8	5235.00	5.56

Table 5.2 Empty Time for Varied System Parameters of Outlet Size $D = 4.5$ cm and Angle $\theta = 60^\circ$ (Single Realization Results)

system e_n	wall e_n	system μ	wall μ	empty time (second)
0.5	0.5	0.5	0.8	12.16
0.5	0.5	0.6	0.8	12.54
0.5	0.5	0.7	0.8	13.07
0.5	0.5	0.8	0.8	13.23
0.8	0.5	0.5	0.8	12.17
0.8	0.5	0.6	0.8	12.46
0.8	0.5	0.7	0.8	12.95
0.8	0.5	0.8	0.8	13.22

- Survival times resulting from single realization results are characterized by a large variation, and there is no clear influence of the material parameters. We note in passing that simulations carried out without static friction, $\mu = 0$, or with completely elastic particles, $e_n = 1.0$, do not lead to jamming, suggesting importance of both static friction and inelasticity.

The results regarding survival time suggest that a single realization is not sufficient to obtain statistically relevant results. For this reason, we have carried out multiple (40) realizations in order to improve the statistics. Due to computational expense involved, we have carried out the multiple realizations only for one set of parameters defined as follows: system particles: $e_n = 0.5$, $\mu = 0.7$; walls: $e_n = 0.5$, $\mu = 0.7$, $k_n = 3350.70$. This value of k_n is obtained using the procedure described above.

5.5 The Mass Flow Rate

Studies on granular flow through an outlet have been carried on for a long time. Experimental studies on this subject have been done by many earlier researchers.

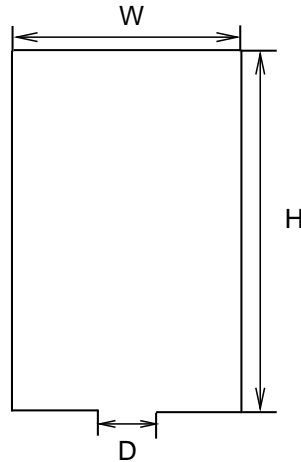


Figure 5.3 Diagram of a hopper.

One aspect among them is the discharge rate through the outlet, and some general agreements have been achieved.

The effect of the size of the hopper and the quantity of material in the hopper, as shown in Figure 5.3, is little. Here, W is the width of the hopper, D is the width of the outlet, and the material height in the outlet is noted as H . It was reported [23] in 1955 that the discharge rate remains constant as long as the height of the material is greater than the width of the hopper, i.e. $H > D$. Later in 1959, similar result [68] was reported and supported the idea that the discharge rate is independent of H until the hopper is almost empty though the precise value of the critical height is not clear. On the other hand, the dependence on D is weak as well provided $W - D > 30d$, where d is the particle diameter.

We see that the relevant characteristic size is D not H or W , if ignoring the possible effect of d . By comparing dimensions between the mass flow rate V

$$[V] = MT^{-1}$$

and the independent parameters

$$[g]^a[\rho]^b[D]^c = \frac{L^a}{T^{2a}} \frac{M^b}{L^{3b}} L^c,$$

where g is the gravitational acceleration and ρ is the bulk density. The dimensional analysis implies that $V \propto \rho g^{1/2} D^{5/2}$.

The interesting power 5/2 can be physically explained. Particles above the outlet seem to have an arch-shaped free-fall zone, whose characteristic size is somehow proportional to the outlet size D . In the zone, particles fall freely under gravity. So the velocity of the particle, v , is proportional to $D^{1/2}$ and therefore the mass flow rate

$$V = \rho v A,$$

where A is the flow area, is proportional to $D^{5/2}$.

Then in 1961, Beverloo found that the power 5/2 varies slightly with different particle diameter d , so he correlated this relation with d and proposed the currently widely accepted law that predicts the mass flow rate of granular materials through an outlet, which has the form:

$$V = C \rho_b \sqrt{g} (D - kd)^{5/2}. \quad (5.2)$$

Here V is the mass flow rate through the outlet, ρ_b is the bulk density, g is the acceleration of gravity, d is the mean diameter of the particles in the hopper, D is the width of the outlet, as shown in Figure 5.3. C and k are fitting coefficients. Both of the coefficients are required to be determined experimentally for every single kind of grains and container properties. The value of C may depend on the friction coefficient, and the other coefficient k generally depends on the particle shape and the slope of the hopper. The validity of the Beverloo law has been tested only for $D \gg d$ so that no jamming event would take place due to the formation of domes (3D) or arches (2D).

Table 5.3 Mean Survival Time Data (Algebraic Means) over 40 Realization Runs

outlet properties	mean survival time (second)	number of jamming events
$D = 2.7$ cm, $\theta = 15^\circ$	3.06	524
$D = 2.7$ cm, $\theta = 30^\circ$	3.53	371
$D = 2.7$ cm, $\theta = 45^\circ$	4.5	261
$D = 2.7$ cm, $\theta = 60^\circ$	6.55	98
$D = 2.9$ cm, $\theta = 15^\circ$	5.58	228
$D = 2.9$ cm, $\theta = 30^\circ$	6.62	146
$D = 2.9$ cm, $\theta = 45^\circ$	6.45	124
$D = 2.9$ cm, $\theta = 60^\circ$	10.10	47
$D = 3.1$ cm, $\theta = 45^\circ$	8.0	48
$D = 3.3$ cm, $\theta = 45^\circ$	10.89	26
$D = 3.5$ cm, $\theta = 45^\circ$	12.53	8

In the same way, in a two-dimensional structure, the Beverloo equation reduces to

$$V = C\rho_b\sqrt{g}(D - kd)^{3/2}. \quad (5.3)$$

5.6 Results

Here we present the results of multiple realization simulations, concentrating first on the survival times which appear to be the most challenging part regarding direct comparison to the experiments. We then proceed with comparing the remaining results available from the experiments [80].

5.6.1 Survival Times

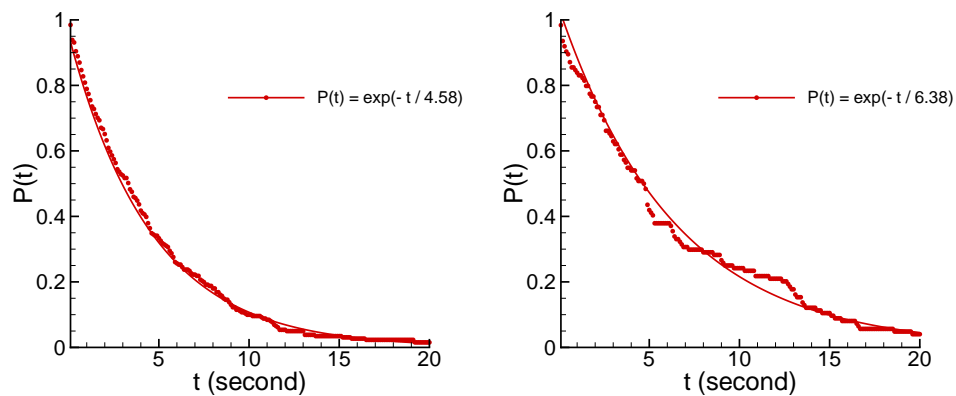
Table 5.3 gives the algebraic mean for the survival times averaged over 40 realizations, together with the total number of jamming events.

As pointed out [80], one may expect that the distribution of survival times obeys Poisson process, that is, the probability that the flow will survive for time t without being jammed is given by $P(t) \propto \exp(-t/\tau)$. To test this model, we consider the distribution of survival times in our simulations. Figure 5.4 shows the results for given D and θ . The main conclusions which can be reached are as follows:

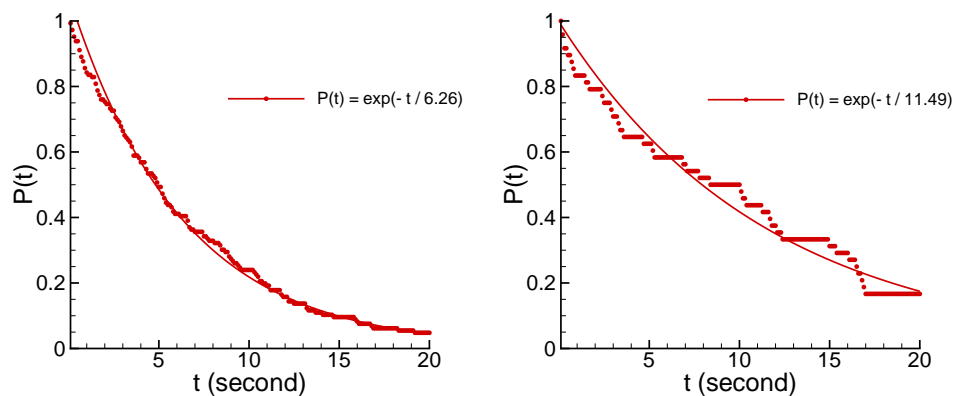
- For small outlets, D (Figures 5.4 a) - d) , we find very good exponential fit to distribution of the survival times, in agreement with the experiments;
- Still for small outlets, the survival times do not appear to depend on the hopper angle, θ , again in full agreement with the experiments (vis. Figure 5.4 b) and c));
- For larger outlet sizes (Figures 5.4 e) and f)), the quality of the fit is not as good anymore, as confirmed by considering χ^2 values of the fits' quality. Clearly, the statistics is not as good for these data, due to a small number of data points available.

Table 5.4 summarizes the data obtained from the exponential fitting, together with the standard deviation of the results for survival times obtained in this manner. By comparison of the average data and the exponential fits (Tables 5.3 and 5.4, respectively), we see that for large D 's, there is a relatively large discrepancy between the time resulting from the fits and from algebraic means (if the Poisson distribution were indeed satisfied, these results would have been close to each other, as for the case of small opening size).

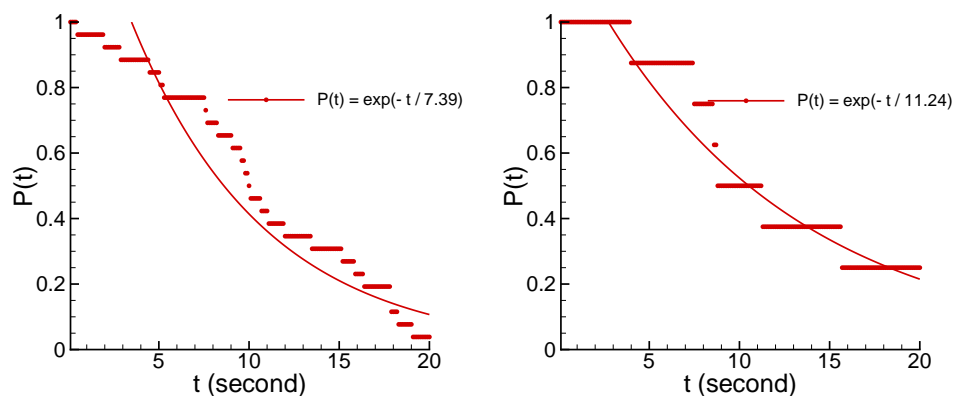
Figure 5.5 shows together the simulation data for mean survival times and the ones resulting from the experiments [80]. We see that both experiments and simulations can be very well fitted by an exponential, although the coefficient in the exponent and prefactor are different. Experimental survival times increase faster with D compared to the simulation ones. We discuss below some possible reasons



(a) $D = 2.7$ cm, $\theta = 45^\circ$, $\chi^2 = 0.9970$ (b) $D = 2.9$ cm, $\theta = 45^\circ$, $\chi^2 = 0.9806$



(c) $D = 2.9$ cm, $\theta = 30^\circ$, $\chi^2 = 0.9862$ (d) $D = 3.1$ cm, $\theta = 45^\circ$, $\chi^2 = 0.9502$



(e) $D = 3.3$ cm, $\theta = 45^\circ$, $\chi^2 = 0.8373$ (f) $D = 3.5$ cm, $\theta = 45^\circ$, $\chi^2 = 0.9429$

Figure 5.4 Distribution of survival times for $D = 2.7$ cm and $\theta = 45^\circ$. The data are obtained from 40 realizations.

Table 5.4 Mean Survival Times and Standard Deviations from Exponential Fitting over 40 Realization Runs

outlet properties	$\theta = 15^\circ$	$\theta = 30^\circ$	$\theta = 45^\circ$	$\theta = 60^\circ$
$D = 2.7$ cm	(3.23, 0.03)	(3.22, 0.06)	(4.57, 0.02)	(6.25, 0.03)
$D = 2.9$ cm	(5.03, 0.04)	(6.25, 0.02)	(6.37, 0.03)	(9.26, 0.06)
$D = 3.1$ cm			(11.49, 0.04)	
$D = 3.3$ cm			(7.4, 0.2)	
$D = 3.5$ cm			(11.24, 0.09)	

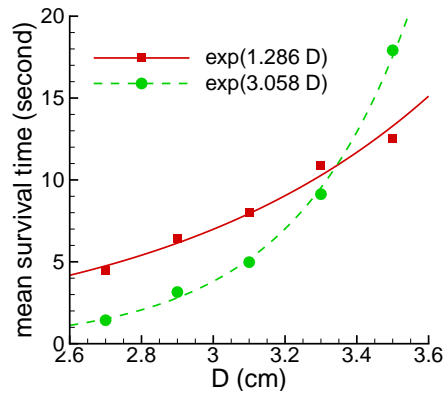


Figure 5.5 Dependence of survival times on the outlet size.

for this discrepancy. Encouraging results is that the general features of the results (exponential dependence) is consistent between the simulations and experiments.

Finally, we discuss whether there is any evidence that survival times may depend on the amount of material in the hopper itself. Figure 5.6 shows the distribution of the number of times jamming occurred as a function of elapsed time for four opening sizes. Within the statistical fluctuations, the jamming times appear to be independent of the elapsed time and therefore on the amount of material in the hopper.

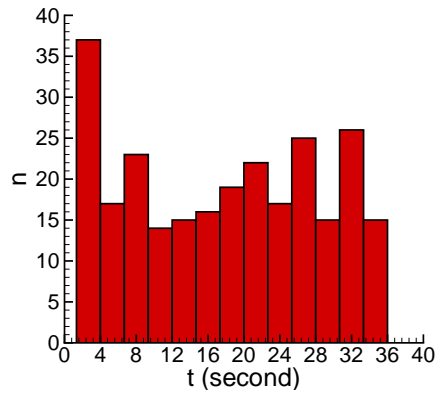
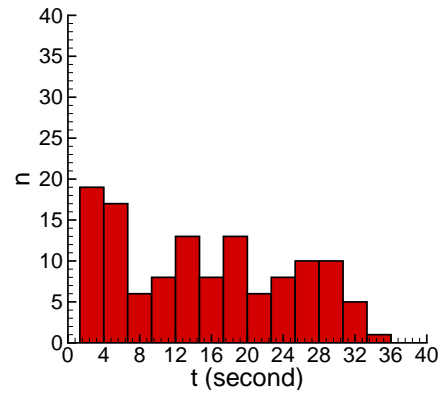
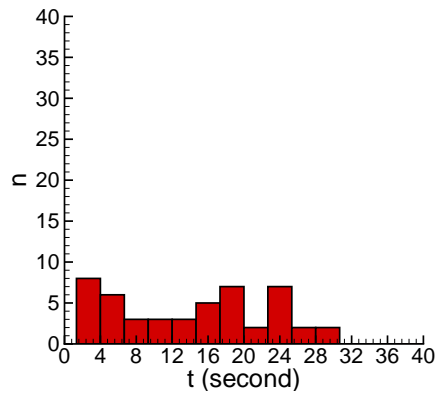
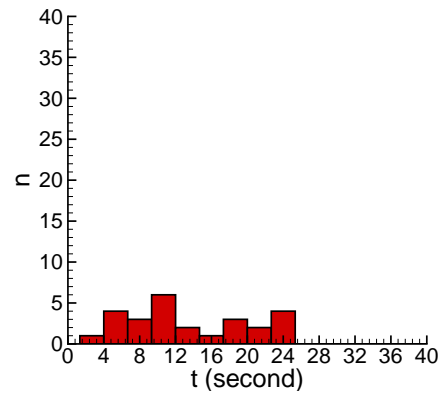
(a) $D = 2.7$ cm.(b) $D = 2.9$ cm.(c) $D = 3.1$ cm.(d) $D = 3.3$ cm.

Figure 5.6 Distribution of survival times as function of elapsed time from the beginning of simulations. Here, $\theta = 45^\circ$. The data are obtained from 40 realizations.

5.6.2 Time to Empty the Hopper and the Mass Flux

Next we discuss the time needed to empty the whole hopper and the corresponding mass flux. Here we consider both small and large outlet sizes (for large outlets jamming is not observed). The results are shown in the context of Beverloo equation [5] which predicts the mass flow rate of the following form (in two spatial dimensions)

$$V = C\rho_b\sqrt{g}(D - kd)^{3/2}. \quad (5.4)$$

Here V is the mass flow rate through the outlet, ρ_b is the bulk density, g is the acceleration of gravity, d is the mean diameter of the particles in the hopper, D is the width of the outlet. C and k are fitting coefficients. The value of C may depend on the friction coefficient, and k generally depends on the particle shape and the slope of the hopper. The validity of the Beverloo law has been tested for $D \gg d$ so that no jamming takes place. Here we check the validity of the proposed scaling for both small and large D 's.

Figures 5.7 and 5.8 shows the results for the flux, V , for different outlet sizes. The part a) shows that the scaling predicted by the Beverloo formulation is satisfied for both small and large outlets. The part b) of this figure shows that the constant k in the Beverloo equation indeed strongly depends on the hopper angle, θ , and it strongly decreases for large θ , as expected based on geometric considerations.

Table 5.5 summarizes the results for empty times for the considered outlet sizes and hopper angles. The results are close to the experimentally observed ones (typically within 10 – 20%).

Figure 5.9 shows the number of particles in the hopper for the case of large opening ($D = 4.5$ cm), as a function of time for different hopper angles. We see that the mass flux (the rate at which the number of particles decreases) is essentially constant, during any given simulation, except close to the end of a simulation and

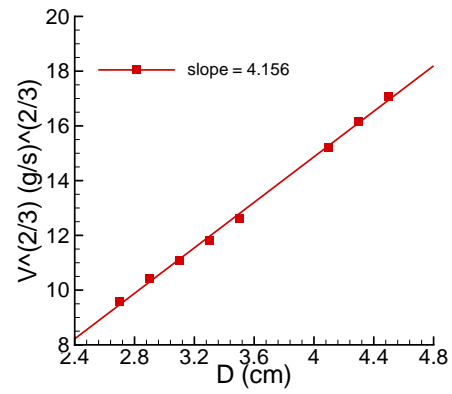


Figure 5.7 Mass flux for $\theta = 45^\circ$.

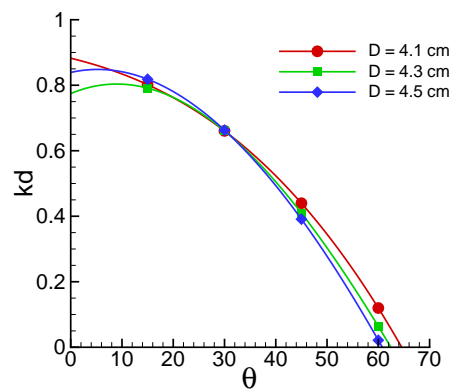


Figure 5.8 Dependence of the constant k from Eq. (5.4) on the outlet angle, θ .

Table 5.5 Mean Empty Time Data (Averages over 40 Realizations are Used for $D \leq 3.5$ cm, and Single Realizations are Reported for Larger D 's Since If There is No Jamming, the Fluctuations between Realizations are Negligible.)

outlet properties	$\theta = 15^\circ$	$\theta = 30^\circ$	$\theta = 45^\circ$	$\theta = 60^\circ$
$D = 2.7$ cm	45.93	41.08	34.45	29.37
$D = 2.9$ cm	39.12	34.88	30.44	27.44
$D = 3.1$ cm			27.83	
$D = 3.3$ cm			25.25	
$D = 3.5$ cm			22.82	
$D = 4.1$ cm	20.19	18.96	17.27	15.23
$D = 4.3$ cm	18.40	17.42	15.76	13.87
$D = 4.5$ cm	17.12	16.09	14.52	12.76

for small outlet angles. Note that the hopper with $\theta = 0^\circ$ never empties since some particles remain at the bottom wall.

5.6.3 Results for Velocities and Pressures

We proceed to discuss the results for the velocities and pressures in the hopper. We compute these quantities by averaging over cells of size 2×2 (in units of d) and furthermore carrying out time averaging as done in the experimental part of the project. More precisely the results are first time-averaged over the interval of 1/100 second, and then the obtained values are averaged over the part of simulation during which considered part of the domain is filled up with particles. The fluctuation plots show standard deviation of the 1/100 second averages. In this section, we concentrate on large outlets where the flow does not jam.

Figure 5.10 shows the velocity vectors at three consecutive time outputs for the specified simulation. We show three snapshots to illustrate variability of the velocity field both in space and in time.

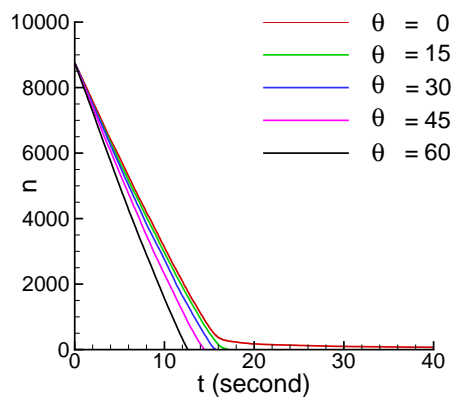


Figure 5.9 Number of particles in the hopper as a function of time for different hopper angles ($D = 4.5$ cm).

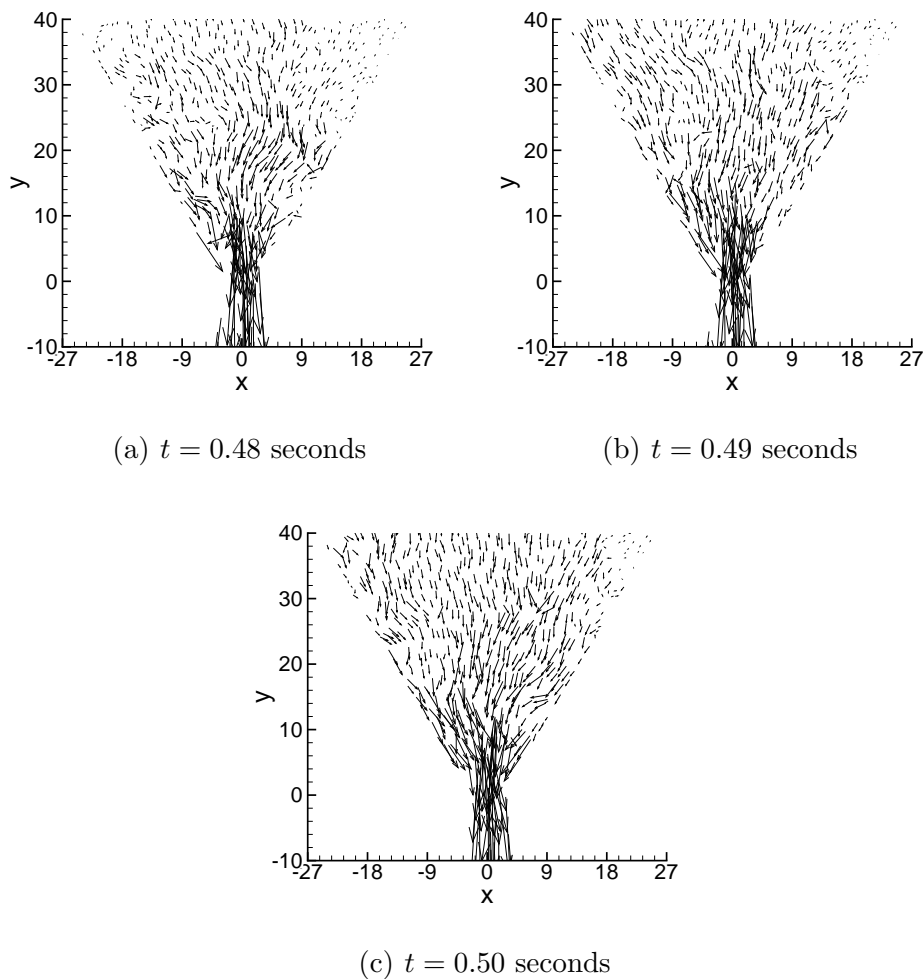


Figure 5.10 Velocity vectors at three consecutive output times (averaged over $1/100$ second). Here $D = 4.1$ cm, $\theta = 60^\circ$.

Figure 5.11 shows contour plots of the averaged velocities for two outlet angles. We find very similar results as in experiments. To illustrate the degree of fluctuations of velocities, we also show standard deviation of the velocity field in Figure 5.12 for $\theta = 60^\circ$. In general, we find that the results for velocities are very similar to the ones found in the experiments [80].

Figures 5.13 and 5.14 show the pressures (more precisely, the normal force which particles experience, in units of mg), averaged over space and time in the same manner as the velocities above. These results again show close resemblance to the experimental ones.

5.7 Summary

To conclude, we discuss the main conclusions and in particular the possible reasons for some discrepancies between the experiments and simulations.

- There is a good agreement between simulations and experiments for a number of results: times to empty the container, the Beverloo equation predictions, the exponential dependence of the survival times on the size of the outlet, all show very good agreement.
- Pressure and velocity fields, as well as their fluctuations closely follow the ones found in the experiments.
- Survival times, although follow the same (exponential) distribution for small outlet sizes as in experiments, overestimate the survival times for the small outlets and underestimate it for the large ones. It should be noted that the fit to exponential distribution is only qualitative for large outlets, which may be one of the reasons for the discrepancy. The other reasons may be (i) over-simplified modeling - the effects such as rolling friction, nonlinear force laws; velocity dependent coefficient of restitution may have an effect; (ii) the experimental

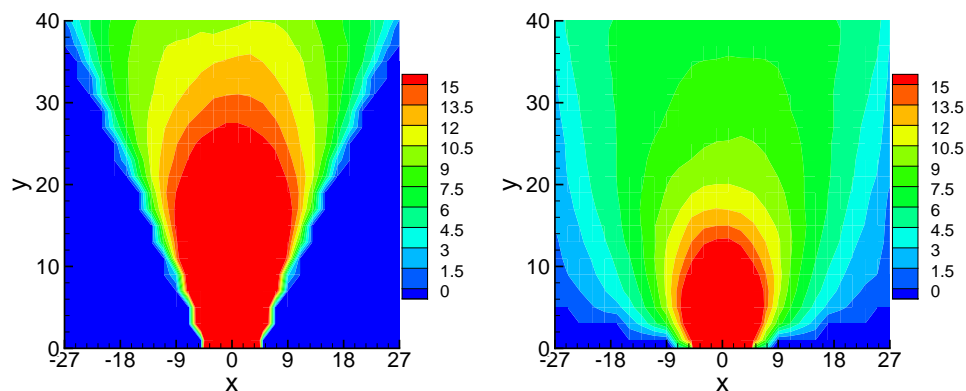
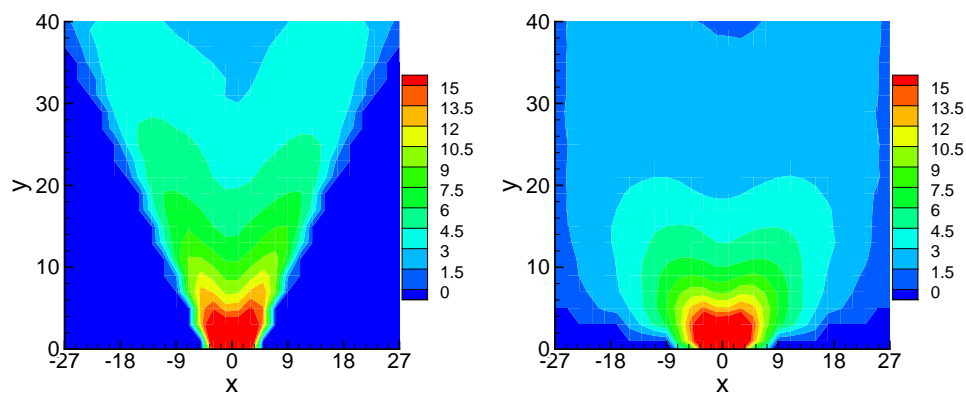
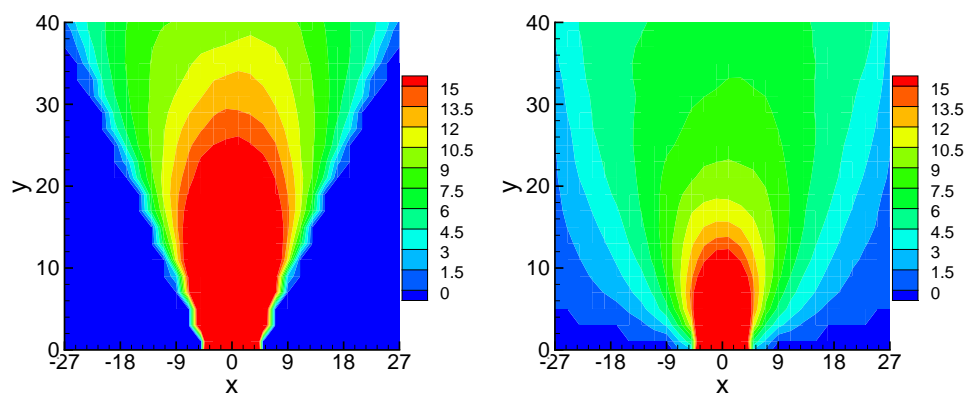
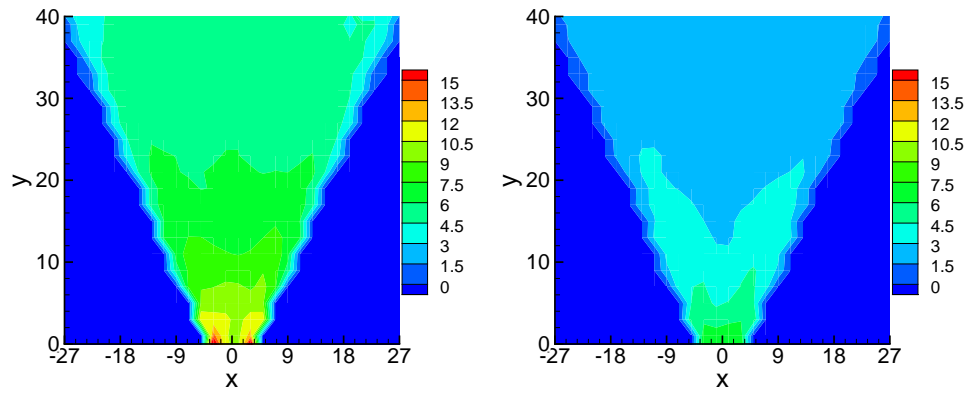
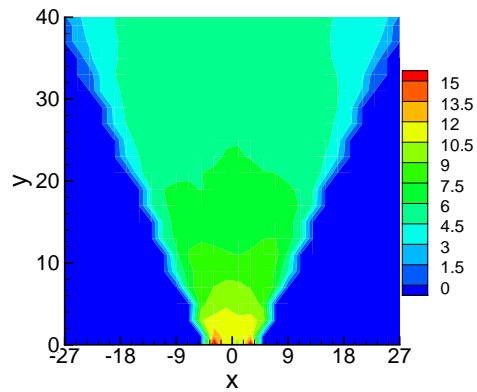
(a) Velocity magnitude, $\theta = 60^\circ$.(b) Velocity magnitude, $\theta = 15^\circ$.(c) x -component of velocity, $\theta = 60^\circ$. (d) x -component of velocity, $\theta = 15^\circ$.(e) y -component of velocity, $\theta = 60^\circ$. (f) y -component of velocity, $\theta = 15^\circ$.

Figure 5.11 Averaged velocity fields for outlet size of $D = 4.5$ cm and two outlet angles. Absolute values of velocity components are shown. Slight waviness next to the hopper walls is due to cell-averaging procedure.



(a) Velocity magnitude.

(b) x -component of velocity.(c) y -component of velocity.**Figure 5.12** Fluctuation of velocity components ($D = 4.5$ cm, $\theta = 60^\circ$).

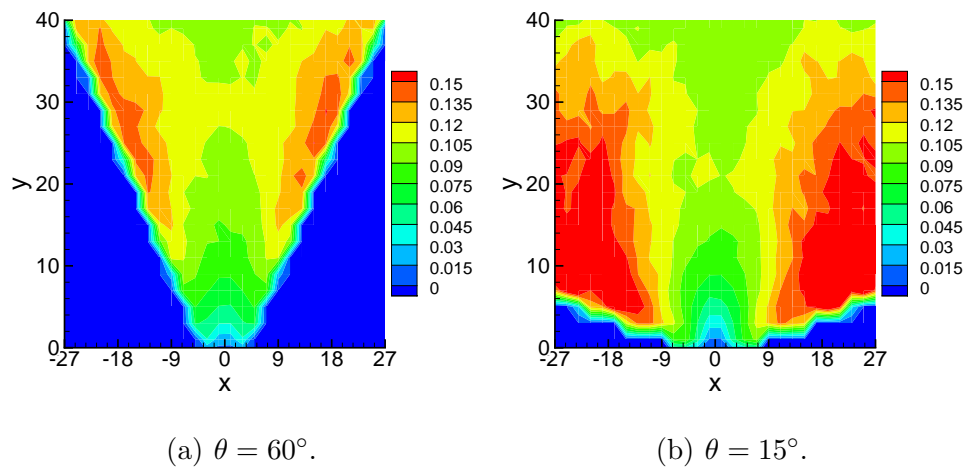


Figure 5.13 Averaged pressure fields for outlet size of $D = 4.5$ cm and two outlet angles.

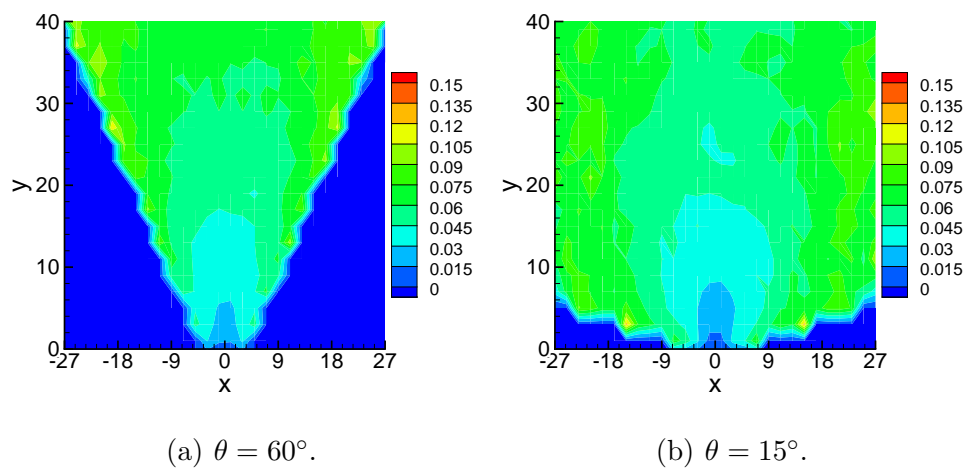


Figure 5.14 Fluctuations of pressure fields for outlet size of $D = 4.5$ cm and two outlet angles.

effects not included in the model, such as air drag and/or interaction with the front and back wall of the hopper.

CHAPTER 6

CONCLUSIONS

In this work, we have considered a few different granular systems and discussed the issues of granular flow and associated energy propagation. In Chapter 2, we provide an overview of the results in simple 1D geometry. These results suggest that a continuum model describing accurately energy propagation should be based on a complex nonlinear wave-type of equations leading to solitary wave type solutions. In Chapter 3, we carry out extensive discrete element (DEM) simulations, discussing in particular propagation of energy from an oscillating boundary. It turns out that a significant insight can be reached by adding a spatial structure to the excitation itself, since comparison to any continuum model becomes much more demanding. This comparison shows that at least for the considered systems, a good agreement can be found by considering a rather simple continuum model - linear wave equation with damping - in place of more complex nonlinear models discussed in the 1D case. While we do not have a precise answer to the question on why such a good description is possible in (more complex) 2D systems, we expect that the disorder of polydisperse (different size) granular particles plays a significant role.

In Chapter 4, we consider force and energy propagation in a system exposed to the impact of a large scale intruder. Again using DEM simulations we discuss response of a granular system to impact, and discuss the processes which govern this response. An additional insight here is reached by considering topological features describing the structure of the force field which develops during impact. These measures, combined with other techniques, allow us to quantify the role of various material properties, such as inter-particle friction, on the force and energy propagation. Furthermore, we discuss a number of scaling laws determining, for example, the depth which an

intruder reaches as a function of its initial velocity. One of the main findings is that inter-particle friction may play a significant role in determining these scaling laws.

The final part of this work, reported in Chapter 5, discusses a slightly different problem of a hopper flow. In particular, we consider situations where a hopper becomes jammed (particles do not flow) and discuss the quantities determining the jamming behavior. We carry out an extensive statistical analysis of the data, since it turns out that the results are strongly realization dependent. One of interesting results here is that the probability of jamming does not appear to depend significantly on the amount of material in the hopper itself.

To conclude, we have carried out extensive discrete element simulations of dense granular materials. Whenever possible, we have compared the simulation results to those obtained for the continuum models, and have clearly identified the situations where continuum models provide a realistic and accurate description of the considered systems. We expect that the results presented here will serve as a basis for future work in this exciting field.

APPENDIX A

MODELING PARTICLE INTERACTIONS

A.1 Force Model

We use a two-dimensional Discrete Element Method (see Appendix B), of disks. Figure A.1 displays two particles, i and j , in collision. We simulate collisions of soft particles, so there are deformations during collision. To model deformations, we simply assume these two particles can slightly overlap each other on the contact point. The governing equations of the linear motion and rotational motion exerted on particle i by the collision are:

$$m_i \frac{d^2 \mathbf{r}_i}{dt^2} = m_i \mathbf{g} + \sum_j (\mathbf{F}_{i,j}^n + \mathbf{F}_{i,j}^t), \quad (\text{A.1})$$

$$I_i \frac{d\boldsymbol{\omega}_i}{dt} = - \sum_j \frac{1}{2} d_i \mathbf{n}_i \times \mathbf{F}_{i,j}^t. \quad (\text{A.2})$$

Here, the index i runs from 1 to the total number of particles used in a system and the index j runs through all particles which collide with particle i . m_i is the mass of particle i , I_i is the particle's moment of inertia, \mathbf{r}_i is the position vector, $\boldsymbol{\omega}_i$ is the vector of angular velocity, d_i is the diameter, the normal direction of particle i is defined as pointing from the other particle j to itself, i.e.,

$$\mathbf{n}_i = \frac{\mathbf{r}_i - \mathbf{r}_j}{|\mathbf{r}_i - \mathbf{r}_j|},$$

and $\mathbf{F}_{i,j}^n$ and $\mathbf{F}_{i,j}^t$ are the force exerted on particle i in its normal and tangential directions, respectively. Its tangential direction will be defined later.

We use the so-called linear spring-dashpot model. In the normal direction, a spring is assumed placed between particles i and j , so the expression for the normal

force is given by

$$\mathbf{F}_{i,j}^n = k_n x \mathbf{n}_i - \gamma_n \bar{m} \mathbf{v}_{i,j}^n.$$

Here,

$$x = \max\{0, \frac{1}{2}(d_i + d_j) - (\mathbf{r}_i - \mathbf{r}_j) \cdot \mathbf{n}_i\}$$

is the overlap between particles i and j in the normal direction, k_n is the normal spring constant, γ_n is the normal damping coefficient,

$$\bar{m} = \frac{m_i m_j}{m_i + m_j}$$

is the reduced mass for this two-body collision. $\mathbf{v}_{i,j}^n$ is the relative velocity in the normal direction between particles i and j . First, the relative velocity between two particles is given by

$$\mathbf{v}_{i,j} = (\mathbf{v}_i - \mathbf{v}_j) - \frac{1}{2}(\omega_i d_i + \omega_j d_j) \mathbf{e}_z \times \mathbf{n}_i$$

where \mathbf{v}_i and \mathbf{v}_j are velocity vectors of particle i and j , respectively. Particles can only rotate in the plane, so both the x and the y components of the angular velocity are zero. In other words, ω_i and ω_j denote the z component of particle i 's and j 's angular velocities. In addition, the relative velocity in the normal direction is defined through the normal direction by

$$\begin{aligned} \mathbf{v}_{i,j}^n &= (\mathbf{v}_{i,j} \cdot \mathbf{n}_i) \mathbf{n}_i \\ &= \left\{ \left[(\mathbf{v}_i - \mathbf{v}_j) - \frac{1}{2}(\omega_i d_i + \omega_j d_j) \mathbf{e}_z \times \mathbf{n}_i \right] \cdot \mathbf{n}_i \right\} \mathbf{n}_i \\ &= ((\mathbf{v}_i - \mathbf{v}_j) \cdot \mathbf{n}_i) \mathbf{n}_i. \end{aligned}$$

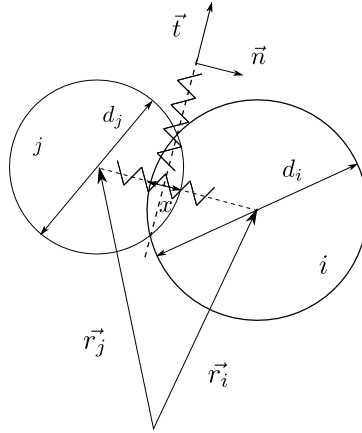


Figure A.1 Diagram of two particles interaction.

Furthermore, the tangential direction is defined through the relative tangential velocity,

$$\mathbf{t}_i = \frac{\mathbf{v}_{i,j}^t}{|\mathbf{v}_{i,j}^t|},$$

and the relative tangential velocity is given by

$$\begin{aligned} \mathbf{v}_{i,j}^t &= \mathbf{v}_{i,j} - \mathbf{v}_{i,j}^n \\ &= (\mathbf{v}_i - \mathbf{v}_j) - (\omega_i d_i/2 + \omega_j d_j/2) \mathbf{e}_z \times \mathbf{n}_i - [(\mathbf{v}_i - \mathbf{v}_j) \cdot \mathbf{n}_i] \mathbf{n}_i \\ &= (\mathbf{v}_i - \mathbf{v}_j) + (\omega_i d_i/2 + \omega_j d_j/2) (n_y, -n_x) - (\mathbf{v}_i - \mathbf{v}_j) \cdot (n_x, n_y) (n_x, n_y) \\ &= (v_{i,j}^x, v_{i,j}^y) + (\omega_i d_i/2 + \omega_j d_j/2) (n_y, -n_x) - [v_{i,j}^x n_x + v_{i,j}^y n_y] (n_x, n_y) \\ &= [v_{i,j}^x + (\omega_i d_i/2 + \omega_j d_j/2) n_y - (v_{i,j}^x n_x + v_{i,j}^y n_y) n_x, \\ &\quad v_{i,j}^y - (\omega_i d_i/2 + \omega_j d_j/2) n_x - (v_{i,j}^x n_x + v_{i,j}^y n_y) n_y] \\ &= [v_{i,j}^x + (\omega_i d_i/2 + \omega_j d_j/2) n_y - (v_{i,j}^x n_x n_x + v_{i,j}^y n_x n_y), \\ &\quad v_{i,j}^y - (\omega_i d_i/2 + \omega_j d_j/2) n_x - (v_{i,j}^x n_x n_y + v_{i,j}^y n_y n_y)]. \end{aligned}$$

It is known that the friction force should be bound from above by the coefficient of static friction, μ multiplied by the normal force. Using a damping term to estimate

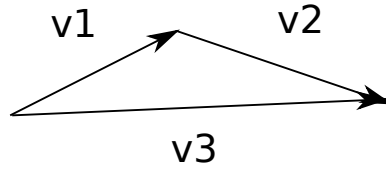


Figure A.2 Direction of $\boldsymbol{\xi}$.

the friction, one comes up with the following ‘kinematic friction model’

$$\mathbf{F}_{i,j}^t = -\min(\gamma_t \bar{m} |\mathbf{v}_{i,j}^t|, \mu |\mathbf{F}_{i,j}^n|) \mathbf{t}_i \quad (\text{A.3})$$

where γ_t is the tangential damping coefficient. We take $\gamma_t = \gamma_n/2$. One problem with this model is that when $\mathbf{v}_{i,j}^t = 0$, the tangential force vanishes. This is not realistic, since, for example, a pile of sand at rest does not collapse. To overcome this problem and in order to depict both the dynamic friction and the static friction, another spring is introduced in the tangential direction, see Figure A.1. When a collision is established between two particles, a spring is assumed to be attached to the contact point in the tangential direction as well, and the tangential deformation is defined by

$$\boldsymbol{\xi} = \int_t \mathbf{v}_{i,j}^t(t) dt. \quad (\text{A.4})$$

Since the direction of $\boldsymbol{\xi}$ is defined through the direction of the tangential velocity $\mathbf{v}_{i,j}^t$ and the tangential velocity may change directions from time to time, the direction of $\boldsymbol{\xi}$ after the integration is not actually in the current tangential direction. See Figure A.2 for example. Suppose $\mathbf{v}_{i,j}^t$ is $\mathbf{v1}$ at time t , after one simulation time dt , $\mathbf{v}_{i,j}^t$ becomes $\mathbf{v2}$, then the direction of $\boldsymbol{\xi}$ at time $t + dt$ is in the same direction as $\mathbf{v3}$ according to Eq. A.4. However, the direction of the tangential spring should be always in the same direction as the tangential direction, which is also defined in the same direction of $\mathbf{v}_{i,j}^t$. So the direction of $\boldsymbol{\xi}$ at time $t + dt$ has to be in the same direction as $\mathbf{v2}$. For this reason, at each simulation time, we remap $\boldsymbol{\xi}$ to use the actual tangential

deformation.

$$\boldsymbol{\xi} \leftarrow \boldsymbol{\xi} - \mathbf{n}_i(\mathbf{n}_i \cdot \boldsymbol{\xi}), \quad (\text{A.5})$$

and the newly assigned $\boldsymbol{\xi}$ on the left side of Eq. (A.5) is the correct tangential deformation coming into the following calculation. Now the tangential force is obtained first through a test force,

$$\mathbf{F}_{test}^t = -k_t \boldsymbol{\xi} - \gamma_t \bar{m} \mathbf{v}_{i,j}^t \quad (\text{A.6})$$

where k_t and γ_t are the spring constant and damping constant in the tangential direction. If the test force is less than the static friction threshold

$$|\mathbf{F}_{test}^t| < |\mu \mathbf{F}_{i,j}^n|,$$

then we have static friction and $\boldsymbol{\xi}$ still goes by definition, i.e.,

$$\boldsymbol{\xi} \leftarrow \boldsymbol{\xi} + \mathbf{v}_t dt_{MD}$$

where dt_{MD} is one simulation time step, and the test force is the tangential force,

$$\mathbf{F}_{i,j}^t = \mathbf{F}_{test}^t.$$

If, on the other hand, the test force is greater than the static friction threshold,

$$|\mathbf{F}_{test}^t| > |\mu \mathbf{F}_{i,j}^n|,$$

then dynamic friction comes into play. Thus, we take the threshold as the magnitude of the tangential force converted into the current tangential direction

$$\mathbf{F}_{i,j}^t = \mu |\mathbf{F}_{i,j}^n| \frac{\mathbf{F}_{test}^t}{|\mathbf{F}_{test}^t|}$$

and retrieve the tangential deformation from Eq.(A.6) as the new $\boldsymbol{\xi}$

$$\boldsymbol{\xi} = -\frac{1}{k_t} (\mu |\mathbf{F}_{i,j}^n| \frac{\mathbf{F}_{test}^t}{|\mathbf{F}_{test}^t|} + \gamma_t \mathbf{F}_{i,j}^t).$$

We refer to tangential force defined above as Model II, and tangential force given by Eq. (A.3) as Model I. Model I is also specified by $k_t = 0.0$ and $k_t \neq 0.0$ for Model II. Here $k_t = 0.0$ simply indicates there is no tangential spring.

A.2 Key Parameters

In the simulation, we have to choose the values of all the parameters. Some of them are easy to give, i.e., the mass and the diameter of the particles, but some are not so obviously determined, i.e., the spring constant. Thus, in this section, we retrieve the information from analysis of the material properties.

Collision time t_{col} : In the MD simulation, all the values of particles are integrated over a 'small' time step. Thus, we need to know the duration of a typical collision between two particles. This collision time t_{col} is connected with the material properties of the particles we simulate. We start with the commonly used nonlinear equation [43], since the shape of the deformation depends on the compression and a linear model is not accurate enough to estimate the collision time.

$$\bar{m} \frac{d^2x}{dt^2} + \eta d x^\gamma \frac{dx}{dt} + Ed x^{\beta+1} = 0,$$

where x is still the compression between particles, d is the diameter of a particle, $\bar{m} = (m_1 + m_2)/m_1 m_2$ is the reduced mass of the collision, m_1 and m_2 being the mass of the two particles, and η and E are the material constants. The bulk modulus, $E = Y/[3(1 - \sigma^2)]$, depends on the Young's modulus Y and the Poisson ratio σ . η , on the other hand, depends on both the bulk modulus and the shear modulus.

Integrating the last term in the above equation, we can obtain the expression for the elastic energy E_e stored during the collision, as

$$E_e = \frac{Ed}{\beta + 2} x^{\beta+2}.$$

Upon impact, the initial kinetic energy is converted partly into a reduced kinetic energy and partly into elastic energy. Thus, we write

$$\frac{1}{2}\bar{m}v_0^2 = \frac{1}{2}\bar{m}\left(\frac{dx}{dt}\right)^2 + \frac{Ed}{\beta+2}x^{\beta+2}, \quad (\text{A.7})$$

where v_0 is the initial impact velocity. The velocity drops to zero when the two particles have penetrated each other at maximal distance, x_{max} . At that moment, $dx/dt = 0$, and we have

$$x_{max} = \left(1 + \frac{\beta}{2}\right)^{\frac{1}{\beta+2}} \left(\frac{\bar{m}}{Ed}\right)^{\frac{1}{\beta+2}} v_0^{\frac{2}{\beta+2}}.$$

Thus, the entire duration of the collision is obtained by integrating Eq. (A.7)

$$t_{col} = 2 \int_0^{x_{max}} \frac{dx}{\sqrt{v_0^2 - \frac{2Ed}{\bar{m}(\beta+2)}x^{\beta+2}}}.$$

Let $y = x^{\beta+2}$,

$$t_{col} = 2 \int_0^{(1+\frac{\beta}{2})\frac{\bar{m}}{Ed}v_0^2} \frac{\frac{1}{\beta+2}y^{-\frac{\beta+1}{\beta+2}}dy}{\sqrt{v_0^2 - \frac{2Ed}{\bar{m}(\beta+2)}y}}.$$

Let $y = z^2$,

$$t_{col} = \frac{2}{\beta+2} \int_0^{\sqrt{(1+\frac{\beta}{2})\frac{\bar{m}}{Ed}v_0^2}} \frac{z^{-2\frac{\beta+1}{\beta+2}}2zdz}{\sqrt{v_0^2 - \frac{2Ed}{\bar{m}(\beta+2)}z^2}}.$$

Let $z = \sqrt{(1+\frac{\beta}{2})\frac{\bar{m}}{Ed}v_0^2}\alpha$,

$$\begin{aligned} t_{col} &= \frac{2}{\beta+2} \int_0^1 \frac{2 \left[(1+\frac{\beta}{2})\frac{\bar{m}}{Ed}v_0^2\alpha^2 \right]^{-\frac{\beta+1}{\beta+2}} (1+\frac{\beta}{2})\frac{\bar{m}}{Ed}v_0^2\alpha d\alpha}{\sqrt{v_0^2 - v_0^2\alpha^2}} \\ &= \frac{2}{\beta+2} \left[(1+\frac{\beta}{2})\frac{\bar{m}}{Ed} \right]^{\frac{1}{\beta+2}} v_0^{1-2\frac{\beta+1}{\beta+2}} \int_0^1 \frac{2\alpha^{1-2\frac{\beta+1}{\beta+2}}}{\sqrt{1-\alpha^2}} d\alpha \\ &= \frac{2}{\beta+2} \left[(1+\frac{\beta}{2})\frac{\bar{m}}{Ed} \right]^{\frac{1}{\beta+2}} v_0^{-\frac{\beta}{\beta+2}} \int_0^1 \frac{2\alpha^{-\frac{\beta}{\beta+2}}}{\sqrt{1-\alpha^2}} d\alpha. \end{aligned}$$

Let $\alpha = \sin \theta$,

$$\int_0^1 \frac{2\alpha^{-\frac{\beta}{\beta+2}}}{\sqrt{1-\alpha^2}} d\alpha = \int_0^{\pi/2} \frac{2(\sin \theta)^{-\frac{\beta}{\beta+2}} \cos \theta}{\cos \theta} d\theta = \int_0^{\pi/2} 2(\sin \theta)^{-\frac{\beta}{\beta+2}} d\theta.$$

Considering the Beta function

$$B(x, y) = 2 \int_0^{\pi/2} (\sin \theta)^{2x-1} (\cos \theta)^{2y-1} d\theta,$$

and taking $x = \frac{1}{\beta+2}$ and $y = \frac{1}{2}$, we have

$$\int_0^1 \frac{2\alpha^{-\frac{\beta}{\beta+2}}}{\sqrt{1-\alpha^2}} d\alpha = B\left(\frac{1}{\beta+2}, \frac{1}{2}\right) = \frac{\Gamma(\frac{1}{\beta+2})\Gamma(\frac{1}{2})}{\Gamma(\frac{1}{\beta+2} + \frac{1}{2})} = \frac{\Gamma(\frac{1}{\beta+2})\Gamma(\frac{1}{2})}{\Gamma(\frac{\beta+4}{2\beta+4})} = \frac{\sqrt{\pi}\Gamma(\frac{1}{\beta+2})}{\Gamma(\frac{\beta+4}{2\beta+4})}$$

since

$$B(x, y) = \frac{\Gamma(x)\Gamma(y)}{\Gamma(x+y)},$$

and

$$\Gamma\left(\frac{1}{2}\right) = \sqrt{\pi}.$$

Finally,

$$t_{col} = I(\beta) \left[1 + \frac{\beta}{2}\right]^{1/(2+\beta)} \left[\frac{\bar{m}}{Ed^{1-\beta}}\right]^{1/(2+\beta)} v_0^{-\beta/(2+\beta)}. \quad (\text{A.8})$$

and

$$I(\beta) = \frac{\sqrt{\pi}\Gamma\left(\frac{1}{2+\beta}\right)}{(1 + \beta/2)\Gamma\left(\frac{4+\beta}{4+2\beta}\right)} = \begin{cases} \pi & \text{for } \beta = 0; \\ 2.94 & \text{for } \beta = \frac{1}{2}, \end{cases}$$

where $\Gamma(z)$ is the gamma function. Here $\beta = 0$ indicates a linear model and $\beta = 0.5$ indicates the Hertz model. Normally, we can choose $\beta = 0.5$ for better approximation and the values of all the other known physical parameters to estimate t_{col} .

Spring constant k_n : We expect that the stiffness of a particle, or the spring constant k_n in our model, relates to the collision time t_{col} . The greater the stiffness of

particles, the shorter the time two particles are in contact during a collision. Here, we find a relation between a typical collision duration of two particles and their spring constant. Since we use a linear spring to describe the deformation between particles in our force model, the compression x satisfies

$$\bar{m} \frac{d^2 x}{dt^2} + \bar{m} \gamma_n \frac{dx}{dt} + k_n x = 0, \quad (\text{A.9})$$

or

$$\frac{d^2 x}{dt^2} + \gamma_n \frac{dx}{dt} + \omega_0^2 x = 0,$$

where γ_n is the damping constant in the normal direction and $\omega_0 = \sqrt{k_n/\bar{m}}$. We only discuss the underdamped case when $\gamma_n \ll \omega_0$, which resembles real materials. The initial conditions are

$$x(0) = 0,$$

and

$$\frac{dx}{dt}(0) = v_0,$$

Applying the initial condition, we find the solution as

$$x = A e^{-\frac{\gamma_n}{2} t} \sin \left[\sqrt{\omega_0^2 - \left(\frac{\gamma_n}{2}\right)^2} t \right].$$

Now the collision duration is the first positive time at which $x(t = t_{col}) = 0$, so

$$t_{col} = \frac{2\pi}{\sqrt{\omega_0^2 - \left(\frac{\gamma_n}{2}\right)^2}} \approx \frac{2\pi}{\omega_0} = 2\pi \sqrt{\frac{\bar{m}}{k_n}}.$$

Thus, the normal spring constant k_n is determined by the collision time t_{col} through

$$k_n = \bar{m} \left(\frac{2\pi}{t_{col}} \right)^2.$$

Damping coefficient γ_n : Now we determine the values of the damping coefficient γ_n and γ_t through the coefficient of restitution e_n , which is defined as the ratio of the speed of a particle after a collision v_f to its speed before the collision v_o , i.e.,

$$e_n = \frac{v_f}{v_o}.$$

Following the same notation, we can obtain the expression of x' from the expression of x , then evaluate it at t_{col} , so

$$e_n = \frac{v_f}{v_o} = \frac{x'(t_{col})}{v_0} = e^{-\frac{\gamma_n}{2}t_{col}}.$$

Therefore,

$$\gamma_n = -\frac{2 \ln e_n}{t_{col}}.$$

In an elastic collision, $e_n = 1$. In our simulation, e_n varies between 0.5 to 0.9. The tangential damping constant γ_t is chosen to be $\gamma_n/2$.

APPENDIX B

DISCRETE ELEMENT TECHNIQUES

The general scheme of a discrete element method (DEM), based on a predictor-corrector algorithm, is described step-by-step in this section. ***.f** denotes any FORTRAN subroutine code used in the simulation.

init.f: Initial values of all the variables and parameters are set here.

predictor.f: The particle's positions $\mathbf{x0}$, linear velocities $\mathbf{x1}$, linear accelerations $\mathbf{x2}$, angular motion related variables $\mathbf{x1}_{rot}$, and $\mathbf{x2}_{rot}$ etc. at next time step are predicted using the current values of these quantities, simply by Taylor Expansion.

$$\begin{aligned}\mathbf{x0}(t + \delta t) &= \mathbf{x0}(t) + \delta t \mathbf{x1}(t) + \frac{1}{2} \delta t^2 \mathbf{x2}(t) + \frac{1}{6} \delta t^3 \mathbf{x3}(t) + \dots \\ \mathbf{x1}(t + \delta t) &= \mathbf{x1}(t) + \delta t \mathbf{x2}(t) + \frac{1}{2} \delta t^2 \mathbf{x3}(t) + \dots \\ \mathbf{x2}(t + \delta t) &= \mathbf{x2}(t) + \delta t \mathbf{x3}(t) + \dots \\ \mathbf{x3}(t + \delta t) &= \mathbf{x3}(t) + \dots \\ \mathbf{x1}_{rot}(t + \delta t) &= \mathbf{x1}_{rot}(t) + \delta t \mathbf{x2}_{rot}(t) + \frac{1}{2} \delta t^2 \mathbf{x3}_{rot}(t) + \dots \\ \mathbf{x2}_{rot}(t + \delta t) &= \mathbf{x2}_{rot}(t) + \delta t \mathbf{x3}_{rot}(t) + \dots \\ \mathbf{x3}_{rot}(t + \delta t) &= \mathbf{x3}_{rot}(t) + \dots\end{aligned}$$

He we point out for the purpose of computational convenience, $\mathbf{x1}_{rot} = d\boldsymbol{\omega}/2$ rather than simply angular velocity $\boldsymbol{\omega}$.

Introducing new variables as follow:

$$\begin{aligned}
 \mathbf{x0}' &= \mathbf{x0} \\
 \mathbf{x1}' &= \delta t \mathbf{x1} \\
 \mathbf{x2}' &= \frac{1}{2} \delta t^2 \mathbf{x2} \\
 \mathbf{x3}' &= \frac{1}{6} \delta t^3 \mathbf{x3} \\
 \mathbf{x1}'_{rot} &= \delta t \mathbf{x1}_{rot} \\
 \mathbf{x2}'_{rot} &= \frac{1}{2} \delta t^2 \mathbf{x2}_{rot} \\
 \mathbf{x3}'_{rot} &= \frac{1}{6} \delta t^3 \mathbf{x3}_{rot}
 \end{aligned}$$

Replacing $\mathbf{x0}$, $\mathbf{x1}$, $\mathbf{x2}$, $\mathbf{x3}$, $\mathbf{x1}_{rot}$, $\mathbf{x2}_{rot}$, and $\mathbf{x3}_{rot}$ by $\mathbf{x0}'$, $\mathbf{x1}'$, $\mathbf{x2}'$, $\mathbf{x3}'$, $\mathbf{x1}'_{rot}$, $\mathbf{x2}'_{rot}$, and $\mathbf{x3}'_{rot}$ and dropping ' ' from the new variables, the predicted values are given by

$$\begin{aligned}
 \mathbf{x0} &= \mathbf{x0} + \mathbf{x1} + \mathbf{x2} + \mathbf{x3} \\
 \mathbf{x1} &= \mathbf{x1} + 2\mathbf{x2} + 3\mathbf{x3} \\
 \mathbf{x2} &= \mathbf{x2} + 3\mathbf{x3} \\
 \mathbf{x3} &= \mathbf{x3}
 \end{aligned}$$

Similarly, the angular motion related variables take the same form as

$$\begin{aligned}
 \mathbf{x1}_{rot}(t + \delta t) &= \mathbf{x1}_{rot}(t) + 2\mathbf{x2}_{rot}(t) + 3\mathbf{x3}_{rot}(t) \\
 \mathbf{x2}_{rot}(t + \delta t) &= \mathbf{x2}_{rot}(t) + 3\mathbf{x3}_{rot}(t) \\
 \mathbf{x3}_{rot}(t + \delta t) &= \mathbf{x3}_{rot}(t)
 \end{aligned}$$

make_list.f: Now we would like to know which particles are in contact with which particles at one iteration. In this subroutine, we only identify the potential pairs of particles which are mostly likely to collide. If we simply take each particle as a pair with all the other particles, the computation would cost a lot of time and it is

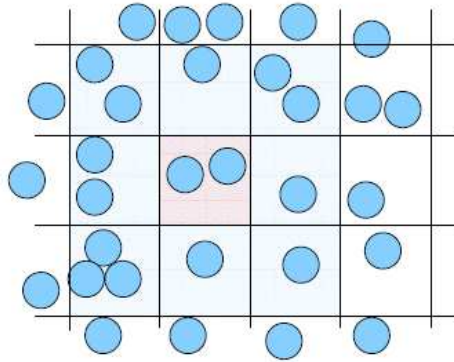


Figure B.1 Illustration of cells in `make_list.f`.

not necessary, because particles are only able to contact particles which are close to them. Thus, we divide the whole simulation domain into $\mathbf{NBX} \times \mathbf{NBY}$ cells with even size. Each cell has eight neighboring cells surrounding it, see Figure B.1. The outer loop first runs through all the cells. For each cell, for example, the red-shaded one in the center, all the pairs of particles in the cell itself are collected and then one particle from this cell and one particle from its 'five neighboring cells' are collected. The reason of only choosing from the five upper and right cells is to avoid repeated counting. All the candidate pairs are stored for later use.

force.f: The motion of particles are taken into account here. First, we determine if the candidate pairs obtained from 'make_list' subroutine are indeed in contact, i.e. the overlap between them $x > 0$. If they are, then the forces, and hence the linear and rotational accelerations \mathbf{xnp} and \mathbf{xnp}_{rot} are calculated through equations (A.1) and (A.2) as

$$\begin{aligned} \mathbf{xnp}_i &= \frac{d^2 \mathbf{x0}_i}{dt^2} = \mathbf{g} + \frac{1}{d_i^2} \mathbf{F}_i^n \\ \mathbf{xnp}_{rot,i} &= \frac{1}{2} d_i \frac{d\boldsymbol{\omega}_i}{dt} = -\frac{1}{d_i^2} (2\mathbf{n} \times \mathbf{F}_i^t). \end{aligned}$$

collision.f: 'collision' subroutine is used inside the force subroutine. For each collision, the deformation of tangential spring evolves with time, so we need to track

this information all along. The array $\mathbf{ncd}(i, :)$ stores the index of all the particles that particle i is in contact with, in an ascending order. And we only store the information of the particle with the smaller index in the pair. Three cases may occur. First, the contact is newly established and there is no existing spring for the collision pair at all; then we assign a tangential spring to them. Second, or the contact is already in the list, then the calculation of ξ follows from the force model. Third, or there are existing springs but the current collision pair is not one of them. In this case, we need to assign a new spring to them and put the index number in the right position in $\mathbf{ncd}(i, :)$ and move all the others after it down.

In addition, after one iteration, if we find an existing spring is not being updated, then it no long exists. We remove it by shifting all the information of particles with index after it up.

corrector.f: The error between the correct acceleration (force subroutine) and the predicted acceleration (predictor subroutine) is

$$\mathbf{xnp}(t + \delta t) = \mathbf{x2}_{correct}(t + \delta t) - \mathbf{x2}(t + \delta t).$$

Here \mathbf{xnp} are just what we have obtained in the force subroutine and are used to correct the predicted results in the form of

$$\begin{aligned} \mathbf{x0}(t + \delta t) &\leftarrow \mathbf{x0}(t + \delta t) + c_0 \mathbf{xnp}(t + \delta t) \\ \mathbf{x1}(t + \delta t) &\leftarrow \mathbf{x1}(t + \delta t) + c_1 \mathbf{xnp}(t + \delta t) \\ \mathbf{x2}(t + \delta t) &\leftarrow \mathbf{x2}(t + \delta t) + c_2 \mathbf{xnp}(t + \delta t) \\ \mathbf{x3}(t + \delta t) &\leftarrow \mathbf{x3}(t + \delta t) + c_3 \mathbf{xnp}(t + \delta t) \\ \mathbf{x1}_{rot}(t + \delta t) &\leftarrow \mathbf{x1}_{rot}(t + \delta t) + c_1 \mathbf{xnp}_{rot}(t + \delta t) \\ \mathbf{x2}_{rot}(t + \delta t) &\leftarrow \mathbf{x2}_{rot}(t + \delta t) + c_2 \mathbf{xnp}_{rot}(t + \delta t) \\ \mathbf{x3}_{rot}(t + \delta t) &\leftarrow \mathbf{x3}_{rot}(t + \delta t) + c_3 \mathbf{xnp}_{rot}(t + \delta t) \end{aligned}$$

where $c_0 = 1/6$, $c_1 = 5/6$, $c_2 = 1$ and $c_3 = 1/3$. The choices of these c_i 's are determined by the order of Taylor Series used in the approximation.

output.f: Values of interest are calculated in this step before going back to the next iteration.

APPENDIX C

CONTINUUM MODEL FOR ENERGY PROPAGATION

C.1 Eigenfunction Approach

$$\frac{1}{c^2}u_{tt} + \frac{1}{D}u_t = \nabla^2 u, \quad -L < x < L, \quad 0 < y < H$$

$$u(-L, y, t) = u(L, y, t)$$

$$u_x(-L, y, t) = u_x(L, y, t)$$

$$u(x, 0, t) = U \sin(\omega t) \cos\left(\frac{2\pi kx}{L}\right)$$

$$u(x, H, t) = 0$$

$$u(x, y, 0) = 0$$

$$u_t(x, y, 0) = 0$$

By applying the method of separation of variables, we obtain the eigenvalue problem:

$$\nabla^2 \phi = -\lambda \phi$$

with

$$\phi(-L, y) = \phi(L, y)$$

$$\phi_x(L, y) = \phi_x(L, y)$$

$$\phi(x, 0) = 0$$

$$\phi(x, H) = 0$$

on the entire boundary. The eigenvalues are $\lambda_{nm} = (n\pi/L)^2 + (m\pi/H)^2$, and the corresponding eigenfunctions are $\phi_{nm}(x, y) = \sin \frac{n\pi x}{L} \sin \frac{m\pi y}{H}$ and $\cos \frac{n\pi x}{L} \sin \frac{m\pi y}{H}$,

where $n = 0, 1, 2, 3, \dots$ and $m = 1, 2, 3, \dots$. Thus,

$$u(x, y, t) = \sum_i A_i(t) \phi_i(x, y)$$

Here the \sum_i represents a summation over all eigenfunctions. Now

$$\begin{aligned} \frac{1}{c^2} u_{tt} + \frac{1}{D} u_t &= \frac{1}{c^2} \sum_i \frac{d^2 A_i(t)}{dt^2} \phi_i(x, y) + \frac{1}{D} \sum_i \frac{d A_i}{dt} \phi_i(x, y) \\ &= \sum_i \left(\frac{1}{c^2} \frac{d^2 A_i}{dt^2} + \frac{1}{D} \frac{d A_i}{dt} \right) \phi_i(x, y) \end{aligned}$$

Thus,

$$\frac{1}{c^2} \frac{d^2 A_i}{dt^2} + \frac{1}{D} \frac{d A_i}{dt} = \frac{\int \int \left(\frac{1}{c^2} u_{tt} + \frac{1}{D} u_t \right) \phi_i dx dy}{\int \int \phi_i^2 dx dy} \quad (\text{C.1})$$

$$= \frac{\int \int \nabla^2 u \phi_i dx dy}{\int \int \phi_i^2 dx dy} \quad (\text{C.2})$$

Now we use Green's formula to find an expression for the right hand side of the above equation.

$$\int \int (\phi_i \nabla^2 u - u \nabla^2 \phi_i) dx dy = \oint (\phi_i \nabla u - u \nabla \phi_i) \cdot \vec{n} ds$$

where \vec{n} is a unit outward normal to the boundary. Since ϕ_i satisfy homogeneous boundary conditions, and hence some of the boundary terms vanish:

$$\begin{aligned} \int \int (\phi_i \nabla^2 u - u \nabla^2 \phi_i) dx dy &= - \oint u \nabla \phi_i \cdot \vec{n} ds \\ &= \int_{-L}^L u \frac{\partial \phi_i}{\partial y} \Big|_y = 0 dx \\ &= \frac{m\pi}{H} U \sin(\omega t) \int_{-L}^L \cos \frac{2\pi kx}{L} \cos \frac{n\pi x}{L} dx \end{aligned}$$

On the left side, since $\nabla^2 \phi_i + \lambda_i \phi_i = 0$, the above equation becomes

$$\begin{aligned} \int \int \phi_i \nabla^2 u dx dy &= -\lambda_i \int \int u \phi_i dx dy + \frac{m\pi}{H} U \sin(\omega t) \int_{-L}^L \cos \frac{2\pi kx}{L} \cos \frac{n\pi x}{L} dx \\ &= -\lambda_i A_i(t) \int \int \phi_i^2 dx dy + \frac{m\pi}{H} U \sin(\omega t) \int_{-L}^L \cos \frac{2\pi kx}{L} \cos \frac{n\pi x}{L} dx \end{aligned}$$

since $A_i(t)$ is the generalized Fourier coefficient of $u(x, y, t)$:

$$A_i(t) = \frac{\int \int u \phi_i dx dy}{\int \int \phi_i^2 dx dy}$$

Consequently, we derive from Eq. (C.2) that

$$\frac{1}{c^2} \frac{d^2 A_i}{dt^2} + \frac{1}{D} \frac{dA_i}{dt} + \lambda_i A_i = \frac{m\pi}{H} U \sin(\omega t) \frac{\int_{-L}^L \cos \frac{2\pi kx}{L} \cos \frac{n\pi x}{L} dx}{\int \int \phi_i^2 dx dy}$$

or

$$\frac{d^2 A_i}{dt^2} + \frac{c^2}{D} \frac{dA_i}{dt} + c^2 \lambda_i A_i = \frac{m\pi}{H} c^2 U \sin(\omega t) \frac{\int_{-L}^L \cos \frac{2\pi kx}{L} \cos \frac{n\pi x}{L} dx}{\int \int \phi_i^2 dx dy} \quad (\text{C.3})$$

We need $n = 2k$, so that the right side of Eq. (C.3) is not zero (otherwise there is only a trivial solution due to zero initial conditions) and it reduces to

$$\frac{d^2 A_m}{dt^2} + \frac{c^2}{D} \frac{dA_m}{dt} + c^2 \lambda_m A_m = \frac{4m\pi}{H^2} c^2 U \sin(\omega t) \quad (\text{C.4})$$

where $\lambda_m = (2k\pi/L)^2 + (m\pi/H)^2$ and $k \neq 0$. For $k = 0$,

$$\frac{d^2 A_m}{dt^2} + \frac{c^2}{D} \frac{dA_m}{dt} + c^2 \lambda_m A_m = \frac{8m\pi}{H^2} c^2 U \sin(\omega t).$$

We put

$$\frac{d^2 A_m}{dt^2} + \frac{c^2}{D} \frac{dA_m}{dt} + c^2 \lambda_m A_m = \frac{pm\pi}{H^2} c^2 U \sin(\omega t),$$

where

$$p = \begin{cases} 4 & \text{if } k \neq 0; \\ 8 & \text{if } k = 0. \end{cases}$$

This is a harmonic oscillator driven by an externally applied sinusoidal force, where

$2m\pi c^2/H^2 U$ is the driving amplitude and ω is the driving frequency. For $(c/2/D)^2 < (2k\pi/L)^2 + (m\pi/H)^2$

the underdamped oscillator has general solution

$$A_m(t) = e^{-\frac{c^2}{2D}t} (c_1 \cos \mu_m t + c_2 \sin \mu_m t) + A_p$$

where $\mu_m = \sqrt{c^2\lambda_m - (c^2/2/D)^2}$ and A_p is a particular solution, which can be obtained as

$$A_p = M_m \sin wt + N_m \cos wt$$

where

$$M_m = \frac{pm\pi c^2}{H^2} U \frac{c^2\lambda_m - w^2}{(c^2/D - w^2)^2 + (c^2/D)^2 w^2} \quad (\text{C.5})$$

and

$$N_m = -\frac{pm\pi c^2}{H^2} U \frac{c^2/Dw}{(c^2/D - w^2)^2 + (c^2/D)^2 w^2}. \quad (\text{C.6})$$

After applying the initial conditions, we find $c_1 = N_m$ and $c_2 = c^2 N_m / 2D\mu_m - M_m w / \mu_m$. Thus

$$\begin{aligned} A_m(t) &= -e^{-\frac{c^2}{2D}t} \frac{pm\pi c^2 U}{H^2} \frac{c^2/Dw}{(c^2/D - w^2)^2 + (c^2/D)^2 w^2} \cos \mu_m t \\ &- e^{-\frac{c^2}{2D}t} \left[\frac{c^2}{2D\mu_m} \frac{pm\pi c^2 U}{H^2} \frac{c^2/Dw}{(c^2/D - w^2)^2 + (c^2/D)^2 w^2} \right. \\ &+ \left. \frac{w}{\mu_m} \frac{pm\pi c^2 U}{H^2} \frac{c^2\lambda_m - w^2}{(c^2/D - w^2)^2 + (c^2/D)^2 w^2} \right] \sin \mu_m t \\ &+ \frac{pm\pi c^2 U}{H^2} \frac{c^2\lambda_m - w^2}{(c^2/D - w^2)^2 + (c^2/D)^2 w^2} \sin wt \\ &- \frac{pm\pi c^2 U}{H^2} \frac{c^2/Dw}{(c^2/D - w^2)^2 + (c^2/D)^2 w^2} \cos wt \end{aligned}$$

$$u(x, y, t) = \sum_m A_m(t) \cos \frac{2k\pi x}{L} \sin \frac{m\pi y}{H}$$

The following plots are generated by using $c = 2.0 d/t_{col}$ and $D = 250 d^2/t_{col}$.

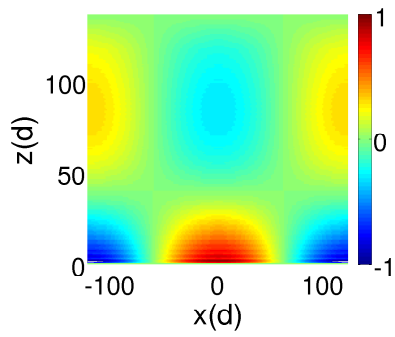
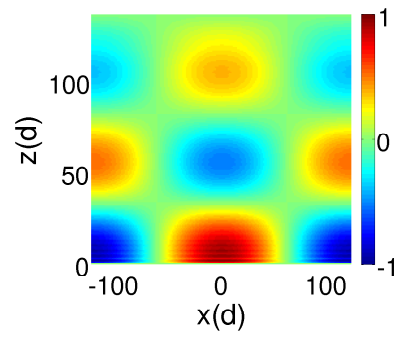
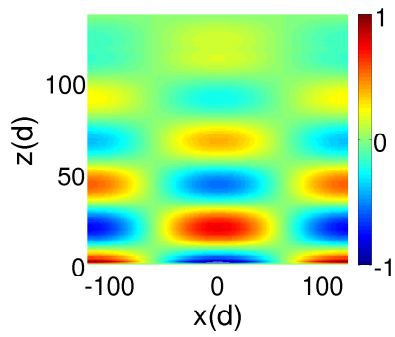
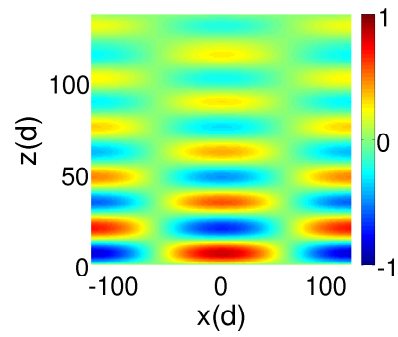
(a) $f = 15$ Hz, $\lambda = 250d$.(b) $f = 30$ Hz, $\lambda = 250d$.(c) $f = 60$ Hz, $\lambda = 250d$.(d) $f = 100$ Hz, $\lambda = 250d$.

Figure C.1 Continuum model results as the frequency of perturbation is modified.

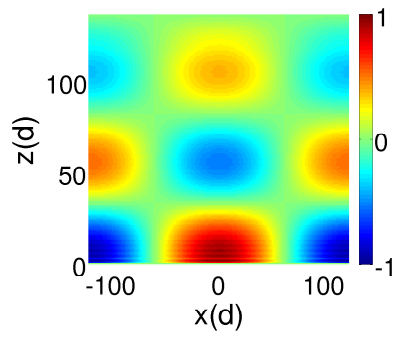
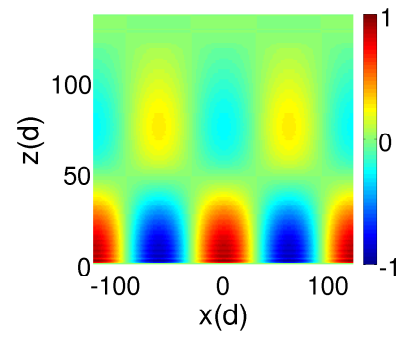
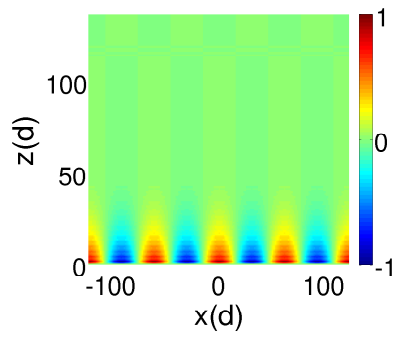
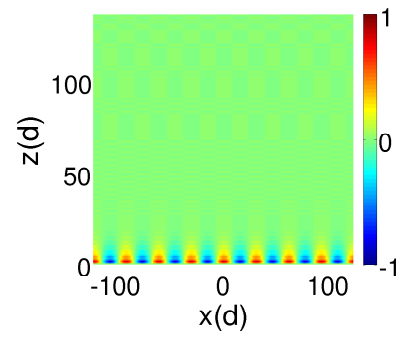
(a) $f = 30$ Hz, $\lambda = 250d$.(b) $f = 30$ Hz, $\lambda = 250d/2$.(c) $f = 30$ Hz, $\lambda = 250d/4$.(d) $f = 30$ Hz, $\lambda = 250d/8$.

Figure C.2 Continuum model results as the wavelength of perturbation is modified.

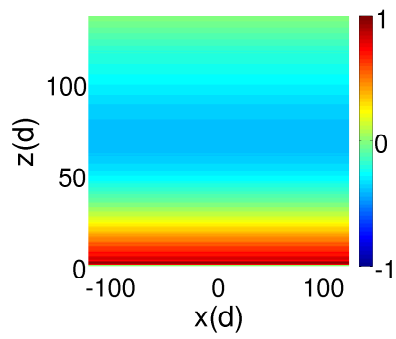
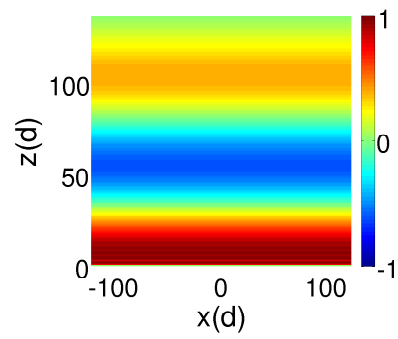
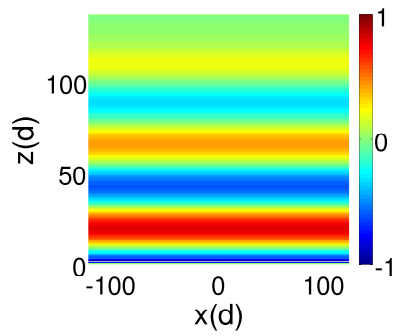
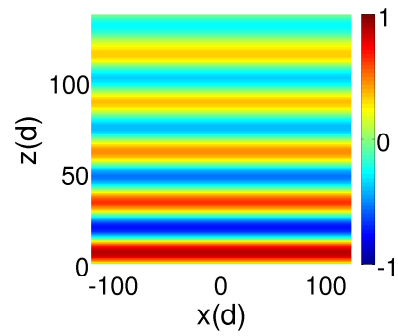
(a) $f = 15$ Hz, $\lambda = \infty$.(b) $f = 30$ Hz, $\lambda = \infty$.(c) $f = 60$ Hz, $\lambda = \infty$.(d) $f = 100$ Hz, $\lambda = \infty$.

Figure C.3 Continuum model results as the frequency of perturbation is modified for spatially independent perturbation.

APPENDIX D

AFFINE AND NON-AFFINE DEFORMATIONS

Deformation of a system may be conforming or non-conforming - in granular systems, where a classical example is plane Couette flow driven by the motion of the boundaries. The dynamics of the particles which conforms to the imposed shear leading to (in this case) a linear velocity profile is called conforming or affine. Any deviation of the affine dynamics is non-affine. In this appendix, we present a general approach which we use to compute both affine (in the case it is not known) and non-affine components of particle motion.

We start by collecting the local information around each particle from its neighbors. For one particle, a circle of radius R centered at this specified particle is defined, and all particles in this circle are considered to be its neighbors. We choose the size of the radius $R = 2.5d$. For example, $\mathbf{r}_0(t)$ denotes the position of this central particle and $\mathbf{r}_m(t), m = 1, \dots, n$, denotes the positions of the neighboring particles, respectively. Thus, the actual displacement of one neighboring particle relative to the central one is

$$\mathbf{r}_n(t) - \mathbf{r}_0(t) \tag{D.1}$$

at time t . We denote the affine deformation as

$$\mathbf{r}(t + \delta t) = A(t) \cdot \mathbf{r}(t)$$

where $A(t)$ can be any 2×2 matrix. Under the affine deformation, the displacement of the neighboring particle relative to the central one becomes

$$A(t) \cdot \mathbf{r}_n(t) - A(t) \cdot \mathbf{r}_0(t). \tag{D.2}$$

Then we define a new quantity \mathcal{D}^2 as the mean-square difference between these two displacements, Eq. (D.1). and Eq. (D.2), i.e.

$$\mathcal{D}^2 = \sum_{n=1}^m \|\mathbf{r}_n(t + \delta t) - \mathbf{r}_0(t + \delta t) - [A(t) \cdot \mathbf{r}_n(t) - A(t) \cdot \mathbf{r}_0(t)]\|^2, \quad (\text{D.3})$$

and define the minimal of \mathcal{D}^2 as the measurement of the localized non-affine deformation.

We minimize \mathcal{D}^2 with respect to the elements of $A(t)$, i.e.

$$A(t) = \begin{bmatrix} A_{11}(t) & A_{12}(t) \\ A_{21}(t) & A_{22}(t) \end{bmatrix}.$$

Rewriting Eq. (D.3) as

$$\mathcal{D}^2 = \sum_{n=1}^m \|\mathbf{r}_n(t + \delta t) - \mathbf{r}_0(t + \delta t) - \begin{bmatrix} A_{11}(t) & A_{12}(t) \\ A_{21}(t) & A_{22}(t) \end{bmatrix} \cdot [\mathbf{r}_n(t) - \mathbf{r}_0(t)]\|^2. \quad (\text{D.4})$$

Let

$$\mathbf{r}_n(t + \delta t) - \mathbf{r}_0(t + \delta t) = \begin{bmatrix} R_n^x(t + \delta t) \\ R_n^y(t + \delta t) \end{bmatrix}$$

and

$$\mathbf{r}_n(t - \delta t) - \mathbf{r}_0(t - \delta t) = \begin{bmatrix} R_n^x(t) \\ R_n^y(t) \end{bmatrix},$$

then Eq. (D.4) implies that

$$\begin{aligned} \mathcal{D}^2 &= \sum_{n=1}^m \left\| \begin{bmatrix} R_n^x(t + \delta t) \\ R_n^y(t + \delta t) \end{bmatrix} - \begin{bmatrix} A_{11}(t) & A_{12}(t) \\ A_{21}(t) & A_{22}(t) \end{bmatrix} \cdot \begin{bmatrix} R_n^x(t) \\ R_n^y(t) \end{bmatrix} \right\|^2 \\ &= \sum_{n=1}^m \left\| \begin{bmatrix} R_n^x(t + \delta t) - A_{11}(t)R_n^x(t) - A_{12}(t)R_n^y(t) \\ R_n^y(t + \delta t) - A_{21}(t)R_n^x(t) - A_{22}(t)R_n^y(t) \end{bmatrix} \right\|^2 \\ &= \sum_{n=1}^m \left[[R_n^x(t + \delta t) - A_{11}(t)R_n^x(t) - A_{12}(t)R_n^y(t)]^2 \right. \\ &\quad \left. + [R_n^y(t + \delta t) - A_{21}(t)R_n^x(t) - A_{22}(t)R_n^y(t)]^2 \right]. \end{aligned}$$

We differentiate \mathcal{D}^2 with respect to the element of $A(t)$, respectively,

$$\begin{aligned}\frac{d\mathcal{D}^2}{dA_{11}} &= -\sum_{n=1}^m 2 [R_n^x(t + \delta t) - A_{11}(t)R_n^x(t) - A_{12}(t)R_n^y(t)] R_n^x(t) = 0, \\ \frac{d\mathcal{D}^2}{dA_{12}} &= -\sum_{n=1}^m 2 [R_n^x(t + \delta t) - A_{11}(t)R_n^x(t) - A_{12}(t)R_n^y(t)] R_n^y(t) = 0, \\ \frac{d\mathcal{D}^2}{dA_{21}} &= -\sum_{n=1}^m 2 [R_n^y(t + \delta t) - A_{21}(t)R_n^x(t) - A_{22}(t)R_n^y(t)] R_n^x(t) = 0, \\ \frac{d\mathcal{D}^2}{dA_{22}} &= -\sum_{n=1}^m 2 [R_n^y(t + \delta t) - A_{21}(t)R_n^x(t) - A_{22}(t)R_n^y(t)] R_n^y(t) = 0.\end{aligned}$$

Then solve for them

$$\begin{aligned}\sum_{n=1}^m R_n^x(t + \delta t)R_n^x(t) - A_{11}(t) \sum_{n=1}^m R_n^x(t)R_n^x(t) - A_{12}(t) \sum_{n=1}^m R_n^x(t)R_n^y(t) &= 0, \\ \sum_{n=1}^m R_n^x(t + \delta t)R_n^y(t) - A_{11}(t) \sum_{n=1}^m R_n^x(t)R_n^y(t) - A_{12}(t) \sum_{n=1}^m R_n^y(t)R_n^y(t) &= 0, \\ \sum_{n=1}^m R_n^y(t + \delta t)R_n^x(t) - A_{21}(t) \sum_{n=1}^m R_n^x(t)R_n^x(t) - A_{22}(t) \sum_{n=1}^m R_n^x(t)R_n^y(t) &= 0, \\ \sum_{n=1}^m R_n^y(t + \delta t)R_n^y(t) - A_{21}(t) \sum_{n=1}^m R_n^x(t)R_n^y(t) - A_{22}(t) \sum_{n=1}^m R_n^y(t)R_n^y(t) &= 0.\end{aligned}$$

So

$$\begin{aligned}A_{11}(t) &= \frac{1}{S} \sum_{n=1}^m R_n^x(t + \delta t)R_n^x(t) \sum_{n=1}^m R_n^y(t)R_n^y(t) \\ &\quad - \frac{1}{S} \sum_{n=1}^m R_n^x(t + \delta t)R_n^y(t) \sum_{n=1}^m R_n^x(t)R_n^y(t), \\ A_{12}(t) &= \frac{1}{S} \sum_{n=1}^m R_n^x(t + \delta t)R_n^y(t) \sum_{n=1}^m R_n^x(t)R_n^x(t) \\ &\quad - \frac{1}{S} \sum_{n=1}^m R_n^x(t + \delta t)R_n^x(t) \sum_{n=1}^m R_n^x(t)R_n^y(t), \\ A_{21}(t) &= \frac{1}{S} \sum_{n=1}^m R_n^y(t + \delta t)R_n^x(t) \sum_{n=1}^m R_n^y(t)R_n^y(t) \\ &\quad - \frac{1}{S} \sum_{n=1}^m R_n^y(t + \delta t)R_n^y(t) \sum_{n=1}^m R_n^x(t)R_n^y(t), \\ A_{22}(t) &= \frac{1}{S} \sum_{n=1}^m R_n^y(t + \delta t)R_n^y(t) \sum_{n=1}^m R_n^x(t)R_n^x(t) \\ &\quad - \frac{1}{S} \sum_{n=1}^m R_n^y(t + \delta t)R_n^x(t) \sum_{n=1}^m R_n^x(t)R_n^y(t),\end{aligned}$$

where

$$S = \sum_{n=1}^m R_n^x(t)R_n^x(t) \sum_{n=1}^m R_n^y(t)R_n^y(t) - \sum_{n=1}^m R_n^x(t)R_n^y(t) \sum_{n=1}^m R_n^x(t)R_n^y(t).$$

Therefore, we find the affine deformation matrix $A(t)$ which minimizes \mathcal{D}^2 , and then obtain the non-affine contribution by evaluating \mathcal{D}^2 at this $A(t)$. We denote it as \mathcal{D}_{min}^2 , and its square root as \mathcal{D}_{min} which is shown in the main text.

APPENDIX E

SIMULATING IMPACTS OF A LARGE INTRUDER

In this section, we simulate a large intruder impacts on granular matter. If the intruder is a disk of the same material as the granular particles, then all the previous calculations follow. However, we would like to vary the shape of the intruder, for instance, an elliptical intruder. In order to achieve that, we generate a composite intruder, which is made up of a number of individual particles assigned on the surface of the composite intruder. Although particles are only on the surface, the intruder is treated as a solid object. In this new scenario, when a particle collides with the intruder at a point, it actually interacts with the particle composed of the intruder at that point. Thus, most of the particle-particle collision we described earlier can follow. Now we list all the modification required.

Equations of motion for the intruder: First, we write down the motion equations of the intruder.

$$m_{b,p} \frac{d^2 \mathbf{r}_{0,p}}{dt_p^2} = m_{b,p} \mathbf{g} + \sum_i \mathbf{F}_{i,p} \quad (\text{E.1})$$

$$I_{b,p} \frac{d^2 \phi_{b,p}}{dt_p^2} = \sum_i (\mathbf{r}_{i,p} - \mathbf{r}_{0,p}) \times \mathbf{F}_{i,p}, \quad (\text{E.2})$$

where $m_{b,p}$ is the mass of the intruder, $I_{b,p}$ is its moment of inertia, $\mathbf{r}_{i,p}$ is the position of particle i on the intruder, $\mathbf{r}_{0,p}$ is the center of mass of the intruder, $\phi_{b,p}$ is the rotational angle of the intruder in the xy-plane, and $\mathbf{F}_{i,p}$ is the total force of particle i on the intruder.

We see that the motion of the intruder is determined by the total forces experienced by all the particles on the intruder.

The reduced mass: When a system particle hits an intruder particle, the particle on the intruder should be treated as the intruder as a whole. So the reduced mass of this collision is not the reduced mass we use for the two particles. Instead, it ought to be the reduced mass of the system particle and the intruder.

Moment of inertia: The moment of inertia of intruders vary as their shape changes. In a two-dimensional system, particles and the intruder are allowed to rotate only in the $x - y$ plane. Thus, the rotation is about the z -axis. In general, the moment of inertia of a continuous solid body rotated about the z axis can be calculated by the integral

$$I = \int_V \rho(\mathbf{r})d(\mathbf{r})^2 dV(\mathbf{r}),$$

where $\rho(\mathbf{r})$ is the mass density at point \mathbf{r} , and $d(\mathbf{r})$ is the distance from point \mathbf{r} to the axis of rotation. The integration goes over the volume V of the body.

- Circle

Particles in the system are treated as disks. The moment of inertia of a thin, solid disk of radius r and mass m , rotating about z axis, is given by

$$I_z = \int_0^h \int_0^{2\pi} \int_0^r \rho(x^2 + y^2) d\theta dr dz = \frac{mr^2}{2}.$$

- Ellipse

The moment of inertia of an ellipse with the same mass, given the major axis a and minor axis b , is obtained in the same way, that is

$$I_z = \int_0^h \int_{-b}^b \int_{-a\sqrt{1-\frac{x^2}{b^2}}}^{a\sqrt{1-\frac{x^2}{b^2}}} (x^2 + y^2) d\theta dr dz = \frac{1}{4}(a^2 + b^2)m.$$

Position and velocity: The position of any intruder particle is determined by the combination of the linear motion which is updated from the previous calculation and

the rotational motion which rotates an angle of ϕ_b about the intruder's center of mass (x_0, y_0) in the xy-plane. The general forms are given by

$$x_i = (x_{i,l} - x_0) \cos \phi_b - (y_{i,l} - y_0) \sin \phi_b + x_0,$$

and

$$y_i = (x_{i,l} - x_0) \sin \phi_b + (y_{i,l} - y_0) \cos \phi_b + y_0.$$

Here $(x_{i,l}, y_{i,l})$ is the translational position of particle i on the intruder, and (x_i, y_i) is the final position of particle i on the intruder after combining contributions from both translational motion and rotational motion.

Intruder particles move and interact as a whole. We can imagine that the angular velocity of an intruder is the same at every point, but the velocity is not the same anywhere. The velocity of an intruder particle is expressed as

$$\mathbf{v}_i = \mathbf{v}_b + \boldsymbol{\omega}_b \times (\mathbf{r}_i - \mathbf{r}_0),$$

where \mathbf{v}_i denotes the velocity of the intruder particle i , \mathbf{v}_b is intruder's linear velocity, $\boldsymbol{\omega}_b = (0, 0, \omega_b)$ and $\omega_b = \frac{d\phi_b}{dt}$ is the angular velocity of the intruder, $\mathbf{r}_i = (x_i, y_i)$ is the position of particle i on the intruder, and \mathbf{r}_0 is intruder's center of mass.

One other thing that needs to be changed is the relative velocity calculation of a collision between a system particle and an intruder particle. We have given the general expression for relative velocity for two particles in Eq. A.1 as follow:

$$\mathbf{v}_{i,j} = (\mathbf{v}_i - \mathbf{v}_j) - (\omega_i d_i / 2 + \omega_j d_j / 2) \mathbf{e}_z \times \mathbf{n}_i.$$

We point out that d_i and d_j are the diameters of the two particles, and the normal \mathbf{n}_i is always along the line through the centers of the two particles. However, when a system particle and an intruder particle come into contact, the normal between the two particles is not the true normal of the system particle and the intruder as a

whole, thus we replace the relatively velocity in this case approximately by

$$\mathbf{v}_{b,j} = (\mathbf{v}_b - \mathbf{v}_j) - (\omega_b |\mathbf{r}_i - \mathbf{r}_0| + \omega_j d_j / 2) \mathbf{e}_z \times \mathbf{n}_i.$$

Spring constant: Now we deal with the k_{bg} , the spring constant for a particle-intruder collision. Spring constants vary from material to material. For two-material collisions, we assume there are two springs; one is for the system particle and the other one is for the intruder. According to Hooke's law, when two springs are attached in series, the equivalent spring constant is given by

$$k_{bg} = \frac{k_g k_b}{k_g + k_b},$$

where k_g is the spring constant for the system particles and k_b is the spring constant for the intruder.

REFERENCES

- [1] M. A. Ambroso, R. D. Kamien, and D. J. Durian. Dynamics of shallow impact cratering. *Phys. Rev. E*, 72:041305, 2005.
- [2] M. A. Ambroso, C. R. Santore, A. R. Abate, and D. J. Durian. Penetration depth for shallow impact cratering. *Phys. Rev. E*, 71:051305, 2005.
- [3] M. Ammi, D. Bideau, and J. P. Troadec. Geometrical structure of disordered packings of regular polygons; comparison with disc packing structures. *J. Phys. D: Appl. Phys.*, 20:424, 1987.
- [4] G. P. Berman and F. M. Izrailev. The Fermi-Pasta-Ulam problem: fifty years of progress. *Chaos*, 15:015104, 2005.
- [5] W. A. Beverloo, H. A. Leniger, and J. Van De Velde. *Chemical Engineering Science*, 15:260, 1961.
- [6] J.-P. Bouchaud, M. E. Cates, and P. Claudin. Stress distribution in granular media and nonlinear wave equation. *J. Phys. I*, 5:639, 1995.
- [7] J.-P. Bouchaud, P. Claudin, M. E. Cates, and J. P. Wittmer. Models of stress propagation in granular media. In H. J. Herrmann, J.-P. Hovi, and S. Luding, editors, *Physics of Dry Granular Media*, page 97, Dordrecht, 1998. Kluwer Academic Publishers.
- [8] J.-P. Bouchaud, P. Claudin, D. Levine, and M. Otto. Force chain splitting in granular materials: A mechanism for large-scale pseudo-elastic behavior. *Eur. Phys. J. E*, 4:451, 2001.
- [9] F. Bourrier, F. Nicot, and F. Darve. Physical processes within a 2D granular layer during an impact. *Granul. Matter*, 10:415, 2008.
- [10] C. S. Campbell and A. Gong. The stress tensor in a two-dimensional granular shear flow. *J. Fluid Mech.*, 164:107, 1986.
- [11] S. Chapman and T. G. Cowling. *The mathematical theory of nonuniform gases*. Cambridge University Press, London, 1960.
- [12] M. P. Ciamarra, A. H. Lara, A. T. Lee, D. I. Goldman, I. Vishik, and H. L. Swinney. Dynamics of drag and force distributions for projectile impact in a granular medium. *Phys. Rev. Lett.*, 92:194301, 2004.
- [13] S. N. Coppersmith, C.-h. Liu, S. Majumdar, O. Narayan, and T. A. Witten. Model for force fluctuations in bead packs. *Phys. Rev. E*, 53:4673, 1996.

- [14] C. Coste, E. Falcon, and S. Fauve. Solitary waves in a chain of beads under Hertz contact. *Phys. Rev. E*, 56:6104, 1997.
- [15] C. Coste and B. Gilles. On the validity of Hertz contact law for granular material acoustics. *Eur. Phys. J. B*, 7:155, 1999.
- [16] C. Daraio, V. F. Nesterenko, E. B. Herbold, and S. Jin. Strongly nonlinear waves in a chain of teflon beads. *Phys. Rev. E*, 72:16603, 2005.
- [17] C. Daraio, V. F. Nesterenko, E. B. Herbold, and S. Jin. Energy trapping and shock disintegration in a composite granular medium. *Phys. Rev. Lett.*, 96:058002, 2006.
- [18] J. R. de Bruyn and A. M. Walsh. Penetration of spheres into loose granular media. *Can. J. Phys.*, 82:439, 2004.
- [19] R. Doney and S. Sen. Decorated, tapered, and highly nonlinear granular chain. *Phys. Rev. Lett.*, 97:155502, 2006.
- [20] J. Duffy and R. D. Mindlin. Stress-strain relations and vibrations of a granular medium. *J. Appl. Mech.*, 24:585, 1957.
- [21] J. Duran, editor. *Sands, Powders, and Grains*. Springer-Verlag, New York, 2000.
- [22] M. Falk and J. Langer. *Phys. Rev. E*, 57:7192, 1998.
- [23] F. C. Franklin and L. N. Johanson. Flow of granular materials through a circular orifice. *Chemical Engineering Science*, 4:119, 1955.
- [24] J. Geng, R. P. Behringer, G. Reydellet, and E. Clément. Green's function measurements of force transmission in 2d granular materials. *Physica D*, 182:274, 2003.
- [25] J. Geng, D. Howell, E. Longhi, R. P. Behringer, G. Reydellet, L. Vanel, E. Clément, and S. Luding. Footprints in sand: The response of a granular material to local perturbations. *Phys. Rev. Lett.*, 87:035506, 2001.
- [26] B. Gilles and C. Coste. Low-frequency behavior of beads constrained on a lattice. *Phys. Rev. Lett.*, 90:174302, 2003.
- [27] J. D. Goddard. Nonlinear elasticity and pressure-dependent wave speeds in granular media. *Proc. R. Soc. Lond. A*, 430:105, 1990.
- [28] C. Goldenberg and I. Goldhirsch. Force chains, microelasticity, and macroelasticity. *Phys. Rev. Lett.*, 89:084302, 2003.
- [29] C. Goldenberg and I. Goldhirsch. Friction enhances elasticity in granular solids. *Nature*, 435:188, 2005.

- [30] C. Goldenberg and I. Goldhirsch. Effects of friction and disorder on the quasistatic response of granular solids to a localized force. *Phys. Rev. E*, 77:041303, 2008.
- [31] D. I. Goldman and P. Umbanhowar. *Phys. Rev. E*, 77:021308, 2008.
- [32] J. Hong. Universal power-law decay of the impulse energy in granular protectors. *Phys. Rev. Lett.*, 94:108001, 2005.
- [33] J. Hong and A. Xu. Effects of gravity and nonlinearity on the waves in the granular chain. *Phys. Rev. E*, 63:061310, 2001.
- [34] S. R. Hostler. *Wave propagation in granular materials*. PhD thesis, California Institute of Technology, 2005.
- [35] S. R. Hostler and C. E. Brennen. Pressure wave propagation in a granular bed. *Phys. Rev. E*, 72:031303, 2005.
- [36] S. R. Hostler and C. E. Brennen. Pressure wave propagation in a shaken granular bed. *Phys. Rev. E*, 72:031304, 2005.
- [37] R. Jackson. Some mathematical and physical aspects of continuum models for the motion of the granular materials. In R. E. Meyer, editor, *Theory of Dispersed Multiphase Flow*, page 291. Academic Press, New York., 1983.
- [38] H. M. Jaeger, S. R. Nagel, and R. P. Behringer. Granular solids, liquids, and gases. *Reviews of Modern Physics*, 68:1259, 1996.
- [39] X. Jia. Codalike multiple scattering of elastic waves in dense granular media. *Phys. Rev. Lett.*, 93:154303, 2004.
- [40] X. Jia, C. Caroli, and B. Velicky. Ultrasound propagation in externally stressed granular media. *Phys. Rev. Lett.*, 82:1863, 1999.
- [41] S. Kann, S. Joubaud, G. A. C-Robledo, D. Lohse, and D. van der Meer. *Phys. Rev. E*, 81:041306, 2010.
- [42] H. Katsuragi and D. J. Durian. Unified force law for granular impact cratering. *Nature Physics*, 3:420, 2007.
- [43] L. Kondic. Dynamics of spherical particles on a surface: Collision-induced sliding and other effects. *Phys. Rev. E*, 60:751, 1999.
- [44] L. Kondic, O. Dybenko, and R. P. Behringer. Probing dense granular materials by space-time dependent perturbations. *Phys. Rev. E*, 79:041304, 2009.
- [45] A. N. Lazaridi and V. F. Nesterenko. Observation of a new type of solitary waves in a one-dimensional granular medium. *Journal Appl. Mech. Tech. Phys.*, 26:405, 1985.
- [46] C.-h. Liu. Spatial patterns of sound propagation in sand. *Phys. Rev. B*, 50:782, 1994.

- [47] C.-h. Liu and S. R. Nagel. Sound in sand. *Phys. Rev. Lett.*, 68:2301, 1992.
- [48] C.-h. Liu and S. R. Nagel. Sound in a granular material: Disorder and nonlinearity. *Phys. Rev. B*, 48:15646, 1993.
- [49] S. Luding. Information propagation. *Nature*, 435:159, 2005.
- [50] H. A. Makse, N. Gland, D. J. Johnson, and L. M. Schwartz. Why effective medium theory fails in granular materials. *Phys. Rev. Lett.*, 83:5070, 1999.
- [51] H. A. Makse, N. Gland, D. J. Johnson, and L. M. Schwartz. Granular packings: Nonlinear elasticity, sound propagation, and collective relaxation dynamics. *Phys. Rev. E*, 70:061302, 2004.
- [52] K. Mischaikow. Computational Homology Project, <http://chomp.rutgers.edu/>.
- [53] C. F. Moukarzel, H. Pacheco-Martinez, J. C. Ruiz-Suarez, and A. M. Vidales. Static response in disk packings. *Granular Matter*, 6:61, 2004.
- [54] N. W. Mueggenburg, H. M. Jaeger, and S. R. Nagel. Stress transmission through three dimensional ordered granular arrays. *Phys. Rev. E*, 66:031304, 2002.
- [55] R. M. Nedderman. *Statics and kinematics of granular materials*. Cambridge University Press, Cambridge, 1992.
- [56] E. L. Nelson, H. Katsuragi, P. Mayor, and D. J. Durian. Projectile interactions in granular impact cratering. *Phys. Rev. Lett.*, 101:068001, 2008.
- [57] V. Nesterenko. *Dynamics of Heterogenous Media*. Springer, New York, 2001.
- [58] V. F. Nesterenko. Solitary waves in discrete media with anomalous compressibility and similar to “sonic vacuum”. *Journal de Physique IV*, 4:729, 1994.
- [59] V. F. Nesterenko, C. Daraiao, E. B. Herbold, and S. Jin. Anomalous wave reflection at the interface of two strongly nonlinear granular media. *Phys. Rev. Lett.*, 90:158702, 2005.
- [60] V.F. Nesterenko. Propagation of nonlinear compression pulses in granular media. *J. Appl. Mech. Tech. Phys.*, 24:733, 1983.
- [61] K. A. Newhall and D. J. Durian. Projectile-shape dependence of impact craters in loose granular media. *Phys. Rev. E*, 68:060301, 2003.
- [62] M. Nishida, K. Tanaka, and Y. Matsumoto. Discrete Element Method Simulation of the Restitutive Characteristics of a Steel Spherical Projectile from a Particulate Aggregation. *JSME International Journal Series A*, 47:438, 2004.
- [63] S. Ostoja and D. Panja. Elasticity from the force network ensemble in granular media. *Phys. Rev. Lett.*, 97:208001, 2006.

- [64] M. Otto, J.-P. Bouchaud, P. Claudin, and J. E. S. Socolar. Anisotropy in granular media: Classical elasticity and directed-force chain network. *Phys. Rev. E*, 67:0313023, 2003.
- [65] J.V. Poncelet. *Course de Me'canique Industrielle*. Paris, 1829.
- [66] F. Radjai, M. Jean, J. J. Moreau, and S. Roux. Force distribution in dense two-dimensional granular systems. *Phys. Rev. Lett.*, 77:274, 1996.
- [67] G. Reydellet and E. Clément. Green's function probe of a static granular piling. *Phys. Rev. Lett.*, 86:3308, 2001.
- [68] H. F. Rose and T. Tanaka. Rate of discharge of granular materials from bins and hoppers. *The Engineer*, 208:465, 1959.
- [69] S. B. Savage. Analysis of slow high-concentration flows of granular materials. *J. Fluid Mech.*, 377:1, 1998.
- [70] A. Scott. *Nonlinear Science*. Oxford University Press, London, 2003.
- [71] A. Seguin, Y. Bertho, and P. Gondret. Influence of confinement on granular penetration by impact. *Phys. Rev. E*, 78:010301, 2008.
- [72] A. Seguin, Y. Bertho, P. Gondret, and J. Crassous. Sphere penetration by impact in a granular medium: A collisional process. *Europhys. Lett.*, 88:44002, 2009.
- [73] S. Sen, M. Manciu, R. S. Sinkovits, and A. J. Hurd. Nonlinear acoustics in granular assemblies. *Granular Matter*, 3:33, 2001.
- [74] S. Sen, M. Manciu, and J. D. Wright. Solitonlike pulses in perturbed and driven Hertzian chains and their possible applications in detecting buried impurities. *Phys. Rev. E*, 57:2386, 1998.
- [75] P. Sheng. *Introduction to Wave Scattering, Localization, and Mesoscopic Phenomena*. Academic Press, San Diego, 1995.
- [76] M. Da Silva and J. Rajchenbach. Stress transmission through a model system of cohesionless elastic grains. *Nature*, 406:708, 2000.
- [77] R. S. Sinkovits and S. Sen. Nonlinear dynamics in granular columns. *Phys. Rev. Lett.*, 74:2686, 1995.
- [78] E. Somfai, J.-N. Roux, J. H. Snoeijer, M. van Hecke, and W. van Saarloos. Elastic wave propagation in confined granular systems. *Phys. Rev. E*, 72:021301, 2005.
- [79] M. B. Stone, D. P. Bernstein, R. Barry, M. D. Pelc, Y. Tsui, and P. Schiffer. Getting to the bottom of a granular medium. *Nature*, 427:503, 2004.
- [80] J. Tang and R. P. Behringer. IFRPI-NSF Collaboratory: 2D hopper data summary. Technical report, Duke University, 2010.

- [81] A. V. Tkachenko and T. A. Witten. Stress propagation through frictionless granular material. *Phys. Rev. E*, 60:687, 1999.
- [82] M. Toda. Problems in nonlinear dynamics. *J. Math.*, 8:197, 1978.
- [83] L. S. Tsimring and D. Volfson. Modeling of impact cratering in granular media. In R. Garcia-Rojo, H. J. Herrmann, and S. McNamara, editors, *Powders and Grains*, page 1215, Leiden, 2005.
- [84] J. S. Uehara, M. A. Ambroso, R. P. Ojha, and D. J. Durian. Low-speed impact craters in loose granular media. *Phys. Rev. Lett.*, 90:194301, 2003.
- [85] P. Umbanhowar and D. I. Goldman. Granular impact and the critical packing state. *Phys. Rev. E*, 82:010301, 2010.
- [86] B. Velicky and C. Caroli. Pressure dependence of the sound velocity in a two-dimensional lattice of Hertz-Mindlin balls: Mean-field description. *Phys. Rev. E*, 65:021307, 2002.